Cloud effects on erythemal UV radiation in a complex topography

Daniel Walker

Cloud effects on erythemal UV radiation in a complex topography

Daniel Walker

Diss. ETH No. 18415

Cloud effects on erythemal UV radiation in a complex topography

A dissertation submitted to the
Swiss Federal Institute of Technology (ETH)
Zurich

for the degree of
Doctor of Sciences

presented by
Daniel Walker
Dipl. Natw. ETH
born 10 August 1976
citizen of Winterthur (ZH)

accepted on the recommendation of
Prof. Dr. U. Lohmann, examiner
Prof. Dr. S. Brönnimann, co-examiner
Dr. L. Vuilleumier, co-examiner
Prof. Dr. M. Blumthaler, co-examiner

2009

Abstract

UV radiation is part of the solar spectrum with wavelengths between 100 and 400 nm. In this study, erythemal UV is investigated; a measure directly related to the harmfulness of solar radiation to our skin. UV radiation has important impacts on different ecosystems, life and also on public health. Therefore, detailed information about the spatial distribution of UV radiation and its temporal evolution is required. Since observations are spatially and temporally sparse, these issues are often approached by radiative transfer modeling. These models perform well for simulating UV radiation for clear-sky conditions, but it is far more difficult for them to capture the short-term variability due to a rapidly changing cloud cover.

The main research topic of the presented thesis concerns cloud effects on UV radiation at four stations in the complex Swiss topography. These stations contribute to the new SACRaM (Swiss Alpine Climate Radiation Monitoring) network and are situated in regions with different climate conditions. The effect of clouds on UV is inferred using observed total solar radiation (SW), which is commonly measured in operational networks. The use of SW radiation and the assessment of the impacts of local environmental conditions on the method enable its application at many locations and for long time periods. The relationship between atmospheric UV and SW transmission was derived using cloud modification factors (CMFs), parameterized separately for strong and weak cloud attenuation using two linear regressions. The analysis of the dependencies of the shape of this parameterization demonstrated that the solar zenith angle (SZA) is the environmental factor with the strongest impact. Furthermore, the derived relationship was physically interpreted incorporating radiative transfer theory and modeling exercises. The results of these studies and the theoretical principles are confirmed by our observations and semi-empiric relationship: the transmission through clouds is generally larger for UV than for SW radiation. However, differences in cloud effects for strong overcast cloud cover and scattered clouds with weaker attenuation were found. For overcast conditions, a change in cloud optical depth provoked stronger variation in the CMF_{UV} than in CMF_{SW}. The same changes for scattered conditions lead to larger changes in SW radiation. These effects are more pronounced for large solar zenith angles. A comparison with the results of a pure modeling based approach provided further indications about the general applicability of the derived method and the possibility to use the parameterization also at other locations without further adaptation.

Clear-sky radiative transfer is important for investigating the effects of clouds since it allows determining their impacts on the atmospheric transmission in a cloudy atmosphere. The validation of the radiative transfer model estimating clear-sky radiation revealed a

good agreement with observed UV between 2.9–5.5 mW m^{-2} (5–7%) and the correspondence for SW was even higher with RMS of 15.2–20.8 W m^{-2} (3–4%). Linear regression models of modeled vs. observed clear-sky radiation yielded slopes close to one, i.e. 1.00–1.01 for UV and 0.98–1.02 for SW radiation.

In addition, modeling atmospheric irradiance requires information about the average surface reflectivity around the point of interest. The surface reflectance is mainly determined by the presence of snow, especially for UV radiation. Therefore, the spatial distribution and temporal evolution of the regional snow cover in Switzerland was investigated in more details. Snow depth observations at 125 stations in combination with a digital elevation model were used for deriving spatial snow cover information within five different regions in Switzerland back to 1980. The resulting daily snow distributions were cross-validated against snow observations over 28 years and compared to satellite snow-masks within 4 case studies. Probability of detections of 0.96 and false alarm rates of 0.15 were found in the cross-validation, while the agreement with the satellite reached values between 69 and 97%. Reconstructed time-series of regional snow cover were tested for temporal trends. In the lowlands north of the Alps, a significant decrease between -10 and -15% was found over the last 28 years. The temporal evolutions in the other, more elevated alpine regions were also negative, but smaller and statistically not significant.

Since the derived relationship between CMF$_{UV}$ and CMF$_{SW}$ mainly depends on SZA and not on the location, it can be used for estimating all-sky UV radiation for time periods when and also at other locations where the necessary input data (ozone, albedo, and observed SW radiation) is available. The validation of estimated against measured UV radiation at the four SACRaM stations showed a very good agreement with RMS errors between 4.3 and 6.9 mW m^{-2} (9–12%) for high temporal resolution of 10 minutes. Aggregated daily doses corresponded even better to observations (RMS < 8%). This generalized relationship was used for reconstructing erythemal UV radiation at the four stations back to 1981 for trend analysis. The strongest increase of UV radiation was found during the months of the first half-year with maximal decadal trends of 8.6–11.5% in March, depending on the station. Over the whole 27-years period, the UV-Index increased for May and June between 0.54 and 0.85. The trends for the months of the second half year are small and mostly not statistically significant.

Zusammenfassung

UV-Strahlung ist Teil des Sonnenspektrums mit Wellenlängen zwischen 100 bis 400 nm. In unserer Studie untersuchen wir die erythemale UV-Strahlung, welche ein direktes Mass für deren Schädlichkeit für unsere Haut darstellt. UV-Strahlung hat weitreichende Auswirkungen auf verschiedene Ökosysteme, Lebewesen und auf unsere Gesundheit. Wir möchten daher mehr über die räumlichen und zeitlichen Charakteristiken der UV-Strahlung erfahren. Da jedoch die beobachteten Zeitreihen spärlich sind, wird diesen Fragen häufig mit Strahlungstransfer Modellen (RTM) begegnet. Solche Modelle zeigen sehr gute Resultate für wolkenfreie Situationen. Die Simulation von kurzzeitigen Wolkeneffekten ist jedoch um ein Vielfaches schwieriger.

Der Hauptteil der vorgelegten Dissertation beschäftigt sich mit Wolkeneffekten auf die erythemale UV-Strahlung an vier Stationen in der komplexen Topography der Schweiz. Diese Stationen sind Teil des neuen SACRaM (Swiss Alpine Climate Radiation Monitoring) Messnetzes und befinden sich in Regionen mit sehr unterschiedlichen Klimabedingungen. Wolkeneffekte auf UV-Strahlung werden mittels beobachteter Sonnenstrahlung (SW) hergeleitet; einer Grösse, welche häufig von operationellen Wetterstationen gemessen wird. Die Verwendung von SW-Strahlung und das Abschätzen der lokalen Umwelteinflüsse auf die Methode erlauben deren Anwendung an vielen Stationen und über lange Zeiträume. Die Beziehung zwischen der atmosphärischen Transmission von UV und SW-Strahlung wurde mittels "cloud modification factors" (CMFs) hergeleitet und mit zwei separaten linearen Regressionen für starke und leichte Bewölkung beschrieben. Die Analyse der Abhängigkeiten dieser Beziehung von verschiedenen Umweltfaktoren zeigte, dass der Sonnenstand den grössten Einfluss auf deren Form ausübt. Die Charakteristiken der Beziehung wurden unter Miteinbezug von Strahlungstransfer-Theorie und früheren Modellstudien auf ihre physikalische Bedeutung hin interpretiert. Diese theoretischen und modellbasierten Grundlagen sind in Übereinstimmung mit unseren Beobachtungen: Die Transmission von Wolken ist generell grösser im UV Bereich als für SW-Strahlung. Es wurden jedoch Unterschiede zwischen geschlossener Wolkenbedeckung und aufgelockerter Bewölkung mit geringerer Strahlungsabschwächung gefunden. Für die geschlossene Wolkendecke führt eine Veränderung in der optischen Dicke der Wolken zu grösseren Änderungen für $\mathrm{CMF_{UV}}$ als für $\mathrm{CMF_{SW}}$. Die gleiche Veränderung der optischen Dicke bei aufgelockerter Bewölkung führt hingegen zu grösseren Änderungen im SW Bereich. Diese Effekte verstärken sich im Allgemeinen für tiefe Sonnenstände. Die Resultate eines direkten Vergleichs der Beziehung mit einem rein modellbasierten Ansatz ergaben weitere Hinweise auf die Möglichkeit, die hergeleitete Methode ohne weitere Anpassungen auch an anderen Orten einzusetzen.

Für die Bestimmung von Wolkeneffekten ist der Strahlungstransfer für wolkenfreie Situationen wichtig, da dieser Aussagen über den Einfluss von Wolken auf die Transmissivität einer bewölkten Atmosphäre erlaubt. Die Validation des RTM zeigte im UV Bereich mittlere Abweichungen (RMS) zu Messungen von 2.9–5.5 mW m^{-2} (5–7%) und für SW 15.2–20.8 W m^{-2} (3–4%). Lineare Regressionsmodelle zwischen dem Modell und den Beobachtungsdaten ergaben Steigungen zwischen 1.00–1.01 (UV) und 0.98–1.02 (SW). Die Modellierung atmosphärischer Strahlung benötigt Informationen zur Bodenreflektivität. Die Schneebedeckung ist die wichtigste Grösse zur Bestimmung der Albedo, dies gilt im Speziellen für die UV-Strahlung. Aus diesem Grund wurde die räumliche Schneeverteilung und deren zeitliche Entwicklung in der Schweiz untersucht. Schneemessungen an 125 Stationen wurden mit einem digitalen Geländemodell kombiniert um die räumliche Schneebedeckung in fünf Regionen der Schweiz zurück bis 1980 zu ermitteln. Die modellierten Scheeverteilungen wurden über 28 Jahre mit Schneebeobachtungen validiert und in vier Fallstudien mit Satellitendaten verglichen. Die Validierung zeigte Nachweiswahrscheinlichkeiten (POD) von 0.96 und Fehlalarmraten (FAR) von 0.15, während der Satellitenvergleich mittlere Übereinstimmungen zwischen 69–97% ergab. Die rekonstruierte Schneebedeckung wurde auf zeitliche Veränderungen untersucht. Für das Schweizer Mittelland resultierte eine signifikante Abnahme der Schneebedeckung zwischen -10 und -15% seit 1980. Die Trends in den höher gelegenen, alpinen Regionen sind kleiner und statistisch nicht signifikant.

Da die hergeleitete Beziehung zwischen CMFs im UV und SW Bereich hauptsächlich vom Sonnenstand und nicht vom Standort abhängt, kann diese ebenfalls für die Modellierung von UV-Strahlung für Zeitperioden und an anderen Orten verwendet werden, wo Informationen über Totalozon, Albedo und SW vorhanden sind. Die Validierung dieses UV-Modells mit Beobachtungen an den vier SACRaM-Stationen führte zu sehr guten Übereinstimmungen mit RMS Fehlern zwischen 4.3 und 6.9 mW m^{-2} (9–12%) für eine hohe zeitliche Auflösung von 10 Minuten. Aggregierte Tagesdosen zeigten noch kleinere Abweichungen zu Beobachtungen (< 8%). UV-Strahlung wurde an den vier Stationen zurück bis 1981 rekonstruiert und auf ihre zeitliche Entwicklung analysiert. Der grösste Anstieg der UV-Strahlung wurde für Monate des ersten Halbjahrs verzeichnet, mit maximalen Zuwachsraten im März zwischen 8.6–11.5% pro Dekade. Über die gesamte analysierte Periode, ergab sich ein Anstieg des UV-Index für Mai und Juni zwischen 0.54 und 0.86. Die Trends für die Monate der zweiten Jahreshälfte waren zumeist klein und statistisch nicht signifikant.

Contents

Chapter 1

Introduction

> The sun, with all those planets revolving around it and
> dependent upon it, can still ripen a bunch of grapes as if
> it had nothing else in the universe to do. *Galileo Galilei*

In the history of mankind, the sun has often been symbolic for life. But not all impacts of sunlight are godsends and positive; the sunlight also bears risks for our planet. In this chapter solar ultraviolet radiation is introduced and various implications on the Earth and our daily life are discussed. Furthermore, today's problems and still open questions illustrate the motivation for the presented study, followed by a brief outline of the research, which was performed during my PhD studies.

1.1 Ultraviolet radiation

The solar radiation reaching the top of the Earths atmosphere is similar to the energy distribution of a perfect emitter with a temperature of ∼5800 K, also called a black body (Figure 1.1). For most applications in environmental science a wavelength range between 100 Å and 3 m is considered. The total energy output of the Sun is relatively stable and amounts to approximately 1366 W m^{-2}, a constant also referred to as TSI (Total Solar Irradiance). However, some variations, especially for short wavelengths, are caused by the rotation cycle of the Sun, which takes around 27 days, and an approximately 11-year cycle in the solar magnetic activity. This variability can be linked to the number of sunspots and leads to changes in the TSI of the order of 0.05–0.07% (Foukal et al., 2006).

The wavelength range between 100 and 400 nm is defined as ultraviolet radiation (UV), which is separated into vacuum-UV, UVC, UVB, and UVA (Figure 1.2). For most applications in environmental photobiology UVB and UVA radiation is of importance, while shorter wavelengths below 280 nm are already absorbed fairly high in the earth's atmosphere. The contribution of UV radiation to the TSI is relatively small and amounts to roughly 8% at the top of atmosphere. Nevertheless, this part of the solar spectrum plays an important role for the photochemistry in the stratosphere and troposphere. Enhanced UVB radiation is furthermore considered harmful for aquatic ecosystems and may decrease the phytoplankton productivity, which not only plays an important role in
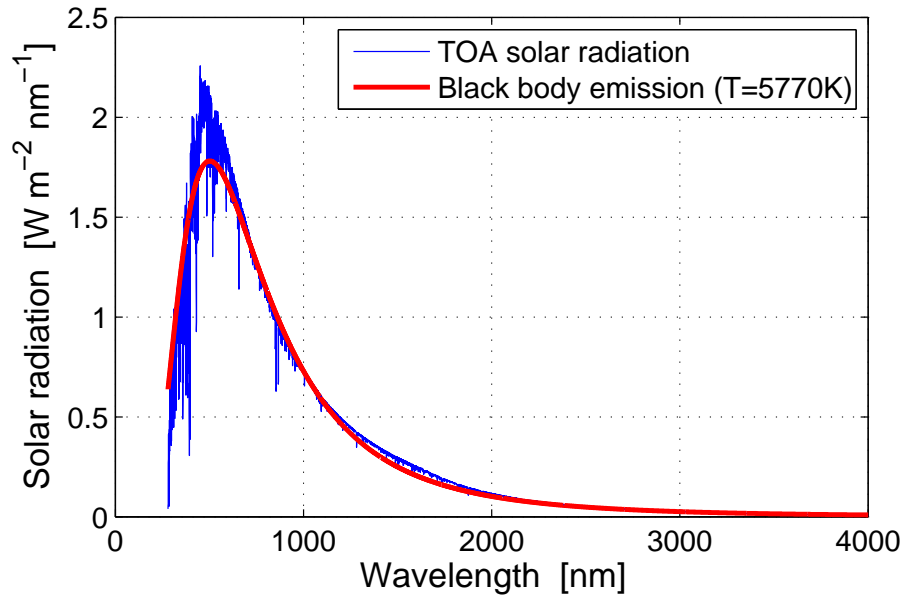
FIG. 1.1: Solar spectrum at the top of atmosphere (TOA) for wavelengths smaller than 4000 nm. The data is smoothed using a moving average over 0.7 nm. For comparison, the emission of a black body with a temperature of 5770 K is shown (red).
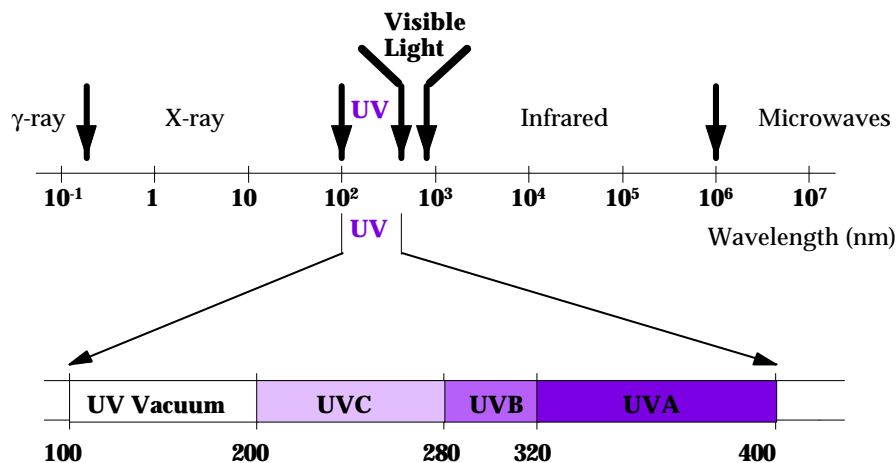
FIG. 1.2: The ultraviolet components of the electromagnetic spectrum (source: Soehnge et al., 1997)

the food web but also represents a valuable sink for atmospheric carbon dioxide (Häder, 1997). There are also terrestrial plants that are sensitive to UV radiation reacting with modified growth, leaf area and photosynthetic activity on changing UVB levels (Tevini, 1993).

A wide range of impacts of UV radiation on the health of human beings has been documented. UV can damage the eyes and reduce the immune system's functionality. For this reason, exposure to UV and sunlight can increase the susceptibility of the individual to illnesses such as herpes (Perna et al., 1987) or the HIV-1 virus (Valerie et al.,

1988). However, the activation of the vitamin D_3 production, which is important for our skeletal health, represents a positive effect of UV exposure. The most prominent effects of UV on our body and skin are tanning and sunburn. There are serious skin diseases including different forms of skin cancer for which UV radiation is considered a major etiological factor (Diffey, 2004). Two major forms of skin cancer must be distinguished: the non-melanocytic carcinomas (basal cell carcinoma and squamous cell carcinoma) and the melanoma skin cancer. The non-melanoma forms show a high incidence rate in the population but are usually well treatable and the mortality is relatively low on the order of 1-2% (Calbó et al., 2005). These skin cancers are closely related to UV and sunlight and also develop on sun-exposed parts of the human body. However, this relation is less well understood for the much more dangerous malignant melanoma, but there is now growing evidence that intermittent sun exposure is associated with increased risk of developing malignant melanoma (Diffey, 2004).

Due to this sensitivity of our skin to sunlight, which greatly varies with wavelength, a radiation measure has been sought for describing the harmfulness of UV radiation. Hence, a standard erythemal action spectrum was defined, assigning more weight to wavelengths to which our skin is more sensitive (McKinlay and Diffey, 1987). In Figure 1.3, the UV radiation reaching the Earth's surface (black) is shown with the standard erythemal action spectra (red). The integral of the erythemally weighted solar spectrum (blue) is called erythemal UV radiation and is used to derive the UV-index, which is a tool for communicating the risks represented by UV radiation to the public.
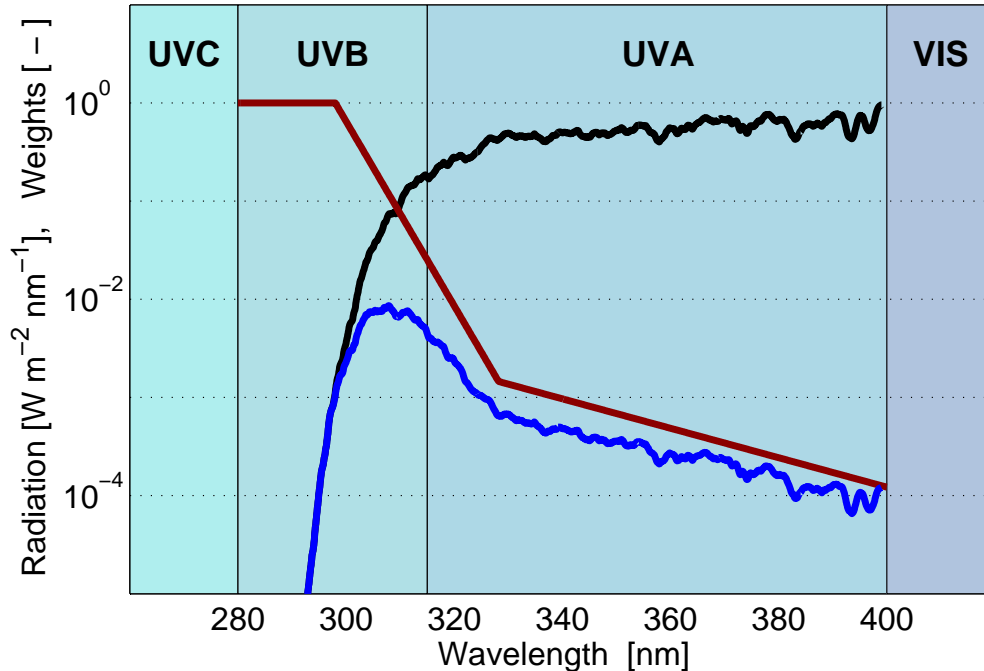

FIG. 1.3: The atmospheric irradiance (black) at the surface and the standard erythemal action spectrum (red). The erythemally weighted solar radiation is shown in blue. Note: the y-axis is in logarithmic scale and is used for both the solar radiation and the dimensionless weights of the erythemal action spectrum.

The air molecules and aerosols in the stratosphere and troposphere interact with the incoming solar radiation before it reaches the Earths surface. Both, absorption and scattering processes lead to a loss of solar radiation. While absorption processes include a transformation of the incoming energy, scattering on aerosols and molecules redirects the radiation, building the diffuse sky radiation and reflecting a part of it back into space. The incoming solar radiation is scattered at the molecules of atmospheric gases following the principles of Rayleigh scattering, which is much more efficient for shorter wavelengths. Furthermore, molecules can absorb radiation within certain parts of the solar spectrum. Tropospheric and stratospheric ozone, for instance, strongly absorb UV radiation between 200–300 nm (Hartley region) and more weakly in the Huggins bands, ranging from 300–360 nm (Madronich, 1993). Further UV absorbing gases are nitrogen- and sulfur-dioxide (NO_2, SO_2). The most important aerosols that absorb radiation in the UV are desert dust, biomass burning aerosols, and volcanic aerosols (de Graaf et al., 2007). Aerosols are much larger than molecules and hence the scattering follows the Mie-theory, whose dependence on radiation wavelength is weaker than for Rayleigh scattering. Scattering sulphate aerosols for example are frequently observed in industrialized regions as a haze, reducing the visibility in the planetary boundary layer (Madronich, 1993). In non-urban areas of industrialized countries the UVB radiation is estimated having significantly decreased due to increased SO_2-emissions as compared to pre-industrial levels (Liu et al., 1991). However, the majority of the European countries have reduced their emissions by more than 60% between 1990 and 2004. Furthermore, the total sulphur target for 2010 set in the Gothenburg Protocol has already been met in 2004 at a European level (Vestreng et al., 2007).

The stratospheric ozone content has a direct effect on the atmospheric transmission of UVB radiation due to the previously discussed absorption processes. Therefore, the significant depletion of stratospheric ozone in springtime over the Antarctic region since the late 1970s (Farman et al., 1985; Stolarski et al., 1986) raised serious concern about a future rise of UV levels in a changed ozone climate (Blumthaler and Ambach, 1990). Crutzen and Arnold (1986) proposed the corresponding chemical mechanisms for the formation of the ozone hole. Based on their model, they stated that the observed depletion was mainly due to emissions of industrial organic chlorine compounds (cf. Molina and Rowland, 1974). Especially Polar Stratospheric Clouds during Antarctic spring provide a suitable surface for heterogeneous chemical reactions, which play a crucial role for the depletion of stratospheric ozone (Solomon et al., 1986). As a reaction to this drastic decline of the stratospheric ozone layer, the Montreal Protocol was initiated in 1987 and eventually signed by more than 190 nations. The aim of this protocol was banning the manufacture of ozone-destroying chemicals primarily chlorofluorocarbons. In recent years, the scientific community intensified its research for detecting a recovery of the ozone layer (e.g. Newchurch et al., 2003; Steinbrecht et al., 2004, 2006). Actually, a significant leveling-off of the declining total ozone within the springtime Antarctic vortex since 1997 was found by Yang et al. (2008). The temporal evolution of the ozone layer is also in Switzerland continuously assessed by remote sensing and regular balloon soundings. Due to the strong ties between UV and ozone, and uncertainties about future changes in the ozone climate, several projects were initiated in the last decade (e.g. COST 713, CUVRA, and EDUCE) investigating UV under various atmospheric conditions and establishing UV-forecasts for public information.

1.2 Motivation and objectives

The scientific community is interested to advance the understanding of the spatial distribution and temporal evolution of UV radiation due to the many implications on various ecosystems and our daily life. While a lot of attention is paid to changes of the stratospheric ozone, the climatological changes of various other environmental factors also influence the amount of incoming UV radiation, such as the atmospheric turbidity, clouds or modified seasonal cycles in snow coverage.

The lengths of observed UV time-series with sufficient data quality do not allow statistical trend analysis in many European countries. Furthermore, the spatial density of UV observing meteorological stations is sparse, which also hampers conclusions regarding the regional distribution of UV radiation. Information about the spatial characteristics of UV is especially valuable for countries with a complex topography like Switzerland, where climate conditions change over short distances. A possible approach to respond to this data scarcity is the application of models for simulating UV for time periods and locations where no observations are available. Radiative transfer models proved in various previous studies being able to estimate UV radiation for clear-sky conditions. However, as soon as clouds interfere with cloud free conditions, atmospheric radiation modeling becomes more difficult. The radiative effects caused by a complex scattered cloud coverage can not be adequately simulated by common 1-dimensional models. Furthermore, 3-dimensional modeling, necessary for addressing such complex situations requires very large data sets for characterizing the cloud fields, which are only exceptionally available. Therefore, it is one of today's important needs to be able to cope with such rapidly changing cloud effects on UV radiation in a simple way and reaching at the same time a high degree of generalization. This allows assessing the cloud effects on UV radiation at many locations and extending existing observed time-series into the past.

The main objective of the presented thesis is the investigation of cloud effects on erythemal UV radiation in a complex topography. This analysis is performed at four stations in Switzerland, which are situated in regions with different climate conditions ranging from the Swiss lowlands to high-alpine environments. The cloud effects in the UV are described by the short-term variability of observed total solar radiation (SW). The use of such an approach enables conclusions at a large number of stations, since this parameter is measured by the extensive operational Swiss meteorological network over almost three decades. A second important aim of this thesis is the assessment of the appropriateness of the chosen approach in this complex alpine topography with different climate conditions. In this study, a new parameterization technique is proposed for describing the relationship between cloud effects in the UV and SW radiation. The investigation of the dependencies of the derived relationship on environmental factors represents a third goal. This information is especially important for drawing conclusions about the general applicability of the method including its uncertainties also at locations where UV is not measured but the required SW radiation is available. This allows estimating UV radiation at a much higher spatial resolution and its reconstruction back to the early 1980s.

These issues are addressed in different parts of the presented study. The main research of this thesis deals with cloud effects on UV and SW radiation and is presented in Chapter 4. These cloud effects are investigated by means of cloud modification factors (CMFs). The shape of the relationship between CMF_{UV} and CMF_{SW} is interpreted with respect to differences in the radiative transfer for UV and SW radiation. Furthermore, the dependencies of the parameterization on environmental factors such as total ozone, surface reflectivity and solar zenith angle are assessed. For testing the appropriateness of the chosen method, estimated all-sky UV radiation is validated against observations at four stations. Since these stations are situated in regions of Switzerland with very different local climate conditions, this validation also allows drawing conclusions about the level of generalization of the used method. In addition, the uncertainties can be estimated when all-sky UV radiation is calculated with this method at other locations in Switzerland, where the necessary input data (ozone, albedo, and SW radiation) is available.

The results of this analysis are used in Chapter 5 for reconstructing erythemal UV radiation back to early 1980s. The derived time-series at the four stations are investigated for temporal trends using non-parametric Mann-Kendall tests and Sen's slope estimations. The same trend assessment is also applied on the proxy data: total ozone, SW radiation and the surface reflectance.

The calculation of cloud modification factors requires information about the UV and SW radiation for the same situations but without clouds. These clear-sky estimates are simulated with libRadtran, a radiative transfer model (RTM). In Chapter 2 the setup of this RTM is described and its performance in modeling clear-sky UV and SW radiation is assessed by comparisons with observations. The results of this modeling exercise also revealed a strong dependency of the agreement between modeled and observed UV radiation on the solar zenith angle. This behavior indicated a non-ideal Lambertian response of the used biometers. Therefore, a post-processing algorithm based on actual calibration information was developed for correcting this instrumental deficiency.

The surface reflectivity represents an important input parameter to the RTM. This reflectivity is mostly determined by the presence or absence of snow on the ground. Therefore, the spatial distribution of snow is studied in details in Chapter 3. A method is developed for estimating the regional snow distribution based on daily snow depth measurements in combination with a digital elevation model. The resulting regional snow cover data is validated using cross-validation and by comparisons with satellite snow masks. The time-series of estimated snow cover are also tested for significant temporal trends in five different regions of Switzerland.

Chapter 2

Data

In the present study, observed atmospheric radiation data of different meteorological networks are analyzed. These networks are introduced and a brief overview about their aims and history is given. Beside observational data, the estimated clear-sky radiation in the SW and UV range is required for assessing cloud effects (Section 2.2). More information about the total ozone content, snow measurements, and effective albedo estimates, which mainly serve as input to the radiation modeling can be found in the Data sections of Chapter 3 and 4, where they are introduced in context of applications in two different studies. The erythemal UV data, playing a crucial role in these studies underwent additional correction procedures, which are discussed in detail at the end of this chapter.

2.1   Atmospheric radiation networks in Switzerland

Historically, meteorological stations of different networks have been measuring atmospheric radiation parameters in Switzerland. These networks have different aims and can be separated into an extensive operational meteorological network for standard applications and smaller networks equipped with high-quality instrumentation used for research purposes, including climate monitoring. These research-networks provide radiation measurements of superior quality and higher temporal resolution, but at much fewer locations compared to the operational automatic network. In this study, both the radiation observations of MeteoSwiss' operational network and additional data with superior research quality are used. The different networks are presented below and further information about their evolution and future developments are given.

2.1.a   ANETZ/SMN

MeteoSwiss has been operating an automatic network (ANETZ), measuring a large number of meteorological parameters with a time resolution of 10 minutes for almost three decades. The most important parameters related to atmospheric radiation are the downwelling total solar radiation (SW), the sunshine duration and the luminosity. A detailed description about these radiation measurements within ANETZ is given by Moesch and Zelenka (2004). The first ANETZ stations became active in the late 1970s and today, the network consists of a total of 72 stations. The locations, where these stations are situated, characterize the different climate conditions found in Switzerland's lowland and

alpine regions. MeteoSwiss is currently renewing its automatic network and is going to unite several previous networks under one general meteorological network, called Swiss-MetNet (SMN, Heimo et al., 2006). After completing this transition to SMN in 2012, spatially and temporally highly resolved meteorological measurements will be performed at 132 stations in Switzerland.

2.1.b CHARM

MeteoSwiss initiated the Swiss Atmospheric Radiation Monitoring Program (CHARM) in the early 1990s. The aim of CHARM is the observation of longwave and shortwave irradiance, including the separation of the latter into its direct and diffuse component; in addition the aerosol optical depth is determined. Furthermore, broadband ultraviolet radiation (UV) is measured for investigating UV in different regions of Switzerland and on a wide range in altitude. This also allows assessing associated effects such as atmospheric ozone, aerosol optical depths, albedo and long term trends (cf. Philipona et al., 1996). The CHARM network consists of four radiometric automatic stations located on the Swiss plateau and in the Alps: Payerne, Jungfraujoch, Davos, and Locarno-Monti. All of these stations are measuring atmospheric short- and longwave radiation, erythemal UV, and spectral radiation at specific wavelengths with Precision Filter Radiometers (PFRs). In this study, erythemal UV irradiance data at these four CHARM stations is analyzed, where this parameter was measured since the mid to end of the 1990s.
Outstanding CHARM-stations are Payerne and the Jungfraujoch: Payerne is the only station in Switzerland, which is member of the Baseline Surface Radiation Network (BSRN) of the World Climate Research Program within the World Meteorological Organization (WMO). The high-alpine station at Jungfraujoch contributes to the Global Atmosphere Watch (GAW) program of the WMO with the status of a global station, and is a well known site for atmospheric research in the free atmosphere.

2.1.c ASRB

A second atmospheric radiation research network was established in the mid 1990s called Alpine Surface Radiation Budget (ASRB). The aim of ASRB is the investigation of the surface radiation budget at different altitudes and its relation to the greenhouse effect (Marty, 2000; Marty et al., 2002; Philipona et al., 1996). This network currently incorporates 10 stations in Switzerland, which are distributed between 370 and 3580 m MSL. For the calculation of the radiation budgets at the surface, downwelling short- and longwave radiation and additionally at some locations the reflected upward radiation components are measured.

2.1.d SACRaM

MeteoSwiss is currently planning to unite the previously described CHARM and ASRB under one radiation-research network, called Swiss Alpine Climate Radiation Monitoring (SACRaM). SACRaM will measure short- and longwave radiation, spectral radiation in the UV and near-IR, and broadband UV radiation at six locations in the Swiss lowlands and Alpine regions (Table 2.1). This new network will include the four CHARM stations extended with two elevated ASRB stations at Cimetta and Weissfluhjoch (Figure 2.1).
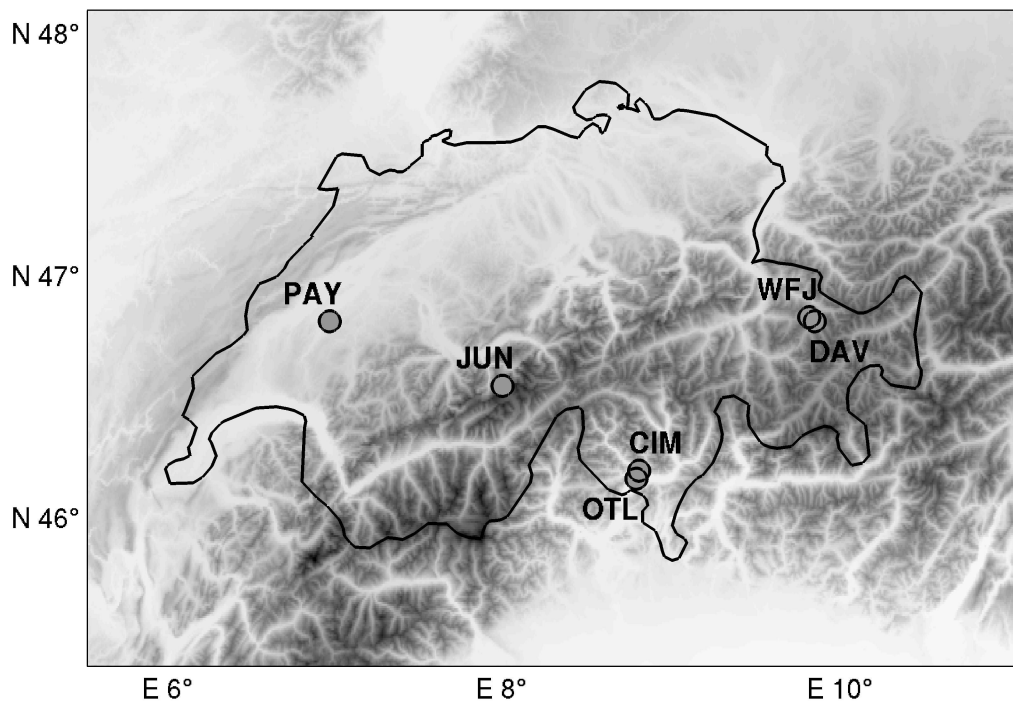
FIG. 2.1: Location map of the stations constituting the new MeteoSwiss SACRaM network for atmospheric radiation research. PAY: Payerne, JUN: Jungfraujoch, WFJ: Weissfluhjoch, DAV: Davos, CIM: Cimetta, and OTL: Locarno-Monti

2.2 Clear-sky radiation

For assessing cloud effects on SW and UV, information about the possible radiation for clear-sky conditions is required. These estimates are obtained from simulations with a radiative transfer model (RTM), which is described in more details below.

2.2.a Radiative transfer modeling

The modeling of clear-sky UV and SW radiation is performed with libRadtran (version 1.01), a software package for radiative transfer calculations (www.libradtran.org). The core of this package is *uvspec*, a program for calculating radiances, irradiances and actinic fluxes over a large wavelength range covering UV, visible, and thermal radiation. Mayer and Kylling (2005) give more information on libRadtran, the available radiative transfer equation solvers and the variety of input parameters. The performance of this RTM was previously assessed by Mayer et al. (1997) who found very good agreements between modeled and observed UV radiation for clear-sky situations. However, the choice of this specific model is not crucial for the precision of modeled clear-sky radiation. Koepke et al. (1998, 2006) found in a comparison of several radiative transfer models that all gave good results from a mathematical point of view. The main uncertainties in modeled irradiances

TABLE 2.1: Overview of stations constituting the new SACRaM network at MeteoSwiss. The list of parameters only refers to a subset of measured variables at each station, which deal with atmospheric radiation. Abbreviation (ID) and net identifier (Net) C: previous CHARM-station, A: previous ASRB-station.

Station	ID	Net	Coordinates °N / °E / alt (m)	Parameters					
Payerne	PAY	C	46.81°/6.94°/491m	SW:	glo	dir	dif	ref	
				LW:	dwn				upw
				UVE:	**glo**	**dir**	**dif**	**ref**	
				UVA:	glo				
				PFR:		dir			
Jungfrau-joch	JUN	C	46.55°/7.99°/3582m	SW:	glo	dir			
				LW:	dwn				
				UVE:	**glo**	**dir**			
				UVA:	glo				
				PFR:		dir			
Davos	DAV	C	46.82°/9.85°/1590m	SW:	glo	dir	dif		
				LW:	glo				
				UVE:	**glo**	**dir**	**dif**		
				PFR:		dir			
Locarno-Monti	OTL	C	46.18°/8.78°/366m	SW:	glo	dir	dif		
				LW:	dwn				
				UVE:	**glo**	**dir**	**dif**		
				UVA:	glo				
				PFR:		dir			
Cimetta	CIM	A	46.20°/8.80°/1670m	SW:	glo			ref	
				LW:	dwn				upw
Weiss-fluhjoch	WFJ	A	46.83°/9.82°/2690m	SW:	glo			ref	
				LW:	dwn				

SW: shortwave radiation
LW: longwave radiation
UVE: erythemally weighted ultraviolet radiation
UVA: ultraviolet radiation (320–400 nm)
PFR: spectral measurements at 16 wavelengths

glo: irradiance (global)
dir: direct component
dif: diffuse component
ref: reflected (surface)
dwn: downward (for LW)
upw: upward (for LW)

for cloud free conditions stem from the uncertainty of the used input parameters describing the atmosphere.

In our study, the clear-sky estimates are used as normalization factors for observed irradiances to assess the cloud attenuation. This estimation of the cloud effects should be available at many locations and for long time-periods when atmospheric data with additional informational content (e.g. turbidity parameters, trace gases, atmospheric profiles) are usually not available. Therefore, we intentionally keep the amount of input data to the model low and aim at a high level of generalization of our approach. The variable input parameters to the model are total ozone, surface albedo, and astronomical parameters. The effective albedo is derived from estimated regional snow distribution, explained in more detail in Section 4.3.a. The total ozone contents are taken from Brewer spectrophotometer measurements at Arosa including a climatological altitude dependent correction to account for the vertical column of tropospheric ozone between Arosa and the different SACRaM stations (cf. Section 4.2.c). More information about the model setup is given in Section 4.3.b.

2.2.b Clear-sky validation

The RTM performance was assessed for clear-sky conditions at the four SACRaM stations Payerne, Davos, Jungfraujoch, and Locarno-Monti. The validation period covers 2.5–5 years, depending on the station. The criterium for identifying clear-sky conditions includes the total cloud coverage and the variability of observed diffuse radiation and is described in more details in Section 4.3.b. Furthermore, only data for solar zenith angles smaller than 72° are considered.

The comparisons between modeled and observed clear-sky radiation in the UV and SW range are presented in Figure 2.2 and 2.3. The model performs well at all four stations and root mean square differences (RMS) between 2.9-5.5 mW m^{-2} (4.9–7.2%) for UV and 15.2–20.8 W m^{-2} (3.1–4.2%) in the SW range are found. Tables 2.2 and 2.3 give more details on the accuracy of the model for the different stations and solar zenith angles (SZAs). The correspondence (relative RMS) between modeled and observed radiation is generally better for small SZAs. In the UV range, the RMS increases from 4–5% for small SZAs to 5–8% for large SZAs. The relative RMS errors are smaller in the SW than in the UV range. Modeled SW radiation deviates less than 3% from observations for small SZAs (22–40°), while the differences increase to 3–5% for large SZAs between 60 and 72°. This validation shows very satisfying results at all four stations and confirms that clear-sky radiation is successfully estimated by the RTM for all seasons and zenith angles.

Apart from this model configuration, which is used in the subsequent studies presented in this thesis, we validated the model including observed aerosol optical depth at Payerne, Davos, and the Jungfraujoch. When introducing derived Ångström parameters into the RTM, the RMS errors decreased by up to 0.5 mW m^{-2}, compared to the validation shown above. At the Jungfraujoch, the bias was reduced from -2.3 to +0.8 mW m^{-2}. The relative RMS errors for this configuration at the three stations with aerosol observations ranged from 4.1 to 4.8%, compared to 4.9–6.2% when no observed aerosol characterization was considered.

FIG. 2.2: Comparison of modeled vs. observed erythemal UV radiation for clear-sky conditions at the four SACRaM stations measuring UV radiation (cf. Table 2.1).

2.3   Calibration of erythemal UV data

2.3.a   *UV calibration at MeteoSwiss*

The measurement of erythemal UV with broadband radiometer (biometers) in an operational network is challenging and demands a rigorous chain of quality controls. Compared to other instruments measuring atmospheric radiation, biometers need special attention because they are known to change their sensitivity and characteristics over short time periods. The sources of this uncertainty are instabilities of the filters approximating the
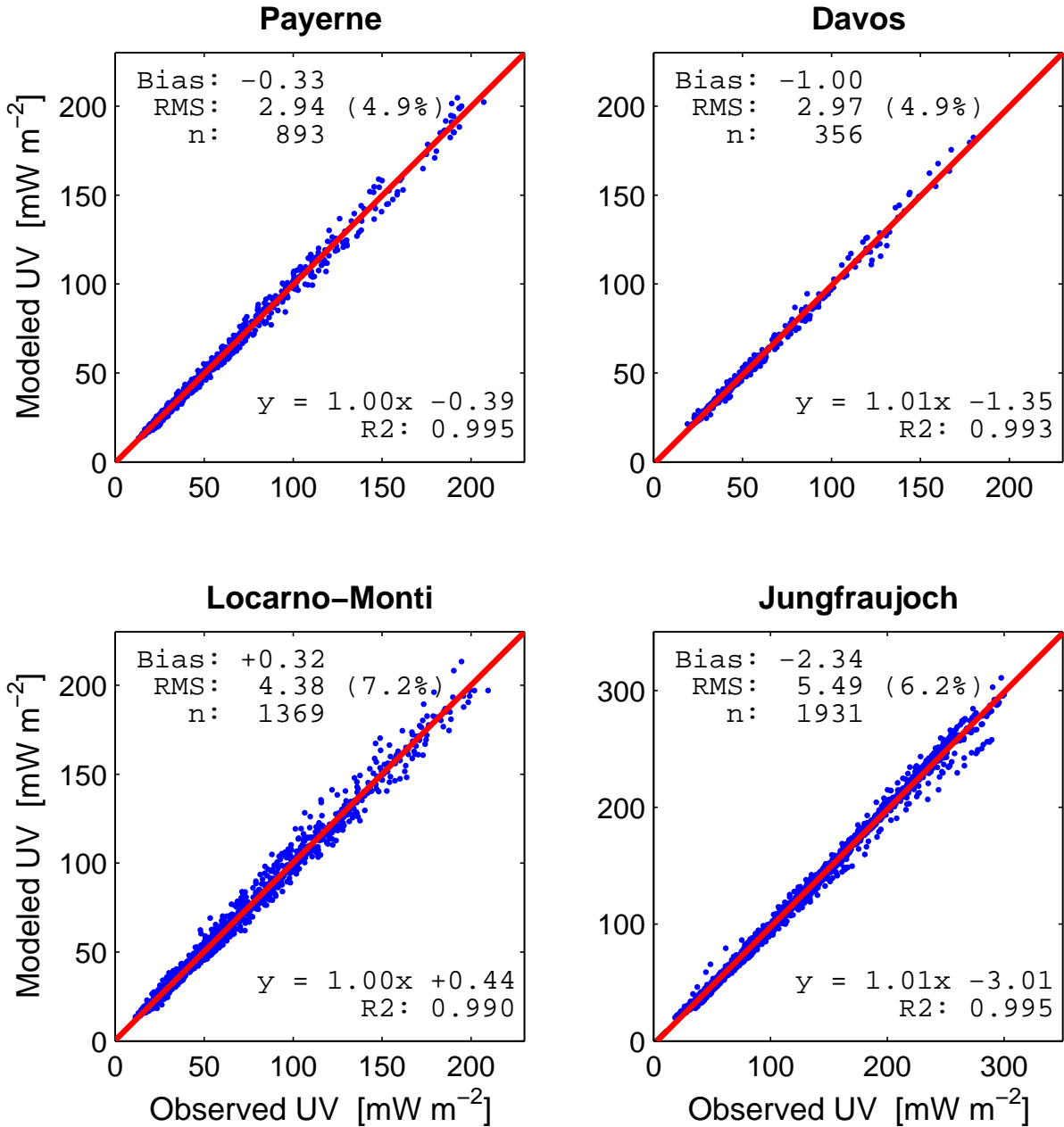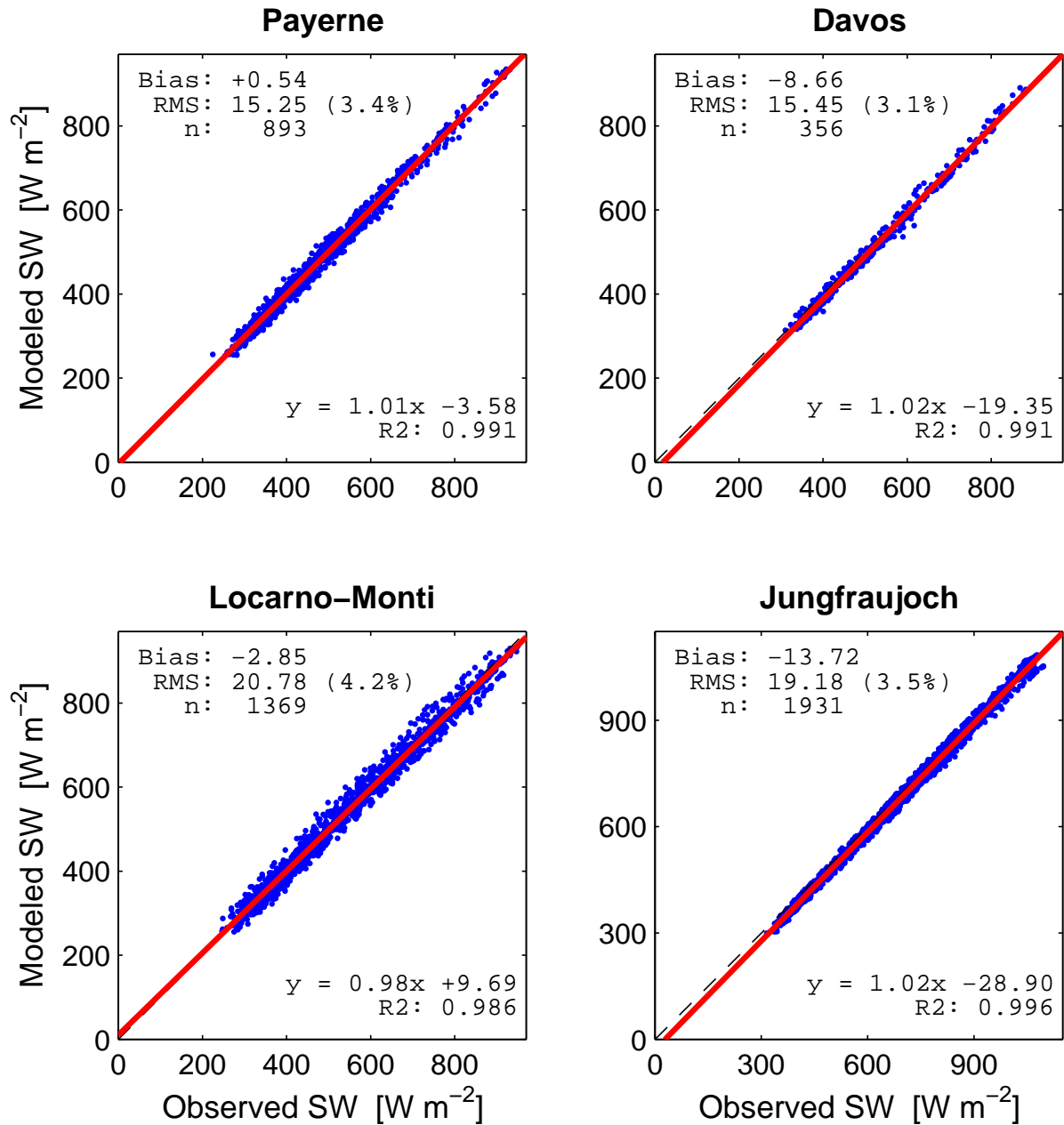
FIG. 2.3: Comparison of modeled vs. observed shortwave (SW) radiation for clear-sky conditions at the four SACRaM stations measuring UV radiation (cf. Table 2.1).

erythemal action spectrum (McKinlay and Diffey, 1987) and the phosphor-based converters influenced by light and humidity.

Regular (re-)calibration and continuous observation of the stability of these instruments are therefore necessary and play a key role for obtaining a sufficiently high data quality, which allows addressing today's needs in UV research. The application of the most sophisticated QA/QC procedures, which are described below, leads to an uncertainty of erythemal UV measurements by biometers on the order of 8-10%. The largest portion of this total uncertainty is caused by the uncertainty of the reference spectroradiometer,

TABLE 2.2: Validation of modeled vs. observed UV radiation at Payerne, Davos, Jungfrau-joch, and Locarno-Monti. The data is separated into three solar zenith angle (SZA) classes ranging from 23 to 72°. Performance measures: Root mean square differences (RMS) in mW m^{-2} and the linear regression coefficients of the model vs. observation: slope (a), intercept (b), and R^2. n refers to the amount of data per station and SZA class. At Davos and for low SZAs ($< 40°$) there are not enough data available for statistical analysis.

	n	RMS	a	b	R^2
Payerne					
SZA: 23-40°	58	6.4 (4.2%)	1.03	-5.5	0.940
SZA: 40-60°	345	3.5 (4.3%)	0.99	+0.9	0.978
SZA: 60-72°	490	1.6 (5.3%)	1.00	-0.4	0.970
Davos					
SZA: 23-40°	9	-	-	-	-
SZA: 40-60°	125	3.8 (4.1%)	1.00	-0.7	0.981
SZA: 60-72°	222	2.2 (5.3%)	0.95	+0.9	0.974
Jungfraujoch					
SZA: 23-40°	328	8.9 (3.6%)	0.93	+14.4	0.900
SZA: 40-60°	835	5.0 (4.4%)	1.01	-3.50	0.985
SZA: 60-72°	768	3.9 (8.3%)	0.95	-0.70	0.972
Locarno-Monti					
SZA: 23-40°	153	7.4 (5.0%)	0.96	+6.5	0.903
SZA: 40-60°	568	5.1 (6.9%)	0.97	+2.9	0.959
SZA: 60-72°	648	2.1 (7.8%)	0.95	+1.4	0.943

used for calibrating the biometers of about 5% (Gröbner et al., 2006). Since the manufacturers of biometers only provide a simple calibration factor per instrument for converting the measured electronic signals (V) into common radiation units (W m^{-2}), the operator should characterize the spectral and cosine dependence of the instrument in order to reach the accuracy mentioned above. The instruments provide broadband measurements over a wavelength range between 280 and 400 nm. In this wavelength interval, the radiation levels at the ground not only change over five orders of magnitudes (cf. Figure 1.3), but also the spectral distribution of this incoming radiation changes with varying total ozone and the path length of the radiation beam in the atmosphere. Therefore, the spectral deviations of the instruments filter from the standard (CIE) erythemal action spectrum (McKinlay and Diffey, 1987) can not be characterized by one single calibration constant. This requires a calibration function depending on the total ozone and the solar zenith angle (SZA). Furthermore, due to diffusor deficiencies, the instrument's angular response does not perfectly follow the expected Lambertian response. A Lambertian behavior means that the detector response depends on the solar zenith angle uniquely from geo-

TABLE 2.3: Validation of modeled vs. observed SW radiation at Payerne, Davos, Jungfrau-joch, and Locarno-Monti. The data is separated into three solar zenith angle (SZA) classes ranging from 23 to 72°. Performance measures: Root mean square differences (RMS) in W m^{-2} and the linear regression coefficients of the model vs. observation: slope (a), intercept (b), and R^2. n refers to the amount of data per station and SZA class. At Davos and for low SZAs ($< 40°$) there are not enough data available for statistical analysis.

	n	RMS	a	b	R^2
Payerne					
SZA: 23-40°	58	14.5 (1.7%)	0.99	+14.8	0.943
SZA: 40-60°	345	16.7 (2.9%)	0.98	+12.4	0.959
SZA: 60-72°	490	14.3 (3.8%)	0.99	+3.1	0.944
Davos					
SZA: 23-40°	9	-	-	-	-
SZA: 40-60°	125	16.4 (2.6%)	1.02	-17.4	0.971
SZA: 60-72°	222	14.9 (3.4%)	0.98	-3.40	0.973
Jungfraujoch					
SZA: 23-40°	328	15.9 (1.6%)	0.98	+12.8	0.932
SZA: 40-60°	835	19.0 (2.6%)	1.02	-29.5	0.976
SZA: 60-72°	768	20.6 (4.7%)	1.02	-25.4	0.983
Locarno-Monti					
SZA: 23-40°	153	24.3 (2.9%)	0.83	137.0	0.780
SZA: 40-60°	568	22.8 (3.7%)	0.93	44.1	0.931
SZA: 60-72°	648	17.8 (4.8%)	0.95	17.8	0.914

metrical factors, i.e., following the cosine law.

In the framework of the COST action 726, guidelines for the operation of UV broadband radiometers were devised (cf. Webb et al., 2007). This guide explains how the different functions, describing the calibration and other corrections, should be applied to convert the measured electric signal into erythemally weighted irradiance:

$$E_{\mathrm{CIE}} = (U - U_{\mathrm{offset}}) \cdot C \cdot f_n\,(\mathrm{SZA}, \mathrm{TO_3}) \cdot \epsilon\,(T) \cdot \mathrm{Coscor} \qquad (2.1)$$

where:

- E_{CIE} is the erythemal effective irradiance.

- U is the measured electrical signal from the radiometer.

- U_{offset} is the electrical offset for dark conditions.

- C is the calibration coefficient, a constant value determined for specific conditions i.e. SZA of 40° and total ozone column of 300 DU.

- $f_n(\mathrm{SZA}, \mathrm{TO_3})$ is a function of solar zenith angle (SZA) and total column ozone ($\mathrm{TO_3}$) i.e. the function can be expressed as a calibration matrix (or look up table) and is derived as part of the calibration procedure. It is normalized at a SZA of 40° and total ozone column of 300 DU. For solar zenith angles less than 40° $f_n(\mathrm{SZA}, \mathrm{TO_3})$ is often nearly unity.

- $\epsilon(T)$ is the temperature correction function (it is recommended that the instrument is temperature stabilized. If this fails then a correction should be applied, which is complex and not always successful).

- Coscor is the cosine correction function (if necessary, otherwise = 1)

The application of this calibration function allows accounting for the most important effects on measured UV due to instrumentation deficiencies. However, UV radiation measurements at MeteoSwiss, starting in the mid to end of the 1990s, did not follow this full correction algorithm (Equation (2.1)) over the whole time period leading to different data quality levels over time. The erythemal UV radiation data used in this study can be separated into three different quality levels: A, B, and C. In the beginning, only a single constant, which is comparable to the factor C in Equation (2.1) was used for characterizing the biometers (Level C). In 2004/05, the calibration procedure at MeteoSwiss was extended (Level B), also considering the deviations of the instruments spectral filter from the CIE erythemal action spectrum. The full calibration formula (2.1) was implemented in 2007/08 for processing raw UV radiation measurements at MeteoSwiss (Level A). An overview about the evolution of the data quality at the four SACRaM stations is given in Figure 2.4.

The consequences of these different quality levels are investigated by comparing original-calibrated UV measurements with estimations of a radiative transfer model (RTM) for clear-sky periods. During time periods with Level-B and -C data, strong seasonal cycles of the ratio of modeled to observed UV radiation were found at all stations. This seasonal signal is caused by non-ideal angular responses of the biometers, which are not considered for calibration during these time periods. In Figure 2.5, time series of the model-to-observation ratio at Jungfraujoch for clear-sky conditions around noon are shown, illustrating this seasonal cycle with a strong amplitude. The erythemal UV observations, made at large solar zenith angles (winter) are significantly lower than the model results, while they are on the same order for other periods. For this assessment, the seasonal cycles in aerosols (except for OTL), albedo and total ozone were considered in the radiative transfer model. This seasonal pattern is in agreement with the angular response of the MeteoSwiss SolarLight biometers, which are found to be smaller than the nominal cosine response for large solar zenith angles (cf. Gröbner et al., 2006).

These seasonal structures in the model-to-observation ratio preclude temporal analysis and lead to a strong reduction of the data suitable for scientific studies. Therefore, a post-processing strategy was devised for correcting older data and bringing their quality to a level more consistent with newer data. The corrections (post-Coscor, post-f_n),

described below in Section 2.3.b are based on available calibration data. The proposed procedures use some of the elements presented in Equation (2.1) but apply the corrections on already calibrated data. A special situation is found for Davos, where between April 1999 and August 2006 the same biometer has been installed for measuring erythemal UV irradiance. This biometer (SL 1085) was fully characterized during the COST-726 inter-comparison campaign at the PMOD/WRC Davos in 2006. Because this instrument was relatively stable over this long time period and the characterization for producing Level-A data quality became available, this calibration is applied on the data over the whole time period analyzed in this study. Therefore, no further corrections are required for the data at Davos (cf. Figure 2.4).
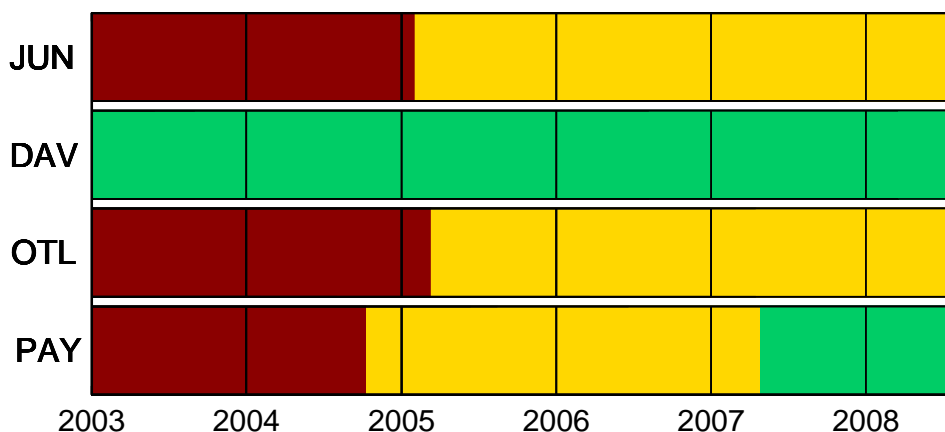

FIG. 2.4: Temporal evolution of UV data quality levels at the four SACRaM stations (JUN: Jungfraujoch, DAV: Davos, OTL: Locarno-Monti, and PAY: Payerne). red: Level C, yellow: Level B, green: Level A.

2.3.b Post-processing of UV measurements

The Level B data are post-processed using a cosine correction ("post-Coscor"); the older Level C data are additionally corrected for deviations of the spectral filter from the CIE erythemal action spectrum ("post-f_n"):

post-Coscor:
The angular characterizations of 23 biometers of MeteoSwiss are available for this post cosine correction. Additionally, an average cosine correction is calculated, using the data of three MeteoSwiss reference instruments (SL 8891, 1903, 1904). This average curve is applied on data from instruments, for which no proper cosine characterization is available. The calibration constants used in Level B and C data include already an unknown cosine correction because they were derived from comparisons against references over various solar zenith angles. These constants led at the time of calibration to the best agreement with the used reference. Therefore, the application of a new post cosine correction must not change the absolute level of the calibrated data. This is attempted by calculating an integrated daily cosine correction factor for each instrument separately ($\overline{\text{Coscor}_{\text{inst}}}$):
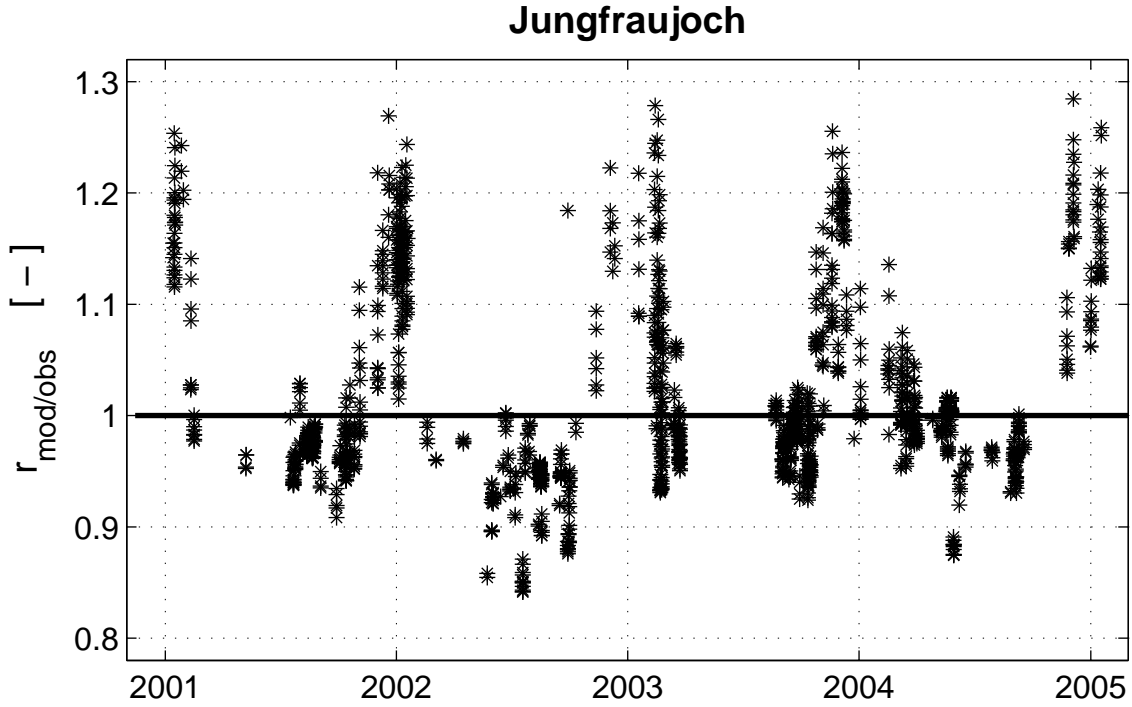
Jungfraujoch

FIG. 2.5: Time series of model-to-observation ratio ($r_{mod/obs}$) at the Jungfraujoch for clear-sky conditions between January 2001 and 2005. Only data around noon (9-13 UTC) is shown.

$$\text{post-Coscor}_{\text{inst}}(\theta) = \text{Coscor}_{\text{inst}}(\theta) \cdot \overline{\text{Coscor}_{\text{inst}}}$$

$$\text{where} \quad \overline{\text{Coscor}_{\text{inst}}} = \frac{\int_{\theta_1}^{\theta_2} I(\theta)\, d\theta}{\int_{\theta_1}^{\theta_2} I(\theta)\, \text{Coscor}_{\text{inst}}(\theta)\, d\theta} \tag{2.2}$$

θ_1 and θ_2 represent the range of solar zenith angles, considered to be representative for the springtime conditions when calibrations take place at MeteoSwiss, Payerne (37-70°). $I(\theta)$ is the clear-sky UV radiation, estimated by the radiative transfer model. $\text{Coscor}_{\text{inst}}(\theta)$ is the angular characterization for the instrument (or, an average cosine error in case no instrument-specific cosine characterization is available).

post-f_n:
The post-f_n correction is very similar to the post-Coscor described above. Again the data is corrected with an instrument-specific f_n characterization if available, otherwise an average f_n correction is applied. In order to minimize a possible change in the absolute radiation levels due to this correction, the data is again multiplied with an integrated diurnal $\overline{f_{n\ \text{inst}}}$ factor:

$$\text{post-f}_{\text{n inst}}(\theta) \quad = \quad \text{f}_{\text{n inst}}(\theta) \cdot \overline{\text{f}_{\text{n inst}}}$$

$$\text{where} \quad \overline{\text{f}_{\text{n inst}}} \quad = \quad \frac{\int_{\theta_1}^{\theta_2} I(\theta)\, d\theta}{\int_{\theta_1}^{\theta_2} I(\theta)\, \text{f}_{\text{n inst}}(\theta)\, d\theta} \qquad (2.3)$$

The observed UV radiation available on quality level C and B is post-processed using the post-Coscor characterization during clear-sky situations (Equation (2.2)). The Level C data is additionally modified for all-sky conditions with the post-f_n correction (Equation (2.3)). While the formerly applied $\overline{\text{Coscor}_{\text{inst}}}$ and $\overline{\text{f}_{\text{n inst}}}$ reduce possibly introduced offsets due to post-Coscor and post-f_n corrections for each instrument separately, a C_{sta} factor is applied on the whole data set from a given station including data of different instruments for avoiding a bias between observations and the model. These C_{sta}-factors adjust the median ratio between modeled and observed erythemal UV radiation to one. However, the effect of this correction is relatively small, since the values of C_{sta} are close to one (0.97-1.02).

$$\text{UV}_{\text{cor}} = C_{\text{sta}} \cdot \text{UV} \cdot \left\{ \begin{array}{ll} \text{post-Coscor}_{\text{inst}} & \text{if clear-sky} \\ 1 & \text{if cloudy} \end{array} \right. \cdot \left\{ \begin{array}{ll} \text{post-f}_{\text{n inst}} & \text{if Level C} \\ 1 & \text{if Level B} \end{array} \right. \quad (2.4)$$

2.3.c   *Evaluation of post-processed UV data*

The effects of the post-processing, presented in Equation (2.4), are assessed by comparing the originally calibrated (UV) and the corrected data (UV_{cor}) against estimations of the RTM for clear-sky conditions. The dependency of the ratio between modeled and observed UV radiation ($\text{r}_{\text{mod/obs}}$) on the solar zenith angle could be strongly reduced by the correction of the original UV data. As an example, this dependency is shown for the data at the Jungfraujoch on Figure 2.6. Using the originally calibrated data, $\text{r}_{\text{mod/obs}}$ clearly increase toward large SZAs (red), while the SZA-dependency is much weaker when the corrected data (black) is used to build $\text{r}_{\text{mod/obs}}$. The post-processing reduced the standard deviation of $\text{r}_{\text{mod/obs}}$ at Payerne, Locarno-Monti and the Jungfraujoch by 35 to 44% (Table 2.4). As described above, no correction was necessary at Davos. Furthermore, the standard deviation of $\text{r}_{\text{mod/obs}}$ for corrected data is on the same order as this for Davos, where the full calibration procedure (Equation (2.1)) was applied. This suggests that the proposed post-processing leads to a data quality comparable to the one we expect in the future, using the QA/QC procedures proposed by Webb et al. (2007).
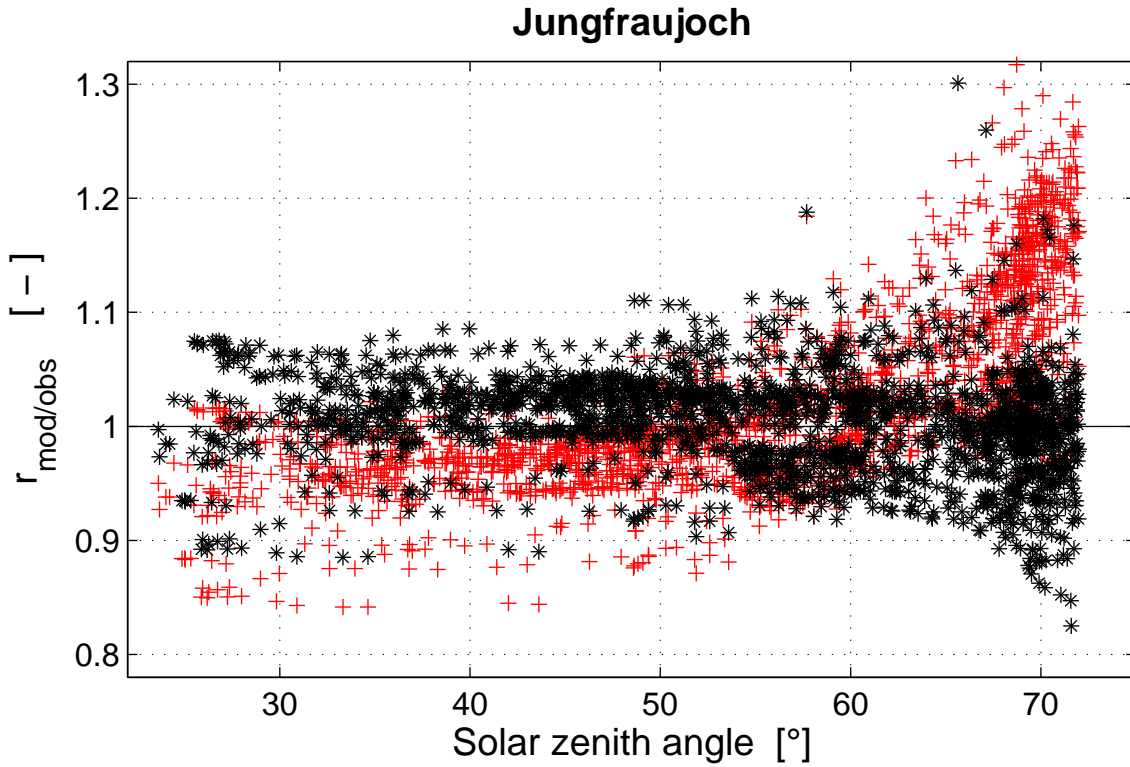
FIG. 2.6: Model-to-observation ratio ($r_{mod/obs}$) at the Jungfraujoch vs. the solar zenith angle between January 2001 and 2005 around noon (cf. Figure 2.5). Red: originally calibrated data, black: post-processed data using Equation (2.4).

TABLE 2.4: Standard deviations of the UV model-to-observation ratios ($r_{mod/obs}$) for originally calibrated and corrected UV data. For Davos, no correction of the data was required because the full characterization (Equation (2.1)) has been applied over the whole analyzed period.

	original	corrected	Δ	
Payerne	0.0691	0.0409	-0.0282	-41%
Jungfraujoch	0.0856	0.0477	-0.0379	-44%
Locarno-Monti	0.1102	0.0711	-0.0391	-35%
Davos	0.045	0.045	±0.0	±0%

Chapter 3

Regional snow distribution and evolution in Switzerland between 1980 and 2008

Daniel M. Walker[1,3], Laurent Vuilleumier[1], Christoph Marty[2], Stefan Brönnimann[3], and Ulrike Lohmann[3]

ABSTRACT

The reflectivity of the earth's surface plays an important role in the determination of the energy budget. We present a method for estimating the spatial distribution of snow, which is crucial for determining surface albedo and therefore for modeling radiation fluxes in the atmosphere. Long-term data sets of this type at high temporal and spatial resolution are rare.

Daily snow cover over Switzerland is estimated using a method based on linear regression of observed snow depth vs. altitude. This study considers exclusively stations, which measured snow over more than 25 winter seasons providing a stable data set since 1980. In a cross-validation over the whole time period, a probability of detection of 0.96 and a false alarm rate (FAR) of 0.15 were obtained. The FARs are higher in the northern part of Switzerland where the orography is lower and snow is infrequent. Over the whole area studied, snow was overestimated by 5%. Another validation of modeled snow coverage against satellite observations yielded an agreement between 69 and 97%. The two independent validations demonstrated that this method successfully describes the spatial and temporal variability of snow in the complex terrain of Switzerland back to 1980. Furthermore, it is capable to respond to sudden changes in meteorological conditions such as snowfall events.

The regional snow coverage was investigated for temporal trends using Mann-Kendall tests. Negative trends of -10% and -15% were found for the northern part of Switzerland, while the changes in more elevated alpine regions were weaker and non-significant.

---

[1]Federal Office of Meteorology and Climatology MeteoSwiss, Payerne, Switzerland

[2]WSL Institute for Snow and Avalanche Research SLF, Davos, Switzerland

[3]Institute for Atmospheric and Climate Science, ETH Zurich, Zurich, Switzerland

3.1   Introduction

The spatial distribution of snow plays an important role in various scientific disciplines, such as atmospheric science. The presence of snow has a strong impact on the surface reflectivity and consequently on the surface energy budget. Furthermore, due to multiple reflections between the atmosphere and the surface, it also influences the diffuse part of downward radiation. The local surface albedo is mostly determined by the presence and absence of snow. This binary character of the local albedo is more strongly pronounced for ultraviolet radiation (UV) than for the total solar radiation. Most soil types show very low reflectivities in the UV range (< 0.1) that differ only slightly one from another while for fresh and dry snow, albedos larger than 0.9 were found in high mountain areas (Ambach and Eisner, 1986; Blumthaler and Ambach, 1988; Schmucki et al., 2001). Thus, the soil type plays only a secondary role in the determination of the UV-albedo. In order to estimate the average albedo around a certain location, the most important requirement is assessing the regional distribution of the snow cover.

Various authors investigated how regional snow distribution can be inferred using a wide range of ground-based methods. Due to the complex nature of the spatial snow variability, it is very difficult to model snow depth in an alpine topography. As a consequence, various studies exhibited markedly different performances in estimating snow depth, snow density or the snow-water equivalent. In a study of snow distribution in the Colorado Rocky Mountains, Erxleben et al. (2002) could not even explain one-third of the variance in observed snow depth even with the most accurate method they used. On the other hand, López-Moreno and Nogués-Bravo (2005) obtained a cross-validation R^2_{adj} of 0.67 in the Spanish Pyrenees. Recent studies compared the results of different interpolation techniques such as local methods (e.g. inverse distance weighting, splines), geostatistical approaches like kriging, and global methods including regression trees, linear models or generalized additive models (Erxleben et al., 2002; López-Moreno and Nogués-Bravo, 2006). Non-parametric regression trees and generalized additive models demonstrated good results in several studies (López-Moreno and Nogués-Bravo, 2005), and their performances even improved when kriging-methods were applied on the residuals (Balk and Elder, 2000; Molotch et al., 2005). Purely geostatistical and local methods were less successful in modeling snow depth (López-Moreno and Nogués-Bravo, 2006). When applying a linear regression model on observed snow depth, the altitude exhibited the highest correlation coefficient of a set of independent variables because of its direct control over the temperature pattern (López-Moreno and Nogués-Bravo, 2006). Foppa et al. (2007b) investigated the synergy of in situ and space borne observations for snow depth mapping in the Swiss Alps. Their approach uses the dependence between snow depth and altitude in combination with information of nearby observations. In addition, they include satellite information for identifying snow-free conditions during clear-sky periods at irregularly distributed locations. In a case study including four selected days in winter 2005, R^2 values between 0.61 and 0.74 were reached. More information about the major patterns of winter snow variability in Switzerland and trends in the occurrence of days with snow are presented by Scherrer and Appenzeller (2006) and Scherrer et al. (2004). In a principle component analysis, three major patterns were isolated explaining almost 80% of the variance in days with snow coverage. Only the altitude related pattern showed a weak negative trend between 1958 and 1999, which is well correlated with an increase of the

0 °C isotherm altitude from ∼600 to ∼900 m MSL in the same period.

In contrast to the previous studies, our application in atmospheric radiation modeling does not need snow depth but an efficient method describing the snow distribution (snow/no snow) within large geographic regions. Furthermore, we need an approach that would present a relatively stable performance when applied to the previous decades and that would not be influenced by adverse weather conditions. Particularly, its performance should be as independent as possible of the availability of satellite data. Additionally, it should feature a high temporal resolution for detecting daily changes in the regional snow coverage. In this study, a method is presented for deriving the daily altitude of the snow line in Switzerland, which is validated against snow measurements and satellite snow masks. The chosen technique is based on a robust linear regression model and focuses on elevation as physical parameter to describe the spatial occurrence of snow. The snow line altitude is calculated for five different regions representing the variable climate conditions of Switzerland. The application of a global interpolation method leads to very short data processing times and the long time series of measured snow depth allow the application of this method back to 1980. In combination with a digital elevation model, snow flags can be assigned to any location differentiating between snow-covered and snow-free surfaces. The resulting snow information is used to infer the spatial distribution of the surface reflectivity needed for radiative transfer calculations.

The following section describes the data used in this study and the analysis technique. Section 3.3 presents two examples of applications and the validation of the method. The temporal evolution of the regional snow coverage is analyzed in Section 3.4. Finally, the results are discussed and conclusions are drawn in Section 3.5.

3.2 Data and method

3.2.a Data

The presented analysis is based on daily snow depth measurements (morning observations) and data from a digital elevation model. The snow data are provided by the Federal Office of Meteorology and Climatology MeteoSwiss and the WSL Institute for Snow and Avalanche Research (SLF). The analysis concentrates on the winter seasons (November-April) between November 1980 and April 2008. In order to ensure uniform conditions over the whole investigation period, only data from stations covering more than 25 winter seasons are incorporated. The used data set includes a total of 125 stations in the Swiss lowlands and the Alps, 45 of which are operated by MeteoSwiss and 80 by the SLF (Figure 3.1). The MeteoSwiss data was checked for unusually large day-to-day differences. In 23 cases the measured snow depths presented suspicious anomalies and were excluded from our data set. However, in some of these cases the human observer obviously confounded the digits and these data were replaced by the realistic values. The SLF snow data underwent a quality control chain, which checks each value for plausibility including unusually large day-to-day differences. An overview about snow measurements in Switzerland is given by Auer et al. (2004).

Digital elevation models (DEMs) provide topographic information that we use to derive the regional snow distribution. We chose the gtopo30 data set, which is freely available at
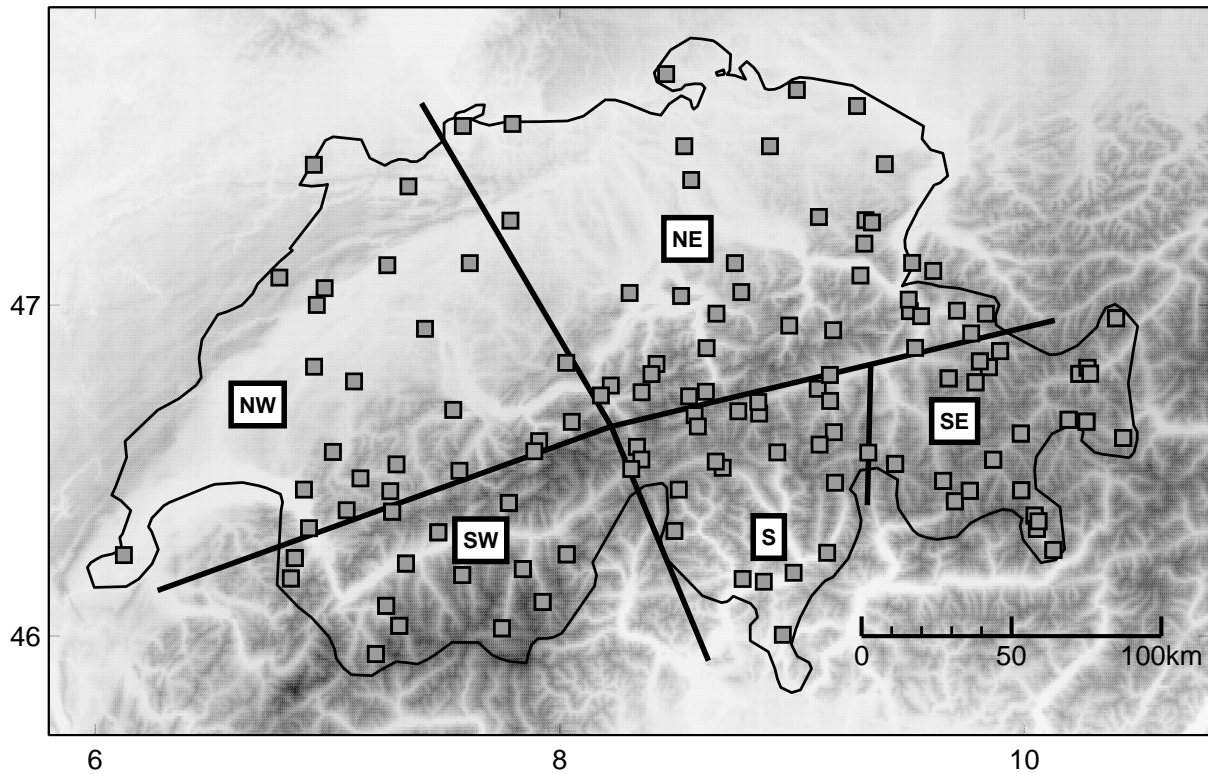
FIG. 3.1: Map of Switzerland showing the different regions and the stations providing snow depth data for this study. The regions are NE: lowlands north-east, NW: lowlands north-west, SW: south-western part (mainly canton Valais), S: southern part (mainly canton Ticino), and SE: south-eastern part of Switzerland (mainly canton Graubünden).

the Center for Earth Resources Observation and Science (EROS) at the U.S. Geological Survey. This DEM provides worldwide grid point altitudes with a horizontal resolution of 30 arc seconds, corresponding to $\sim$640/940 m east-west/south-north within our study area. For this analysis the data are interpolated onto a regular 200 x 200 m^2 grid, using cubic interpolation. The resulting topographic data set has been validated at the locations of meteorological stations in Switzerland (n=141) and average deviations of 3 ± 40 m and -57 ± 141 m (mean $\pm$ std dev) were found for locations below and above 700 m MSL, respectively.

3.2.b   Method

The goal of the current study is to derive the daily regional snow distribution for Switzerland. For this purpose we calculate, for each day t, a binary snow map based on the assumption that a unique snow line altitude (SL) exists, separating snow free and snow covered conditions, i.e., if a location (x,y) is below the snow line it is snow free and if it is above, it is snow covered:

$$
\begin{aligned}
s(x,y,t) &= 1 \quad \text{if } \mathrm{elev}(x,y) \geq \mathrm{SL}(x,y,t) \\
s(x,y,t) &= 0 \quad \text{if } \mathrm{elev}(x,y) < \mathrm{SL}(x,y,t)
\end{aligned}
$$

where $s(x, y, t)$ is the binary snow flag and $\mathrm{SL}(x, y, t)$ the snow line altitude for a given location and day. The altitudes $\mathrm{elev}(x, y)$ are derived from the topographic data set. It is then assumed that the snow line altitude $\mathrm{SL}(x, y, t)$, for a given day, does not vary much in space so that it can be approximated by regional values:

$$\mathrm{SL}(x, y, t) \cong \mathrm{SL}(r, t) \qquad \text{region:} \quad r = 1, \dots, 5$$

For this purpose, Switzerland was divided into five different geographic regions (Figure 3.1). This choice was prompted by striking a balance between the need to accurately describe different climate conditions in Switzerland, while maintaining a sufficiently high number of observation stations in each region. The chosen regions account for the different climate conditions on the northern and southern parts of the alpine ridge and the typical west-east orientation of weather patterns in Switzerland. In addition, dividing Switzerland into five regions ensures a reasonable number of observation stations within each area, which helps reducing the number of cases where a lack of data hampers obtaining accurate results. For each region and day, the altitude of the snow line is calculated using a robust linear regression of snow depth measurements (SD) vs. the altitudes of the observing stations (elev):

$$\mathrm{SD}(x, y) = b + a \cdot \mathrm{elev}(x, y) + \epsilon$$

yielding the coefficients a and b for each region and day: $a_{r,t}$ and $b_{r,t}$. The robust regression method uses an iteratively reweighted least squares algorithm, with the weights calculated by applying the bisquare function. This approach assumes a linear increase of snow depth with altitude. This is reasonable since the median correlation between snow depth and altitude over all regions amounts to 0.77 for winter days (November - April). López-Moreno and Nogués-Bravo (2006) also found such a strong relationship, the elevation being the variable with the highest correlation coefficient with snow depth in a stepwise linear regression model. The altitude of the daily snow line for each given region is inferred using:

$$\mathrm{SL}_{r,t} = \frac{\theta - b_{r,t}}{a_{r,t}} \tag{3.1}$$

where $\mathrm{SL}_{r,t}$ is the altitude of the snow line within the region r at day t. The value of θ represents a threshold to separate snow from snow-free conditions, which is set to 0.05 m similarly to Hantel et al. (2000) in their study of snow cover climate sensitivity. The estimated altitudes of the snow line are then related to the Swiss topography and daily snow maps (constituted of binary pixels) are calculated. Appendix A describes how specific problems such as data shortage or inverse regression slopes are handled by the algorithm.

3.3   Applications and validation

The method presented above can generate time series of snow line altitudes and, in combination with a digital elevation model (DEM), the spatial snow distribution within the five defined regions of Switzerland. Two examples of applications are presented below, followed by a validation of the method including both cross-validation and comparison with satellite data. In the cross-validation, 28 winter seasons of modeled snow data are compared with observations, while the satellite validation concentrates on case studies between 2002 and 2005.

Figure 3.2 shows an example of the evolution of the daily snow line since November 1980 in the south-western part (SW) of Switzerland. In this region, the altitude of the snow line drops in November from its climatological summer value (cf. Appendix A) to lower altitudes. Usually in the time period between mid to end of March the snow line starts climbing back to higher altitudes. The results of this method suggest a change in the springtime snow-retreat pattern in the SW-region in the late 1980s. While during most days in March between 1981 and 1988 snow was generally present below 800 m MSL, the number of days in this month where snow has already retreated to higher altitudes clearly increased after 1989. This change is investigated in more detail using trend analysis later in Section 3.4. Furthermore, the time series of this region illustrate some interesting examples of snow-events such as sudden drops of the snow line. This happened for example in mid November 1999 with a heavy onset of the winter-season or in December 1994 when snow was reported down to low altitudes after a cold front (see red boxes in Figure 3.2). These examples illustrate that our method responds to sudden changes in weather conditions.

An example of a calculated regional snow distribution for March 15, 2004 is shown on Figure 3.3 (upper panel). While the regression method leads to complete data sets, the satellite source used for validation (lower panel) shows regions without valid snow data due to cloud coverage. For a comparison, the modeled snow data sets are reduced to the valid satellite data. The general structure of the snow distribution as determined by the satellite is well reproduced by our model. Furthermore, the use of a DEM allows resolving the distinctive topographic features of Switzerland such as valleys and mountain ridges (e.g. Alps, Jura).

As mentioned above we validate our method using a cross-validation procedure within our data set on one hand, and comparisons of our snow maps with satellite-derived ones on the other hand. The underlying idea of cross-validation is the repeated separation of the whole data set into developmental and verification subsets (Wilks, 1995) by removing in turn each single station from the developmental subset and using it for verification. Knowing the time periods when the surface is actually snow covered from observations at a given station, the derived snow-flags at the altitude of the validating station are verified using the remaining data set. Analyzing categorical results (snow/no snow), contingency tables are calculated and verification measures such as hit rate (HR), probability of detection (POD), false alarm rate (FAR), and bias (B) are derived. The HR is the fraction of correct snow and no snow predictions, while POD is the likelihood that snow for a given station/altitude is predicted, given that snow is observed for this case. On the other hand, FAR is the fraction of snow predictions for which there are no corresponding observations.
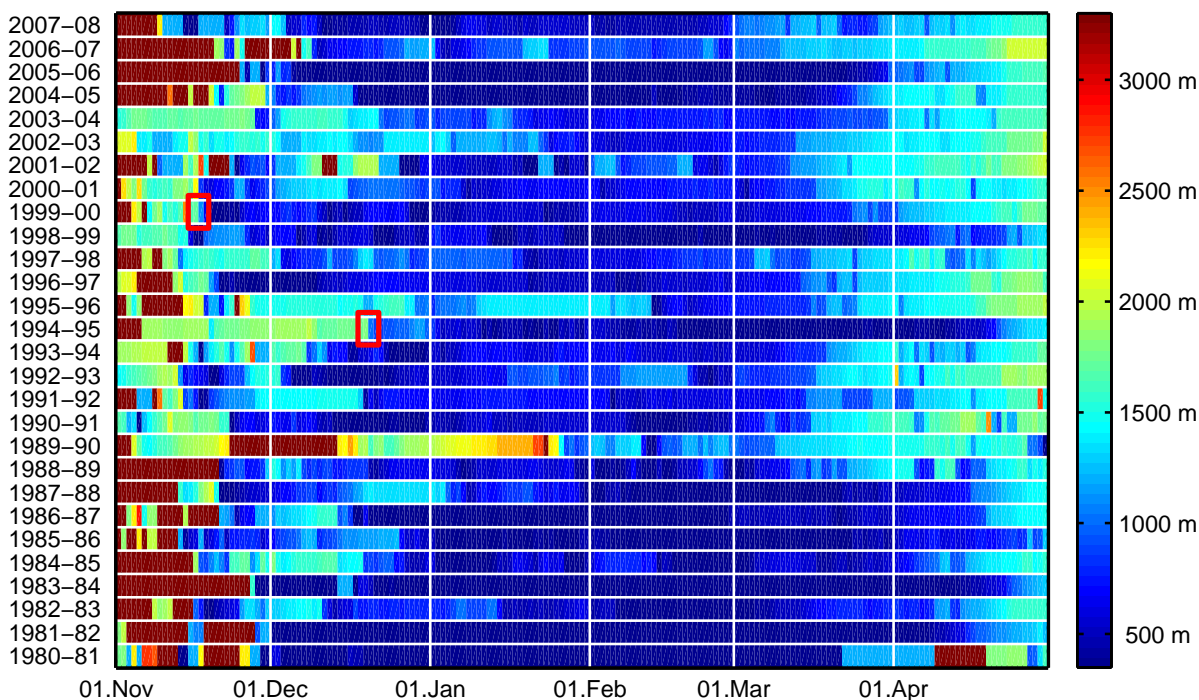
FIG. 3.2: Evolution of the snow line in the SW-region (south-western part of Switzerland) since winter 1980/81. The colors refer to the snow line altitude [m MSL] on a daily base. The red markers indicate examples with large steps in the snow line altitudes due to changes in the meteorological conditions (snowfall).

While HR is giving the same weight to both snow event and non-event, skill factors like POD and FAR are focusing on the presence of snow. Additionally, as proposed by Wilks (1995), B is the ratio of the number of snow forecasts to the number of snow observations and is one for unbiased forecasts.

The results of the cross-validation are presented in Table 3.1. Within each region, the different skill measures (HR, POD, FAR, and B) are computed for each station in turn, using all the other stations in the region to make a prediction for the station under review. Table 3.1 gives the medians of the skill factor distributions over all stations in a region. The hit rates (i.e. the proportions of correct forecasts) are high with values above 0.87. The probability of detection of snow exceeds 0.90 and is better in the alpine regions (SW, S, and SE) with medians higher than 0.96. Combining all regions, an overall median POD of 0.96 and FAR of 0.15 are obtained. The biases in all regions are above one, and indicate that the method tends to more often forecast the presence of snow than it actually occurred. While the bias in the NE region is close to one, snow is overestimated in the SE and S region by 8 and 12%, respectively. The median FAR and bias over all regions increase by 6 and 3%, respectively, when the analysis is restricted only to March and April. Thus, the overestimation of snow is more pronounced when the cross-validation is limited on late winter periods where snow is rare at low altitudes.

Figure 3.4 shows the distribution of the PODs and FARs in the different regions as boxplots. The model performs better in the alpine regions (SW, S, and SE) than in the

Swiss lowlands (NE and NW), which is discussed later in Section 3.5. The distributions of the PODs and FARs are broader (interquartile range) in the lowlands than in the alpine regions. In the SW and SE-region, the POD and FAR are close to one and zero, respectively, and their distributions are well separated. The highest POD is reached in the south-eastern region and the lowest FAR in the south-western part of Switzerland.
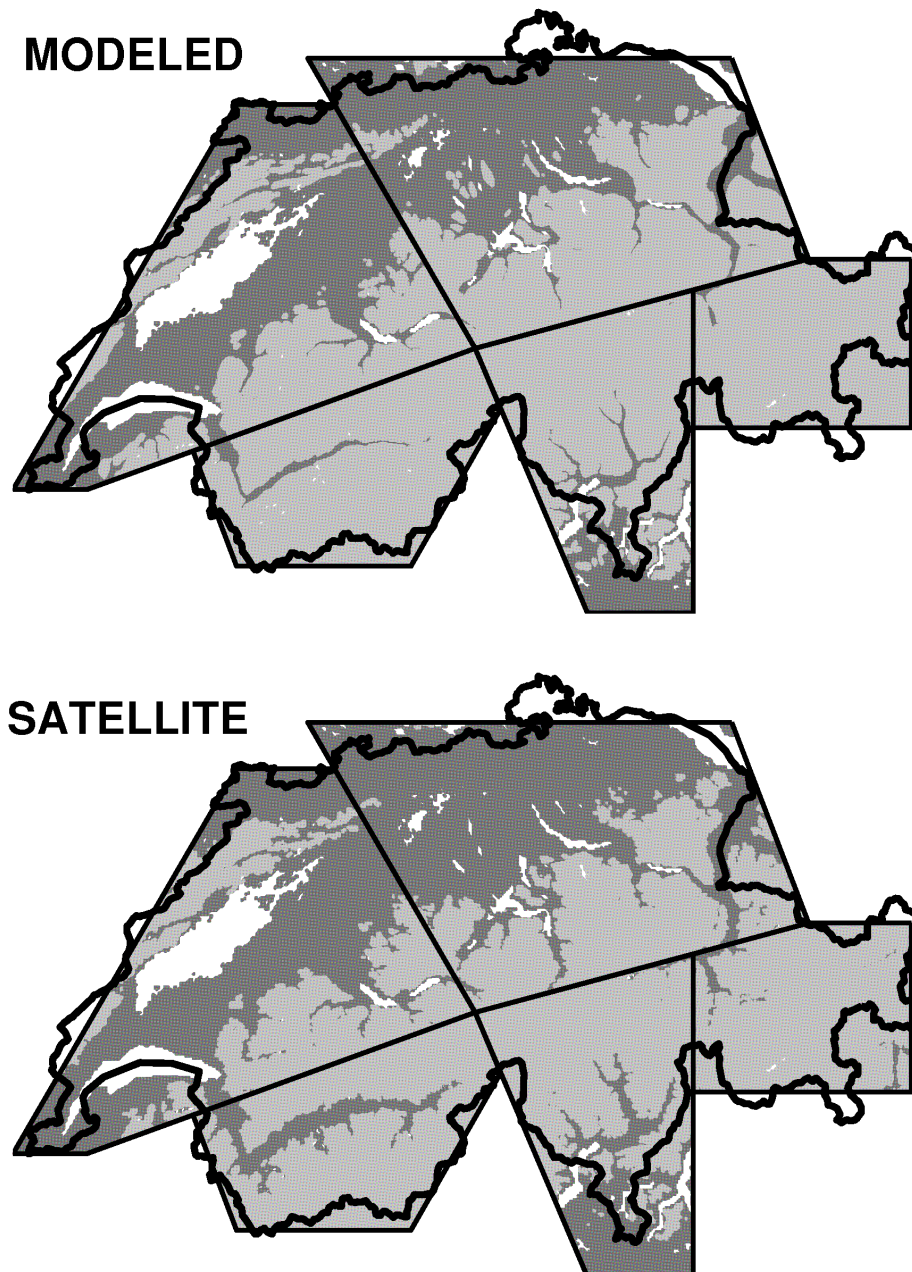

FIG. 3.3: Snow distribution (15 March 2004) inferred with our robust regression method (top panel) and from satellite data (bottom). Snow covered areas are shown in light and snow-free in dark gray. White pixels refer to regions for which satellite snow-cover data were not available (clouds or over water).

TABLE 3.1: Medians of the different skill scores resulting from cross-validation for each of the five regions (see Figure 3.1). HR: hit rate, POD: probability of detection, FAR: false alarm rate, B: bias, n: number of stations. On the last row, the median skill factors over all stations of all regions are shown.

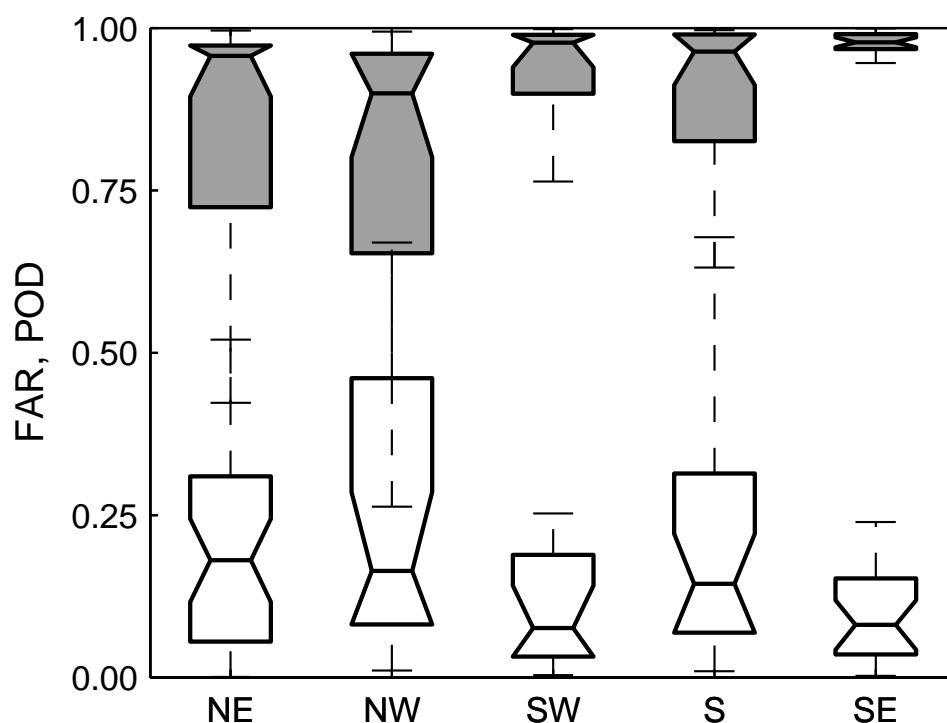|		HR	POD	FAR	B	n
north-east	NE	0.92	0.96	0.18	1.01	39
north-west	NW	0.92	0.90	0.16	1.04	24
south-west	SW	0.87	0.98	0.08	1.05	14
south	S	0.88	0.96	0.14	1.12	25
south-east	SE	0.90	0.98	0.08	1.08	23
		0.91	0.96	0.15	1.05	125

FIG. 3.4: Probability of detection of snow (POD, gray) and false alarm rate (FAR, white) for all regions. The boxplots characterize the distribution of the respective skill measure resulting from cross-validation. The horizontal lines of the boxes represent the lower, upper quartile and the median. The notches indicate a robust estimate of uncertainty about the medians. Not overlapping notches state that the medians differ at the 5% significance level. The whiskers represent the range of the most extreme data value from the box within 1.5-times the interquartile range of the sample.

In a second step, the resulting regional snow distributions are compared against satellite data in four case studies between November 2002 and March 2005 (one example is shown on Figure 3.3). The criteria for the four case studies were on one hand choosing interesting regional snow distributions, including snowfall events and on the other

hand analyzing different snow situations in the lowlands and the alpine regions. Furthermore, the choice was limited by the requirement of clear-sky conditions over wide areas of Switzerland for obtaining good satellite coverage. The case studies are distributed over four years and are therefore independent. As reference satellite information, we use the operational sub-pixel snow mapping product described by Foppa et al. (2004). This product is based on observations from the multi-spectral sensor AVHRR (Advanced Very High Resolution Radiometer) on board the NOAA-17 satellite with a spatial resolution of 1.1 km at nadir. Foppa et al. (2007a) validated the AVHRR snow retrievals against high resolution reference data from the Advanced Spaceborne Thermal Emission and Reflection Radiometer (ASTER). The two data sets were compared for three different test sites in the European Alps and an overall correlation of 0.78 and a mean absolute error of 10.44% fractional snow cover were found. Terrain effects and forested areas reduce the agreement with the reference ASTER data and influence the accuracy of the AVHRR subpixel snow retrievals.

For the comparison with our modeled snow distributions, the fractional snow information are interpolated onto a regularly spaced grid, corresponding to the gtopo30-regridding (mentioned above). A threshold of 15% fractional snow-coverage is used to translate the satellite snow data into binary snow flags (Foppa et al., 2004). We use a post-agreement (PAG) assessment of the performance of our method by comparison to satellite data. The PAG describes the number of correct forecasts divided by the number of forecasts in each category and thus is the complement of the FAR; PAG=1-FAR (Wilks, 1995). In our analysis, this corresponds to the fraction of snow-flags (snow/no snow) assigned by our method that coincide with satellite snow-flags. For this validation we exclude a vertical transition zone, centered around the estimated snow line altitude, including 5% of the topography in the region. Snowflags within this transition zone are not used for validation because the real snow line is not a strict horizontal separation and therefore local effects are dominant around the snow line altitude.

Table 3.2 summarizes the results of this validation for the different regions and cases. For case #1, two overpasses have to be combined due to clouds in order to obtain a more complete data set over Switzerland. For four case-region combinations, the predicted snow line is either too low or too high to validate modeled snow-free or snow-covered areas, respectively. Depending on the region, the fractions of correctly modeled snow-free areas range on average between 0.91-0.97 (PAG). For forecasted snow-covered surfaces the agreement with the satellite observation is between 0.69-0.85. The March 2004 (#3) case study gives the best results with PAGs on the order of or above 0.9, while the least satisfying performances in snow modeling are found for the March 2005 case (#4). In all regions and for both forecast categories (snow/no snow) the average PAGs over all cases exceed 0.69 and the overall average is 0.86.

3.4   Trend analysis

As mentioned in Section 3.2.a, this study is based on a set of stations that has been stable on the period 1980-2008, and there was no significant change in the measuring technique. Thus any temporal evolution in the data is likely to be real, and not an artifact of data density or change in the measuring technique. In addition, the previous section verified

TABLE 3.2: Post-agreement between inferred snow-coverage and satellite data (PAGs). Left side: the ratio of correctly inferred snow-free (flag = 0) to all snow-free modeled pixels, right side: idem for snow-covered pixels (flag = 1). Last row: the average PAGs for each region. Case #1: 1/8 November 2002, #2: 24 February 2003, #3: 15 March 2004, and #4: 21 March 2005.

	p(obs=0 | mod=0)					p(obs=1 | mod=1)				
	NE	NW	SW	S	SE	NE	NW	SW	S	SE
#1	0.98	1.00	0.99	0.93	0.98	0.69	0.71	0.64		0.67
#2	0.65	0.90	0.82	1.00		0.89	0.82	0.92	0.71	0.91
#3	1.00	0.97	1.00	0.99		0.81	0.85	0.90	0.90	0.96
#4	1.00	0.99	1.00		0.96	0.58	0.67	0.82	0.47	0.86
	0.91	0.97	0.95	0.97	0.97	0.74	0.76	0.82	0.69	0.85

that a binary pixel-wise snow cover information can be satisfactorily deduced from the data. This snow cover information is therefore well suited to be investigated for possible trends related to climate change.

The regional snow coverage is calculated by relating the snow covered area to the total surface of each region (horizontally projected). Statistically significant ($p < 0.1$) trends in the mean snow covered area during the winter seasons (November-April) are assessed with the non-parametric Mann-Kendall test (Mann, 1945; Kendall, 1955) for each region separately. Mann-Kendall tests are based on the ranking of the data and not their value, and can therefore be used even when uncertainties are not normally distributed. Monotonic trends are expressed as a percentage change from their initial values based on the Theil-Sen slope estimation (Theil, 1950; Sen, 1968). Such an estimator is based on the median of multiple slopes derived from all possible time-ordered observation pairs, and is specifically designed for the Mann-Kendall test.

The investigation reveals that the NE- and NW-region show a significant decrease (p=0.08 and 0.05, respectively) in snow coverage for the investigated winters between November 1980 and April 2008. They experienced a decline of -10 and -15%, respectively, during the 28 years of the study period. The three other regions also show a decrease in snow coverage. However, the trends are weaker (between -1 and -8%) and not significant. The different behaviour of the northern and southern regions as defined in this study is caused by the fact that the two northern regions comprise the whole Swiss plateau (i.e. a lot of low altitude stations), whereas the three southern regions cover the majority of the Swiss Alps. This explanation is corroborated by the fact that the S-region, which comprises the most low altitude stations of all three southern regions (Figure 3.5), shows the largest negative trend of these three regions. Therefore, the different behaviour of the northern and southern regions is most likely related to the altitude dependency of the climate change signal on snow cover, which is stronger at low altitude. This result is confirmed by Scherrer et al. (2004), who investigated the snow coverage by calculating the number of snow days in Switzerland between 1958 and 1999. They found a significantly decreasing trend since the beginning of the 1980s at altitudes below 1300 m MSL, which they mainly attributed to increasing temperatures. Moreover, Marty (2008) demonstrated with a more comprehensive data set (1948–2007) that this decrease is mainly caused by
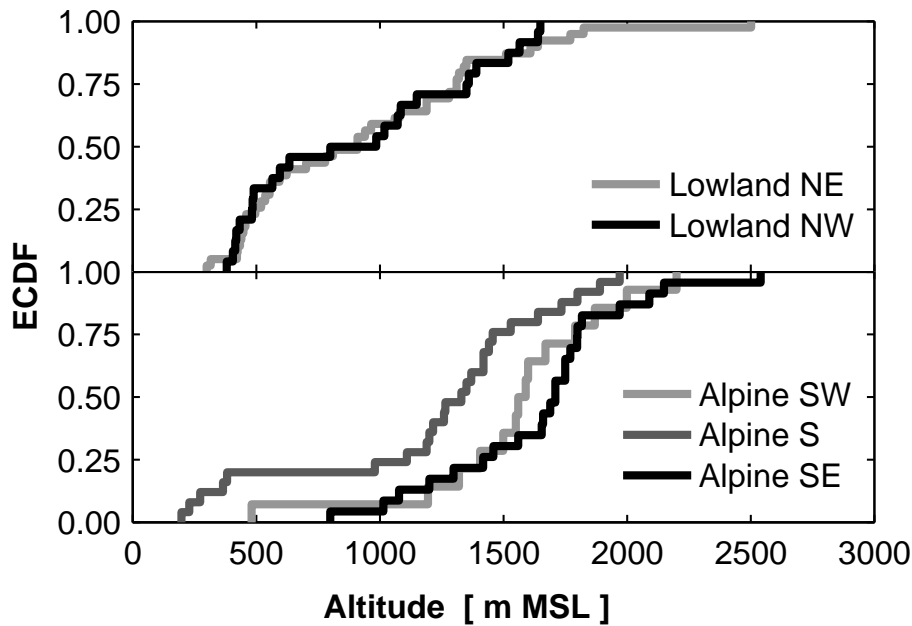
Fig. 3.5: Empirical cumulative density functions (ECDF) of the station altitudes for each region. Upper panel: lowland regions (NE and NW); lower panel: alpine regions (SW, S, and SE).

a regime change at the end of the 1980s. This signal is also found in our study's time series. The Mann-Kendall test in the sequential version (Sneyers, 1992) was applied to the estimated snow coverage. This method takes into account the possibility of compensating trends occurring inside the analyzed time period. This is achieved by applying the trend test to the two partial time-series in which a point running from the beginning to the end divides the complete time-series. This analysis indicated that the decreasing trend of the snow coverage in the two northern regions is caused by a step-like change at the end of the 1980s.

The time series of the annual snow coverage of the regions NW and SE are shown in Figure 3.6 as an example. Both regions show a high year-to-year variability of the snow coverage, due to the high sensitivity of snow to temperature and precipitation anomalies. The main difference of the two regions is the absolute percentage of snow coverage. In the NW-region between 10 and 55% of the area can be snow covered, where as the SE region experiences between 75 and 95% in the same time period. The reason is again the different altitudinal distribution of the two regions. The highest values of the NW-regions are represented by the known snow-rich winters of 1981, 1999, and 2006 in this part of the country. On the other hand also the snow-poor winters of 1990 and 2007 stand out by their low percentage values. In the SE-region the snow coverage of winter 2007 is by far the lowest, mainly caused by warm temperatures and scarcity of snowfall up to the highest mountains. The other well-known snow-poor winter 1990 does not show especially low percentage in this region, because the snow scarcity was mostly limited to the lower altitudes due to warm temperatures, but almost normal amounts of snowfall. Moreover, the highest values of the SE-region correctly represent the winters 1982, 1991, 2001, and 2004, which were especially snow rich in this part of the country.
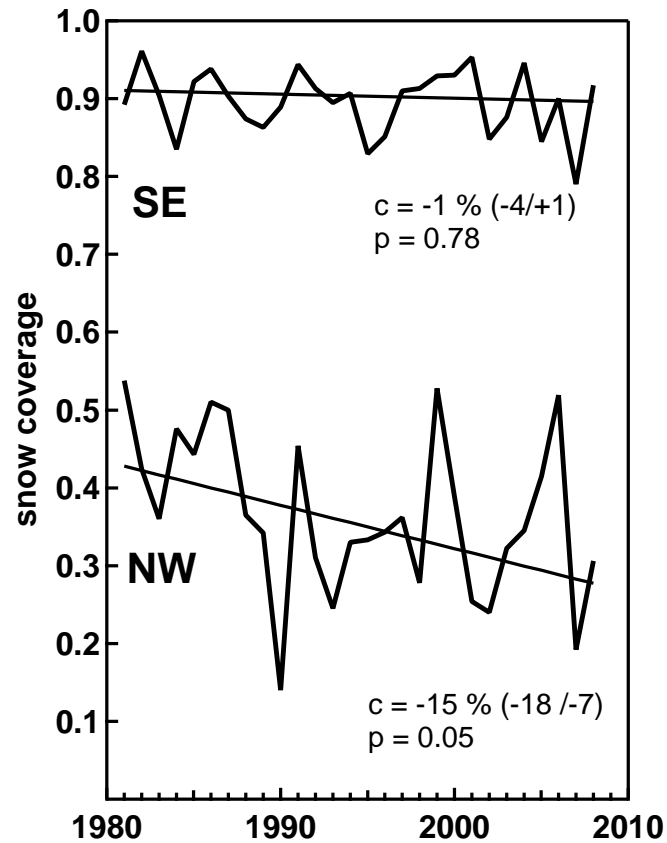
FIG. 3.6: Time series of the average winter snow coverage (November-April) for the SE-
and NW-region with the corresponding line of the Theil-Sen slope. The change c (and
its 95% uncertainty) based on this slope and the p-values from the Mann-Kendall trend
analysis are given in the graph.

3.5 Summary and discussion

The method described here allows deriving the snow line altitude within different regions
of Switzerland as function of time with a daily resolution. The snow line altitude is in-
ferred with a robust linear regression on the relationship between observed snow depth
and altitude. Combined with a digital elevation model, our method allows identifying
areas that are snow covered. The resulting spatial snow information can be used for esti-
mating the effective surface albedo needed for radiative transfer calculations. In contrast
to satellite products, the performance of this method is not influenced by clouds and
instrument related effects.

Time series of calculated snow line altitudes reproduce well the typical seasonal cycle
observed in Switzerland. Even sudden changes in weather conditions such as temperature
or heavy snowfall events can be identified in the inferred snow line. This method was
validated using two independent procedures: cross-validation and comparison of modeled
snow distribution with satellite snow masks.

Cross-validation for winter seasons (1980-2008) showed the median of the proportion of

correct forecasts (hit rate) to be on the order of or above 0.9. The probability of detection is high in alpine regions (0.96-0.98) and slightly lower in the lowlands (0.90-0.96). The median false alarm rates (FAR) amounts to 0.15. In the alpine south-eastern and southern part of Switzerland (SE and S) an overestimation of the presence of snow of 8 and 12% was found. The reason for these increased biases are mainly the validation results of some low-altitude stations that do not measure snow during periods when the regression model predicts snow at these altitudes. In general, skill factors and especially the FARs are less good for the lowest stations in the regions. Two factors can explain these lower performances: first, the measured snow quantities are generally small at low altitudes and frequently close to the detection threshold resulting in larger uncertainties. Second, since the snow amounts are low, local effects are more influential for explaining the absence or presence of snow at a given altitude, which lowers the performance of the robust regression. In the SW region a long narrow valley is the predominant topographic feature surrounded by high mountainous areas. However, only one station (Sion, 480 m MSL) represents the conditions found on lower altitudes. The influence of this station on the regression is limited when snow free conditions are present at low altitudes and therefore shows the weakest cross-validation results in this region. Similarly, an influence of an irregular altitude distribution of the stations within the S-region on the validation is found. In this region, there is a gap with no observations between ∼380 and 980 m MSL (Figure 3.5), and the few stations below 380 m show worse validation results than the upper stations. In addition, the S-region is the most inhomogeneous region seen from a climatological point of view. In the northern areas (NE, NW), more than 40% of the stations are located below ∼600 m MSL. At these low altitudes the observation of snow is relatively rare compared to alpine stations, which makes snow detection more difficult. The inferred snow distributions were also compared to satellite snow masks during four case studies between November 2002 and March 2005. Depending on the region, the post-agreement (PAG) between the two methods for snow-free areas ranged between 0.91 and 0.97, and between 0.69 and 0.85 for snow-covered areas. The best agreement between modeled and satellite-observed regional snow coverage was found for case #3 with PAGs between 0.81-0.96 for the detection of snow. The lowest performance of this validation occurred during case #4 in the southern region (S) where only 47% of the forecasted snow areas were actually snow covered. The snow line altitude was predicted too low in this region for this episode and therefore snow was overestimated. In this case, there was a weak correlation between altitude and snow depth, which could be related to the inhomogenety of this climate region and the strong warming during the whole week before.

The validation of this simple method showed, that it is possible to estimate the spatial and temporal variability of snow in Switzerland back to the early 1980s. The condition for its successful application is the possibility of defining relatively homogeneous climatic regions with snow depth observing stations that are well distributed in altitude. Particularly, this method is suitable for mountainous regions with a good network of stations where snow depth is recorded daily.

The average regional snow coverage has been calculated for the winter seasons between 1980 and 2008. Snow-rich and -poor winter seasons are well represented in the analyzed time series. The derived snow coverage over 28 years has been investigated for temporal trends using a non-parametric Mann-Kendall test and Theil-Sen slope estimations. Statistically significant ($p < 0.1$) negative trends of -10 and -15%, respectively, were found for the NE and NW regions over the analyzed time period. Decreasing snow coverage was

also found in the other three regions but these were weaker (between -1 and -8%) and not statistically significant. The decreasing trends in the northern lowland regions are in agreement with a previously found step-like regime change of snow days at the end of the 1980s that is more pronounced at low altitudes (Marty, 2008). This analysis shows that the derived data set enables the investigation of the temporal evolution of snow coverage in Switzerland including the detection of climate change effects on the presence of snow in the complex alpine topography.

Chapter 4

Cloud effects on erythemal ultraviolet (UV) and total solar radiation in Switzerland

Daniel M. Walker[1,2], Laurent Vuilleumier[1], Stefan Brönnimann[2], and Ulrike Lohmann[2]

ABSTRACT

Despite its small contribution to the total solar irradiance, UV radiation has important impacts on various ecosystems and public health. The available time-series in Switzerland are short and spatially sparse, and do not allow detailed studies concerning the temporal evolution and spatial distribution of UV radiation. For extending existing time-series and describing the spatial UV-variability, the adequacy of reconstruction techniques needs to be assessed. While radiative transfer models (RTMs) perform well in simulating clear-sky conditions, the treatment of cloud effects are challenging.

We present a method for reconstructing erythemal UV radiation during all cloud situations based on relationships between cloud modification factors in the total solar radiation (SW) and UV. The use of SW for describing the cloud effect in the UV is convenient since SW is measured at many locations and for long time periods. The semi-empirically derived relationships are tested for dependencies on various environmental factors with a special focus on the potential generalization for the different climate conditions found in Switzerland. We found the method being generally applicable at four Swiss stations situated in different climate settings.

Our method is capable to capture the short-term variability caused by changing cloud coverage and shows good agreement with observed UV at 10-minutes time resolution. RMS differences between 4.3–6.9 mW m^{-2} (9.4–11.9%) were found and estimated daily doses deviated by less than 8.0% from observed ones. These results confirm that our UV reconstruction technique performs well in regions with different climate conditions without further adaptations. Furthermore, the good agreement of our parameterization with the results of a modeling study further demonstrates that our method can be generalized to the different environmental conditions found in Switzerland and most likely in central Europe.

---

[1]Federal Office of Meteorology and Climatology MeteoSwiss, Payerne, Switzerland
[2]Institute for Atmospheric and Climate Science, ETH Zurich, Zurich, Switzerland

4.1   Introduction

Policy makers and the medical community require better and more complete information concerning the spatial distribution and temporal evolution of ultraviolet (UV) radiation, because of its important effects on the atmospheric chemistry (e.g., Brönnimann et al., 2001), various ecosystems and human beings (van der Leun et al., 1998). Such effects include the link between excessive UV exposure and the development of skin cancer (Diffey, 2004), and also UV impacts on the eyes and negative impacts on the immune system (de Gruijl et al., 2003). In many European countries, time-series of measured UV radiation are spatially sparse and temporally short and do not allow conclusions regarding such questions. For answering this data availability problem one can apply radiative transfer models and reconstruct UV irradiances for time periods when no UV observations are available. In the ongoing COST action 726, different reconstruction methods were assessed for studying the UV radiation over Europe during the last 50 years. These techniques extend existing time-series into the past and allow analyzing the UV temporal evolution and therewith the underlying processes leading to these changes. Furthermore, these techniques should be applicable at many locations to get a better insight in the spatial distribution of UV. Radiative transfer models (RTMs) explain well the variability and dependencies of UV radiation for clear-sky conditions. In many studies, good correspondence between measured and observed UV radiation has been found (e.g., Koepke et al., 2006; Mayer et al., 1997). However the treatment of clouds with such models is more difficult. Most cloudy situations do not consist of homogeneous cloud layers, and the resulting three dimensional problems cannot be adequately treated with the usual one-dimensional radiative transfer modeling.

The effects of clouds on UV radiation have been studied in the past using different variables related to cloud coverage. In several studies the total cloud coverage, cloud types and altitudes are used to estimate the impact of different cloud situations on atmospheric radiation (e.g., Blumthaler et al., 1994; Josefsson and Landelius, 2000). Josefsson and Landelius (2000), Lindfors et al. (2003) and Lindfors and Vuilleumier (2005) investigated the cloud effects using the relationship between observed sunshine duration and UV radiation. However, such explanatory variables either do not carry information about the screening of the sun by clouds or describe the cloud situation only as a binary flag. Total solar irradiance (SW) includes superior information on atmospheric turbidity and cloud coverage. Foyo-Moreno et al. (1999) investigated hourly ratios between UV and SW in Spain and found a contribution of UV to SW radiation of around 4%. The seasonal variability of this ratio and differing results found by other authors at different locations (e.g., Al-Aruri, 1990; Feister and Grasnick, 1992; Martinez-Lozano et al., 1994) do not allow generalizing this approach. On the other hand, Frederick et al. (1993) investigated the relationship between SW- and UV-transmission, and found a strong positive correlation (R^2=0.968). Thus, studying the cloud attenuation by evaluating the ratio between all-sky and estimated cloud-free radiation for the same situation (also called cloud modification factor - CMF) is more adequate than analyzing absolute radiation values. This approach was employed in several successive studies (e.g., Bodeker and McKenzie, 1996; Bordewijk et al., 1995; den Outer et al., 2000, 2005; Krzyścin et al., 2003; Schwander et al., 2002 or Trepte and Winkler, 2004).

These studies mainly differ in using varying time resolutions, different parameterization of the relationships between CMFs in the UV and SW, and how input information such as clear-sky radiation, albedo and ozone are inferred. The potential of describing the UV short-term variability due to clouds by using semi-empirical relationships between CMFs in the UV and SW was demonstrated in a recent study within COST action 726, where an inter-comparison of 16 reconstruction models showed the superiority of such methods (Koepke et al., 2006). However, most of these models were focused on specific sites for which the CMF_{UV} vs. CMF_{SW} relationships were derived, and the potential for further generalization should be investigated. Particularly, it should be determined whether such relationships are influenced by the local environment and cloud regimes, etc., which we explore for different Swiss locations in this study.

Such generalized methods allow not only reconstructing past UV time-series at locations with already existing observations, but also estimating UV radiation at locations where it has never been measured, but the necessary input data is available. Our aim is to derive semi-empirical relationships between CMF_{SW} and CMF_{UV} that can be applied to data from the dense Swiss meteorological network measuring SW since the early 1980s. Its stations are distributed over a complex topography and are located in regions with different climate conditions. We assess the dependencies of the generalized semi-empirical relationship on environmental variables, and propose a final parameterization using a time resolution of 10 minutes (10'). This high temporal resolution enables capturing the short-time variability in atmospheric radiation due to clouds. Our parameterization is also compared to relationships derived from previous studies, giving a better insight into the processes of cloud effects on SW and UV radiation.

In the next section, the data sources and their uncertainties are presented. Our method is explained in Section 4.3 and the results, including the validation of the derived relationships are shown in Section 4.4. These results are discussed in Section 4.5, together with a comparison against previous studies.

4.2 Data

This study is based on UV and SW radiation data measured at four sites in Switzerland (Figure 4.1, Table 4.1). The station at Payerne is situated in the Swiss lowlands, while Davos is set in an alpine valley in the eastern part of Switzerland. The high alpine site Jungfraujoch is located at 3580 m MSL, and the fourth station, Locarno-Monti, represents the climate conditions in the lowlands, south of the alpine ridge.

SW data is measured by the Swiss standard automated meteorological network (Swiss-MetNet, previously ANETZ), while SW and UV data is observed with enhanced time resolution by the Swiss Alpine Climate Radiation Monitoring network (SACRaM). Both networks are operated by the Federal Office of Meteorology and Climatology, MeteoSwiss. The SACRaM network is specialized in atmospheric radiation measurements of high accuracy and stability, and merges two previously separated networks, the Swiss Atmospheric Radiation Monitoring network (CHARM) and the Alpine Surface Radiation Budget network (ASRB). Both, the SwissMetNet and SACRaM network include the previously-mentioned four stations. In addition, information on the snow cover was necessary for

estimating the ground surface reflectance (albedo). Snow cover data are measured by two institutions in Switzerland: MeteoSwiss and the Swiss Federal Institute for Snow and Avalanche Research (SLF). Snow data from both institutions are used in this study.

We concentrate our analysis on time periods listed in Table 4.1, considering only data for solar zenith angles smaller than 72°. This ensures avoiding radiation data with larger relative uncertainties due to high solar zenith angles, while still selecting a large enough data set even during winter season. The modeled clear-sky UV and SW radiation, used as normalization quantity for the CMF calculation is estimated using observed total ozone and estimated regional surface albedo derived from observed snow depth. The CMF_{SW} is derived from SW 10'-averaged data provided by the SwissMetNet (previously ANETZ) network. This data is available at many sites in Switzerland since the early 1980s. Performing the analysis at stations located in regions with different climate conditions and excluding more detailed atmospheric data (i.e. profiles from balloon soundings or observed aerosol optical depth) allows estimating the method's uncertainties, which result from using such a limited data set available for the reconstruction of UV radiation over almost three decades.
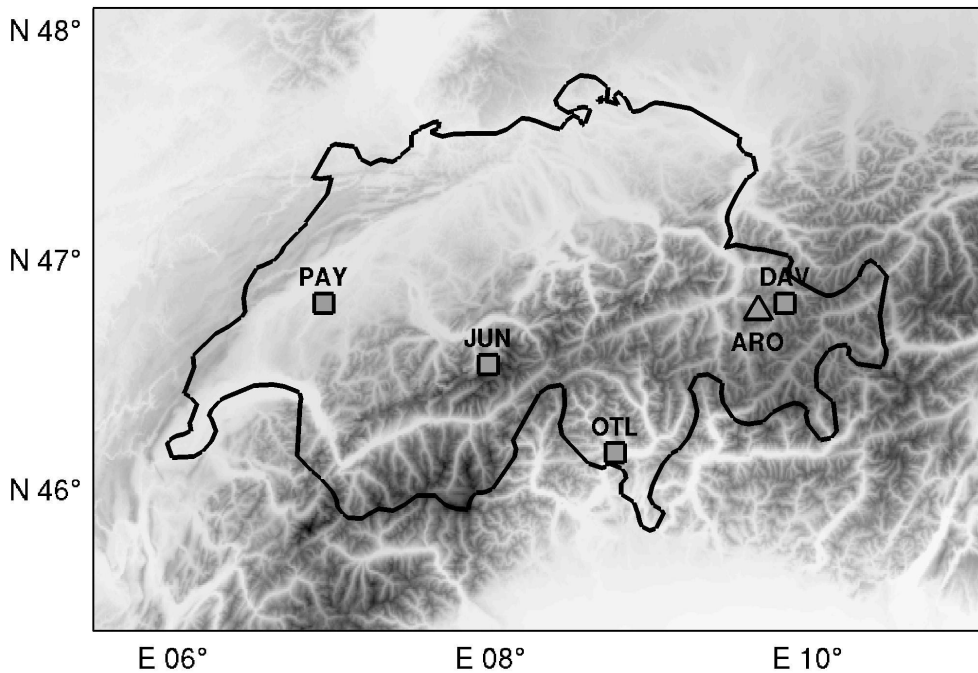

FIG. 4.1: Map of Switzerland showing the four stations (□) of the SACRaM network measuring UV radiation and Arosa (△) from where the ozone data was obtained. PAY: Payerne, JUN: Jungfraujoch, OTL: Locarno-Monti, DAV: Davos, and ARO: Arosa.

Table 4.1: Stations of the Swiss Alpine Climate Radiation Monitoring network (SACRaM) included in the analysis. Data of the "learning" period are used to derive the relationship. Observations of the "validation" period are used for testing. The geographic position of the stations is described by the latitude (lat), longitude (lon), and the altitude (alt) above mean sea level (MSL).

	lat / lon	alt	"learning"	"validation"
Payerne	46.8°N/6.9°E	491	05.04.2003 - 19.04.2007	20.04.2007 - 30.07.2008
Locarno	46.2°N/8.8°E	366	13.03.2005 - 25.04.2006	26.04.2007 - 31.03.2008
Davos	46.8°N/9.8°E	1590	01.10.2003 - 19.04.2007	20.04.2007 - 30.07.2008
Jungfraujoch	46.6°N/8.0°E	3582	08.08.2003 - 14.08.2006	02.11.2007 - 30.07.2008

4.2.a Broadband UV

In Switzerland, erythemal UV radiation is measured by broadband SolarLight SL 501 radiometers (biometers). The operational measurements started in the mid to end 1990s. All instruments are ventilated and temperature-stabilized at 25°C. Biometers are calibrated, using an ozone and solar zenith angle dependent method similar to the one recommended by Webb et al. (2007). For this study, the erythemal UV data has been averaged over 10' to make it comparable to the SW radiation observed by SwissMetNet. The stability of the biometers is continuously monitored, including regular calibration checks of each instrument at the aerological station at Payerne. The reference biometers used for the calibration checks took part in the COST 726 calibration and inter-comparison campaign for erythemal radiometers, which was organized at the World Radiation Center, PMOD/WRC Davos, in summer 2006. During this campaign the radiometers were fully characterized and their uncertainties assessed. The total uncertainties of MeteoSwiss references were estimated to be on the order of 7.5-9.5% for solar zenith angles of less than 50° and clear-sky conditions. For all-sky conditions, the uncertainties increase by 0.5% due to a stronger random variability.

4.2.b Total solar radiation (SW)

SW radiation is currently measured at around 70 stations in Switzerland by the presently installed SwissMetNet automatic meteorological network (previously ANETZ) at a time resolution of 10'. Pyranometers of both CM5 and CM21 type by Kipp&Zonen were used for SW measurements over the time period analyzed in this study. The CM21 measures global irradiance between 305-2800 nm and fulfills the WMO requirements for a "secondary standard" instrument, corresponding to maximum expected errors on the order of 3% for hourly averages, and 2% for daily averages (Kipp&Zonen, 2004). The uncertainty of the 10'-data has been further assessed at Payerne and Jungfraujoch, which are also part of the high-accuracy SACRaM network. For this purpose the data of SwissMetNet were compared against SACRaM-data. At the lowland station Payerne, an annual cycle in the root mean square differences (RMS) between 20 and 70 W m^{-2} (winter/summer)

was found (R^2=0.96, n=570'511). The quality for ANETZ/SwissMetNet observations improved significantly since beginning 2007 due to instrument changes. At the high alpine site Jungfraujoch larger deviations were found. The annual cycle in the RMS varies between 30 W m^{-2} in winter and 70 to 100 W m^{-2} during summer (R^2=0.949, n=351'734). These higher values are caused by a combination of calibration problems and the harsh meteorological conditions found at this exposed mountainous site.

The change from ANETZ to SwissMetNet resulted in a change in the absolute radiation level when compared to the SACRaM network. Since at all four stations SACRaM and SwissMetNet/ANETZ instrumentation was operated in parallel over the analyzed period, the SwissMetNet data could be corrected to be compatible with the ANETZ data. The more accurate SwissMetNet data was adjusted instead of correcting the ANETZ data because we want our method to be set up so that it allows using the older ANETZ data for inferring CMF$_{UV}$ in the past. The correction factors used for modifying the SwissMetNet data ranged from 0.94 to 0.98, depending on the station (cf. Appendix B).

4.2.c   Ozone

The historic total ozone time-series from the Light Climatic Observatory at Arosa, Switzerland are the longest worldwide. The station (46.77° N, 9.67° E, 1840 m MSL) is located in the Swiss Alps close to Davos (Figure 4.1). The total ozone observations started in 1926 with Dobson spectrophotometer measurements (cf. Staehelin et al., 1998b). The instrumentation at this site was supplemented with Brewer spectrophotometers in 1988. The total ozone data used in this study was derived from Brewer measurements at Arosa. An altitude correction is performed to account for the vertical tropospheric ozone column between the altitudes of the different sites and Arosa. This correction is based on a yearly cycle climatology derived from ozone concentration profiles obtained by balloon soundings at the aerological station of Payerne. The three Brewer instruments (Serial No. #40, #72, and #156) at Arosa undergo yearly calibrations through the traveling standard Brewer #17 from the International Ozone Services Inc. This instrument is traceable to the reference triad at Toronto, Canada (Fioletov et al., 2005). The calibrations between 2003 and 2007 revealed no major changes or drifts in the stability of the Brewers at Arosa. All instruments were certified to be in good conditions over this period. However, for some years, the calibration constants needed small adjustments of at most 1%.

4.2.d   Snow measurements

In this study, snow observations from MeteoSwiss and SLF are used to estimate the effective surface albedo at the different sites. Snow depth and new snow amount are measured by meteorological observers on a daily basis. The regional snow distribution was assessed using the data of 125 stations in the Swiss lowlands and the Alps, 45 of which are operated by MeteoSwiss and 80 by the SLF. These manual observations are of higher quality than automated stations, measuring snow by ultrasound instrumentation. However, the data of MeteoSwiss was checked for unusually large day-to-day differences and the data of the SLF passed a further internal quality control chain.

4.3   Method

We want to express CMF_{UV} as a function of CMF_{SW}. Both CMFs are ratios of all-sky observations to theoretical clear-sky predictions in their respective wavelength range:

$$\text{CMF}_{\text{UV}} = \frac{\text{UV}_{\text{all-sky}}}{\text{UV}_{\text{clear-sky}}} \qquad \text{and} \qquad \text{CMF}_{\text{SW}} = \frac{\text{SW}_{\text{all-sky}}}{\text{SW}_{\text{clear-sky}}} \tag{4.1}$$

where $\text{UV}_{\text{all-sky}}$ includes UV observations for both clear-sky and cloudy situations, while $\text{UV}_{\text{clear-sky}}$ are model simulation estimates of the UV irradiance for the same conditions but without clouds. SW quantities are defined similarly.

4.3.a   Effective albedo

The surface reflectance is an important input parameter to the RTM used for estimating clear-sky values. To describe the surface reflectance effects on the downward irradiance, an effective albedo is estimated using the reflectivity of an enlarged area around the target location. This albedo is calculated using the daily regional snow distribution around the desired sites, following the method described by Walker et al. (2009). In their study, the elevation of the snowline was inferred daily from observed snow depth at 125 stations in the Swiss lowlands and the Alps. The combination of the snowline altitude with a digital elevation model allowed estimating the spatial snow cover in Switzerland back to 1980. This method was successfully validated using both cross-validation and comparison to satellite data.

Within a radius of 50 km, the snow covered portion of the surrounding area was calculated for each radiation observing station used in our study on a daily base. We applied a Gaussian distance weighting, giving more weight to pixels closer to the station. The effective albedo is linearly interpolated between a minimal and maximal albedo, corresponding to 0% and 100% snow coverage. Typical effective albedo values for completely snow-free and snow-covered conditions are on the order of 0.03–0.65 for UV and 0.2–0.6 for SW, respectively (cf. Eck et al., 1987; Kylling et al., 2000; Schmucki et al., 2001; Weihs et al., 2001). In this study, station-specific effective albedo ranges are used, estimated by comparing observed UV and SW radiation with estimates by a radiative transfer model. These adjusted values (Table 4.2) are minimizing the dependency of the model-to-observation ratio on the regional snow coverage for clear-sky events. The lower and upper limits of the estimated albedo are larger for stations in alpine regions. This can be related to the snow being generally cleaner and more fine-grained at higher altitudes and the snow covered surfaces being more homogeneous than at lower altitudes (cf. Weihs et al., 2001). Nonetheless, the upper albedo limit found at Locarno-Monti is identical to the lower limit, which is unrealistic. This is probably due to albedo, compensating for a seasonal cycle (e.g. for aerosols) that is not enough captured by the limited number of model input parameters that vary according to observations. However, snow effects at this station are relatively rare because the median number of days with snow per year (≥ 0.05 m) is around four since 1990.

TABLE 4.2: Limits of the effective albedo for snow free (min) and fully snow covered (max) area around a location (radius < 50 km).

	Regime	UV min	UV max	SW min	SW max
Payerne	lowlands	0.03	0.30	0.2	0.6
Locarno-Monti	southern alpine foothills	0.03	0.03	0.2	0.8
Davos	alpine valley	0.10	0.60	0.3	0.8
Jungfraujoch	high alpine	0.60	0.80	0.2	0.9
Standard range		0.03	0.65	0.2	0.6

4.3.b   Clear-sky model

Erythemal UV and SW radiation for clear-sky conditions were modeled using the *uvspec* program, which is part of libRadtran, a library for radiative transfer calculations (Mayer and Kylling, 2005). This model was validated in several model to observation comparisons (e.g., Mayer et al., 1997). Koepke et al. (1998, 2006), however, found in inter-comparisons that all models give similarly good results from a mathematical point of view, and the model uncertainty is mainly due to the uncertainty of the input parameters.

Total ozone, the solar zenith angle (SZA), and the daily effective albedo are the variable parameters used as input to the radiative transfer model (RTM). The effective albedo is derived as described in Section 4.3.a. The vertical structure of the atmosphere in the RTM is defined by standard atmospheres for mid-latitudes with a summer and winter configuration (Anderson et al., 1986). The aerosol composition and properties are derived from Shettle (1989) with rural type aerosols in the boundary layer and background aerosols above 2 km. Again, a spring-summer and fall-winter profile is available. All calculations are performed using the pseudospherical disort radiative transfer equation solver (Dahlback and Stamnes, 1991). In case of erythemal UV simulation, the spectral model output is weighted by the CIE erythemal action spectrum (McKinlay and Diffey, 1987). When modeling the integrated SW radiation, the correlated-k scheme after Kato et al. (1999) was used.

We tested the performance of the model in reproducing clear-sky radiation in the UV and SW range at the four study sites. Clear-sky periods are selected using the APCADA cloud detection algorithm, which calculates the partial cloud amount based on longwave radiation, temperature, and relative humidity (Duerr and Philipona, 2004). In addition to the zero octas of cloud estimation by APCADA, we require that the variability in the observed diffuse SW radiation is small, since this parameter is especially strongly influenced by clouds. Therefore, the difference between adjacent diffuse SW radiation measurements minus its 30'-moving average is tested for its variability. The standard deviation over bins of 30' is limited to a maximum of 0.25 W m^{-2} for assigning clear-sky conditions.

The root mean square (RMS) differences between modeled and observed clear-sky UV and SW radiation are given in Table 4.3. The modeling performance is generally better for SW than for UV radiation. For small SZAs ($< 40°$), the relative differences range within 3.6-5.0% (6.4-8.9 mW m^{-2}) for UV and 1.7–2.9% (14.5–24.3 W m^{-2}) for SW radiation. The relative modeling uncertainties increase at all stations for larger SZAs ($> 60°$) with

differences ranging within 5.3–8.3% (1.6–3.9 mW m^{-2}) for UV and 3.4–4.8% (14.3–20.6 W m^{-2}) for SW radiation. Despite the use of seasonal aerosol climatologies and atmospheric profiles instead of observations, the differences between modeled and observed irradiances are small. This confirms that libRadtran is able to reproduce satisfactorily clear-sky solar irradiance within the desired wavelength ranges. When for all stations the standard albedo limits are used (cf. Table 4.2), instead of the individually estimated albedo ranges (cf. Section 4.3.a), the relative RMS errors increase by less than 3.0% and 1.3% for UV and SW, respectively. The only exception represents the high-alpine station Jungfraujoch, where the optimized albedo range for UV radiation improves the RMS by 7.5%. This improvement due to the albedo optimization is mostly caused by the very special snow conditions at this high-alpine location, including adjacent glacier fields and the station being situated between two close mountain peaks rising more than 500 m. A compensation effect of a missing aerosol characterization can mostly be excluded, since optimized albedo differ only slightly when observed aerosol optical depth is included.

TABLE 4.3: Root mean square differences [%] between modeled and observed UV and SW radiation for clear-sky conditions. The data is separated into three classes with different solar zenith angles (SZA). n_{tot} represents the number of observations per station, n the size of the subset analyzed per SZA class. For Davos and SZAs between 22 and 40° not enough data was available for statistical analysis.

| | n_{tot} | 22-40° | | | 40-60° | | | 60-72° | | |
		UV	SW	n	UV	SW	n	UV	SW	n
Payerne	893	4.2%	1.7%	58	4.3%	2.9%	345	5.3%	3.8%	490
Davos	356	-	-	9	4.1%	2.6%	125	5.3%	3.4%	222
Locarno	1369	5.0%	2.9%	153	6.9%	3.7%	568	7.8%	4.8%	648
Jungfraujoch	1931	3.6%	1.6%	328	4.4%	2.6%	835	8.3%	4.7%	768

4.3.c Relationship between CMF_{UV} and CMF_{SW}

The CMF_{UV} to CMF_{SW} relationships are derived from the analysis of scatterplots (e.g. Figure 4.2). Such graphs reveal three different clusters that can be distinguished using objective criteria. An ovoid-shaped data cluster at high CMFs (around $CMF_{UV} = CMF_{SW} = 1$, shown in green on Figure 4.2) is separated using a combination of two "clear-sky" criteria: (1) 100% sun-duration over 10' and (2) restricting the relative standard deviation over 70 minutes (70') of the differences between the SW radiation and its 70'-window moving average to less than 10%. This separation of clear-sky data is important because this cluster has a high data density, and wields a disproportionate influence on the parameterization of the rest of the data. Two regimes can be distinguished when analyzing the remaining data representing cloudy conditions. For large cloud coverage (low CMFs, in red on Figure 4.2) the CMF_{UV} increase over-proportionally with CMF_{SW} resulting in a CMF_{UV} vs. CMF_{SW} slope above one. Conversely, at higher CMFs with smaller cloud attenuation (in blue on Figure 4.2), the slope is smaller than one. Hence, we assume a relationship divided into two subsets and characterize them separately by two linear

regressions, hereinafter refered to as lower (red) and upper (blue) regression. The break-point between the two regressions is determined with an iterative procedure driven by the requirement that the two regressions intersect at the same value at this breakpoint ($CMF_{SW,break}$). The separate analysis of low and high CMF clusters allows a differentiated treatment according to the individual data characteristics of the clusters. The low-CMF cluster (red) has a fanlike structure, which results in an increasing scatter of the residuals with increasing CMF_{SW}. When using a linear fit in log-transformed CMF space (log-log), the residuals with respect to the fit remain nearly constant over the range of the lower regression. The subset at high CMFs does not exhibit such a varying structure of the residuals to the fit (providing the clear-sky cluster is excluded), and can be satisfactorily treated with a linear regression in normal CMF space. Statistical analysis of the residuals confirmed our approach of choosing two linear regressions and to perform a logarithmic transformation for the low CMF data (strong attenuation).
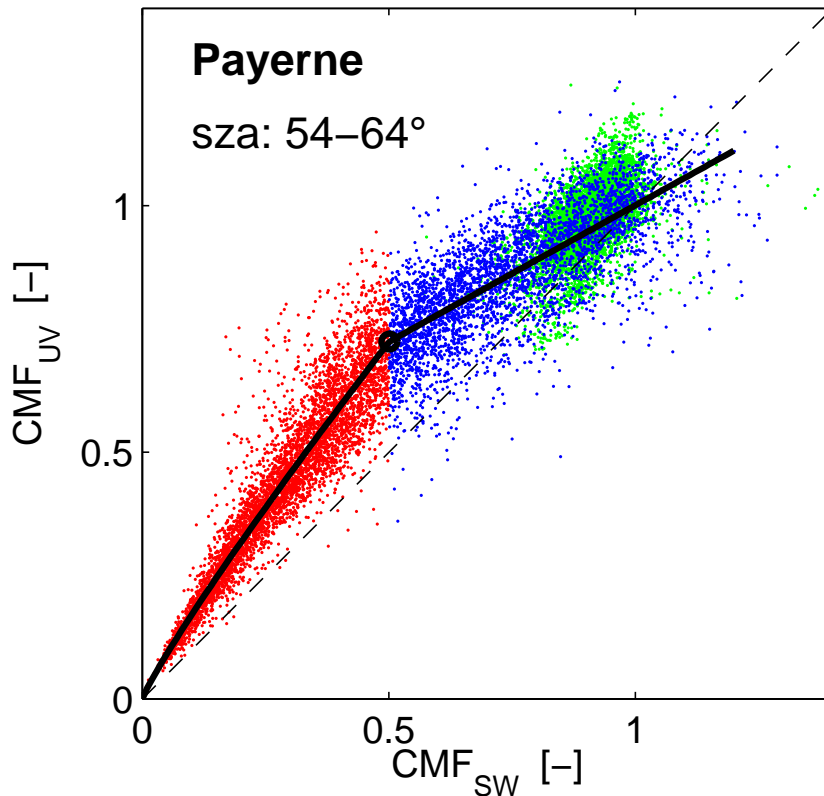

FIG. 4.2: The relationship between dimensionless CMF_{UV} and CMF_{SW} at Payerne for data with SZAs between 54 and 64°. **o**: the separation between lower (red) and upper (blue) regression ($CMF_{SW,break}$).

We define the relationship between CMF_{UV} and CMF_{SW} as the combination of the lower and upper regression. Because the lower regression fit is obtained in log-log space, the resulting relationship for strong cloud attenuation is of the form $CMF_{UV} = b \cdot CMF_{SW}{}^{a}$. Nevertheless, this parameterization is almost linear also for untransformed CMF data, since the curvature parameter (a) is generally close to one. For the upper regression fit, we deduce a truly linear relationship.

The relationships between CMF_{SW} and CMF_{UV} are estimated using a joined dataset of all four stations. In order to give the same statistical weight to all four stations, the combined dataset consists of subsets of each station including the same amount of data. This amount was defined by the station with the smallest dataset (i.e. Locarno-Monti, n = 7372). Subsets of the same size are extracted randomly for the other three stations. The shape of the fitted relationships is robust and its sensitivity on the chosen subsets of data is smaller than ± 0.020 CMF_{UV}. This was demonstrated by a non-parametric bootstrapping method (n = 10^4) and the calculation of the envelope around all regressions, resulting from these random samples.

The relationship between CMF_{UV} and CMF_{SW} is estimated for four different solar zenith angle (SZA) classes (Table 4.4) since its shape strongly depends on the sun elevation. The data separation into more than four SZA-classes was tested, but did not improve the variability of the residuals from the fitted data for big SZAs where the scatter is largest. Further details regarding the dependencies of the relationships on environmental factors are given in the next Section (4.4.a). These four relationships, as shown in Figure 4.3, are used to infer all-sky erythemal UV from observed SW radiation. We verified that the most adequate method to infer UV radiation for the previously separated "clear-sky" cluster is the application of the parameters of the upper regression. It was this method, which produced the best results in validations. In addition, it is reasonable to use the regression derived for weak cloud attenuation also for the clear-sky situations since there is a smooth transition from light cloud coverage to clear-sky conditions. The formulation of the full parameterization:

$$CMF_{UV} = \begin{cases} b_1\left(\theta\right) \cdot CMF_{SW}^{a_1(\theta)} \\ b_2\left(\theta\right) + a_2\left(\theta\right) \cdot CMF_{SW} \end{cases} \quad \text{for} \quad CMF_{SW} = \begin{cases} < CMF_{SW,break}\left(\theta\right) \\ \geq CMF_{SW,break}\left(\theta\right) \end{cases} \quad (4.2)$$

where $a_{1,2}$, $b_{1,2}$, and $CMF_{SW,break}$ are depending on the solar zenith angle (θ). The parameter values and statistical information about the linear regressions for the four SZA classes are presented in Table 4.5.

TABLE 4.4: Limits of the classes used for the analysis of the dependencies of the relationship on environmental variables (total ozone, surface reflectance, and solar zenith angle).

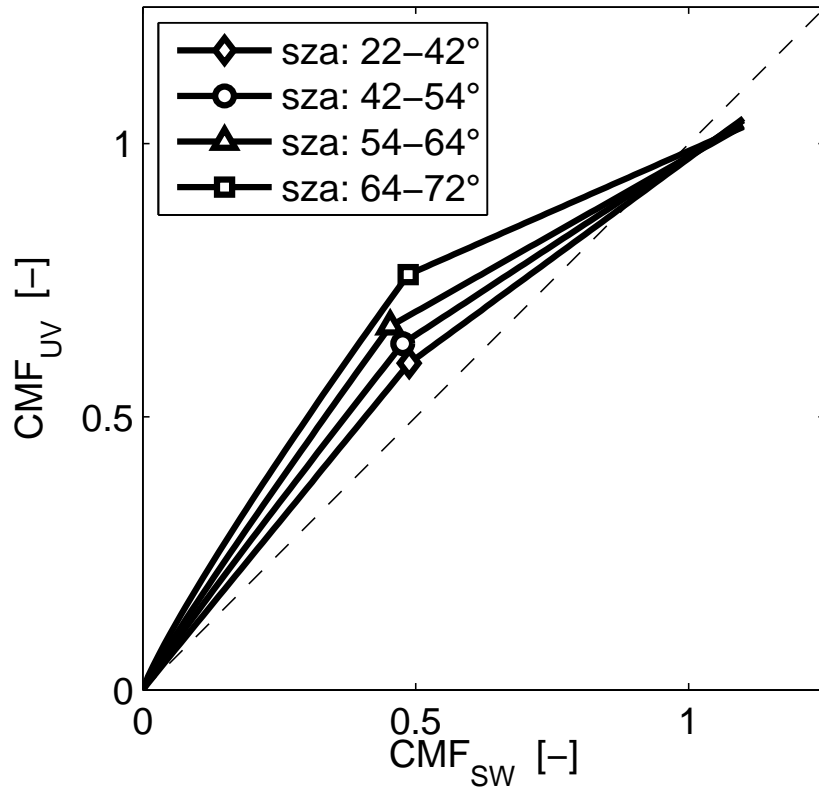| Environmental factors:					
Total ozone	[DU]	< 300	300 - 350	> 350	
Effective albedo	[-]	0 - 0.1	0.1 - 1.0		
Solar zenith angle	[°]	22 - 42	42 - 54	54 - 64	64 - 72

FIG. 4.3: Relationship between CMF_{UV} and CMF_{SW} for four different SZA-classes. The markers ($\square, \triangle, \bigcirc, \diamondsuit$) represent the position of the $CMF_{SW,break}$, separating the upper and lower regression.

4.4   Results

4.4.a   *Dependencies of cloud effects on environmental factors*

The chosen parameterization (Equation (4.2)) is based on an assessment of the dependencies of cloud effects on various environmental factors. In this section, the effect of variable surface reflectance, total ozone and solar zenith angle (SZA) on the relationships between CMF_{SW} and CMF_{UV} is presented. The main parameters describing the shape of the relationships are the slopes of the lower and upper regression and the location of the breakpoint ($CMF_{SW,break}$). Since the power function of the lower regression is almost linear (curvature parameter (a_1) close to one), the slope is approximated by the first derivative at a CMF_{SW} of 0.2. For the analysis of the dependencies, the data of each station is separated into subsets for all possible combinations of albedo-, ozone-, and SZA-classes shown in Table 4.4. Fitting upper and lower regressions to the CMF data for all class-combinations allowed assessing the impact of these local climate conditions on the shape of the relationships.

Neither the ozone, nor the albedo exhibited a clear influence on the regression parameters. The largest effect on the slopes of the relationships is caused by varying SZA. In Figure 4.4, the slopes of the upper and lower regression for all class-combinations at the four stations are shown. The inter-station effect on the slope magnitudes is small and on

TABLE 4.5: Regression parameters (a_i, b_i) of the relationships CMF_{UV} vs. CMF_{SW} for four different SZA-classes including the location of $CMF_{SW,break}$, where the lower and upper regressions are separated. Further information: coefficients of determination (R^2), root mean square errors between the observed and fitted CMFs (RMS) and amount of observations (n).

	22 - 42°	42 - 54°	54 - 64°	64 - 72°
lower regression:				
a_1	0.997 [±0.007]	0.956 [±0.008]	0.941 [±0.009]	0.884 [±0.011]
b_1	1.223 [±0.013]	1.289 [±0.015]	1.401 [±0.018]	1.439 [±0.022]
R^2	0.955	0.926	0.907	0.827
RMS [-]	0.046	0.057	0.070	0.100
RMS [%]	13.6	14.4	15.9	19.2
n	3142	3164	3562	4100
$CMF_{SW,break}$	0.49	0.48	0.45	0.49
upper regression:				
a_2	0.732 [±0.012]	0.655 [±0.012]	0.568 [±0.013]	0.441 [±0.014]
b_2	0.241 [±0.010]	0.322 [±0.009]	0.408 [±0.010]	0.546 [±0.011]
R^2	0.803	0.778	0.651	0.449
RMS [-]	0.067	0.066	0.080	0.092
RMS [%]	8.7	8.7	11.1	12.5
n	3933	3560	3895	4132

the same order of magnitude as the scatter. Furthermore, the graph illustrates a distinct change in shape of the relationship with increasing SZA: for larger SZAs the lower regression becomes steeper (lower panel), while the slope of the upper regression decreases at the same time. This behavior leads to a stronger bend of the relationships for larger SZAs. The horizontal position of the $CMF_{SW,break}$ is robust and ranges typically between 0.4 and 0.55 and again, no clear inter-station differences are found.

4.4.b   UV modeling for all-sky conditions

The parameterization (Equation (4.2)) is used to estimate erythemal UV radiation on a 10'-time interval at the four SACRaM stations during the validation time periods defined in Table 4.1. The lengths of these validation periods depend on the station and do not overlap with the data, previously used for deriving the relationships. Erythemal UV for all-sky conditions ($UV_{all-sky}$) is calculated using:
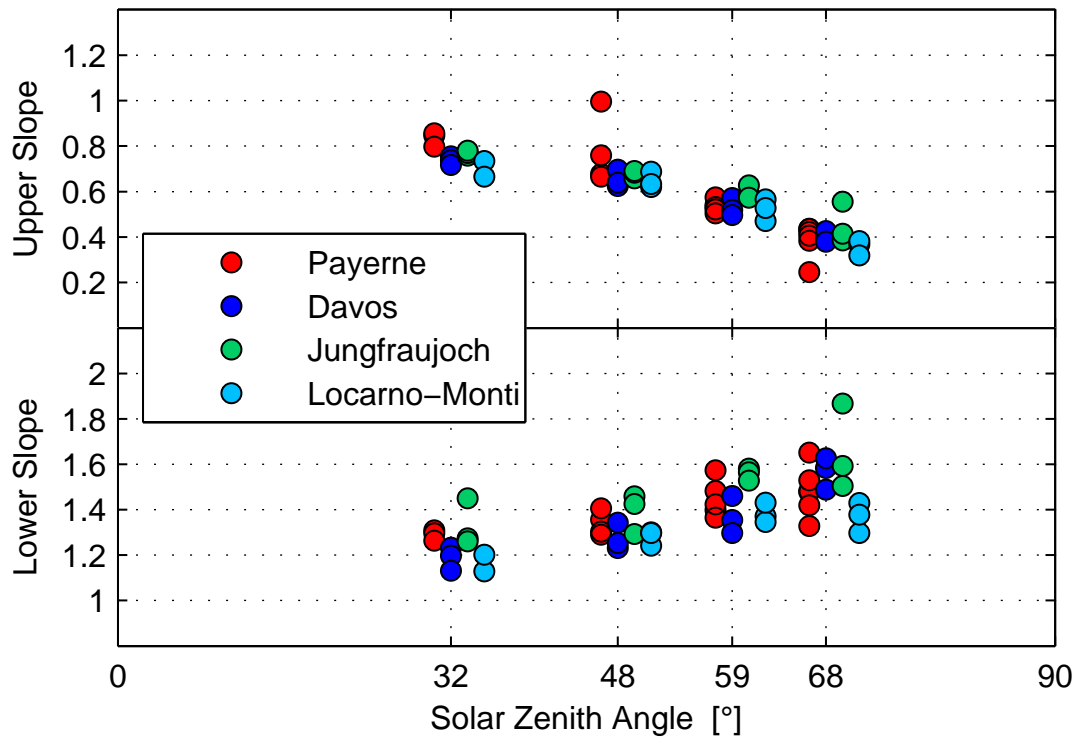
FIG. 4.4: Slopes of the upper and lower regression vs. the SZA. Slope of the lower regression refers to the first derivation of the fitted power function at CMF_{SW} of 0.2. Each data point represents one combination of station, SZA, albedo, and ozone (cf. Table 4.4). Combinations are only analyzed in case of more than 20 data points. The data of the different stations are separated by small offsets around the four SZA class centers for better readability.

$$UV_{\text{all-sky}} = UV_{\text{clear-sky}} \cdot CMF_{UV} \tag{4.3}$$

where $UV_{\text{clear-sky}}$ is the clear-sky UV radiation modeled by the RTM and CMF_{UV} the cloud modification factor derived from the parameterization (Equation (4.2)) described in the previous section.

In Figure 4.5, the diurnal cycles of observed and estimated UV radiation for a cloudy day at Payerne in June 2007 are shown. During this day, observed cloud coverage varied between 6 and 8 octas leading to strong diurnal variability of the solar radiation. The observed short-term variability due to clouds is well reproduced by the estimated UV radiation. This example illustrates the capability of the method to respond adequately to rapidly changing cloudiness when working with high time resolution data instead of using hourly averaged or daily aggregated data.

The correspondence between estimated and observed UV radiation over the whole validation period is shown in Figure 4.6. The linear regressions of estimated vs. observed UV yield slopes between 0.96 and 1.03 and small absolute intercepts exceeding 0.28 mW m^{-2} only at Payerne (0.88 mW m^{-2}). The coefficients of determination (R^2) exceed 0.987 at all four stations. The root mean square (RMS) differences between estimated and ob-
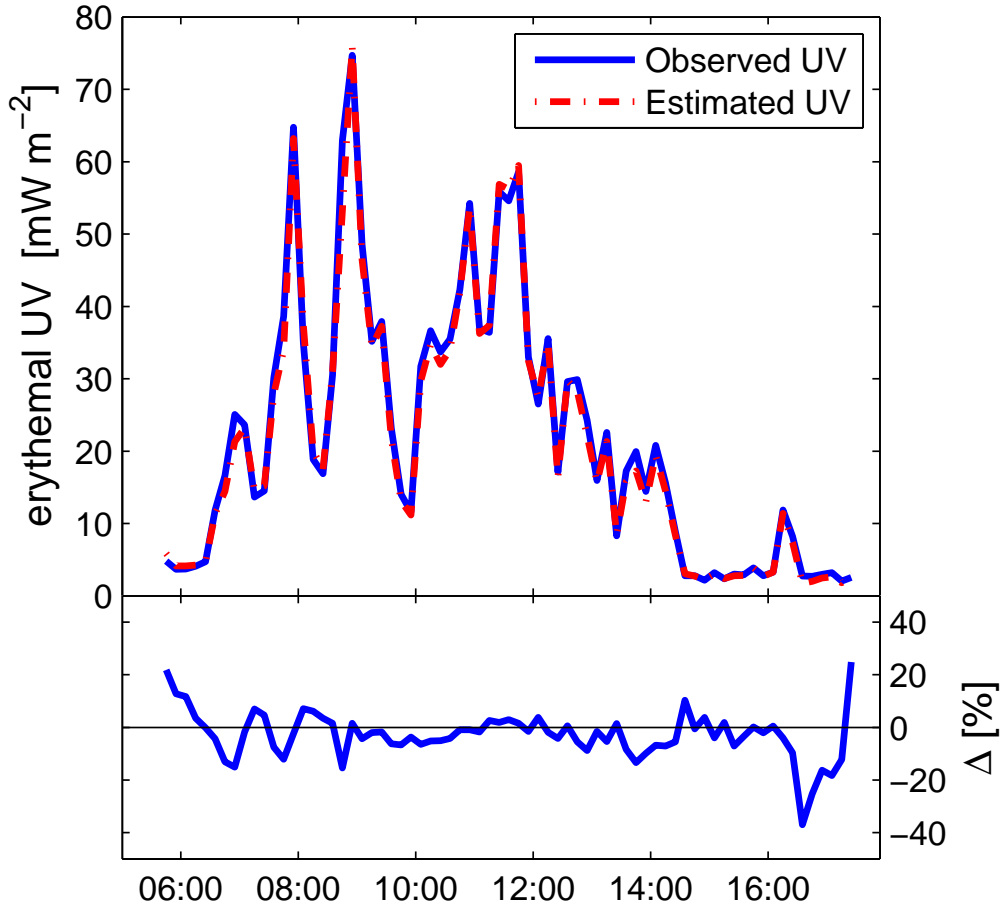
FIG. 4.5: Diurnal cycle of observed and estimated all-sky UV radiation at Payerne (25 June 2007, Time UTC). Lower panel: differences between estimated and observed UV in percent.

served UV range from 9.4–11.9% (4.3–6.9 mW m^{-2}). The Willmott's d is a descriptive index of agreement between a model (P) and observations (O), which is both a relative and bounded measure between zero and one (Willmott, 1982).

$$d = 1 - \frac{\sum_{i=1}^{n} (P_i - O_i)^2}{\sum_{i=1}^{n} (|P_i'| + |O_i'|)^2} \quad , \quad 0 \leq d \leq 1 \tag{4.4}$$

where $P_i' = P_i - \overline{O_i}$, and $O_i' = O_i - \overline{O_i}$. This skill factor gives more weight to modeling errors in cases where the model and/or the observation are close to the average observation $\overline{O_i}$. A Willmott's d of one indicates a perfect agreement between the model and the observations. The Willmott's d values in our validation reach at all four stations 0.997. The contribution of systematic errors in this comparison was investigated by separating
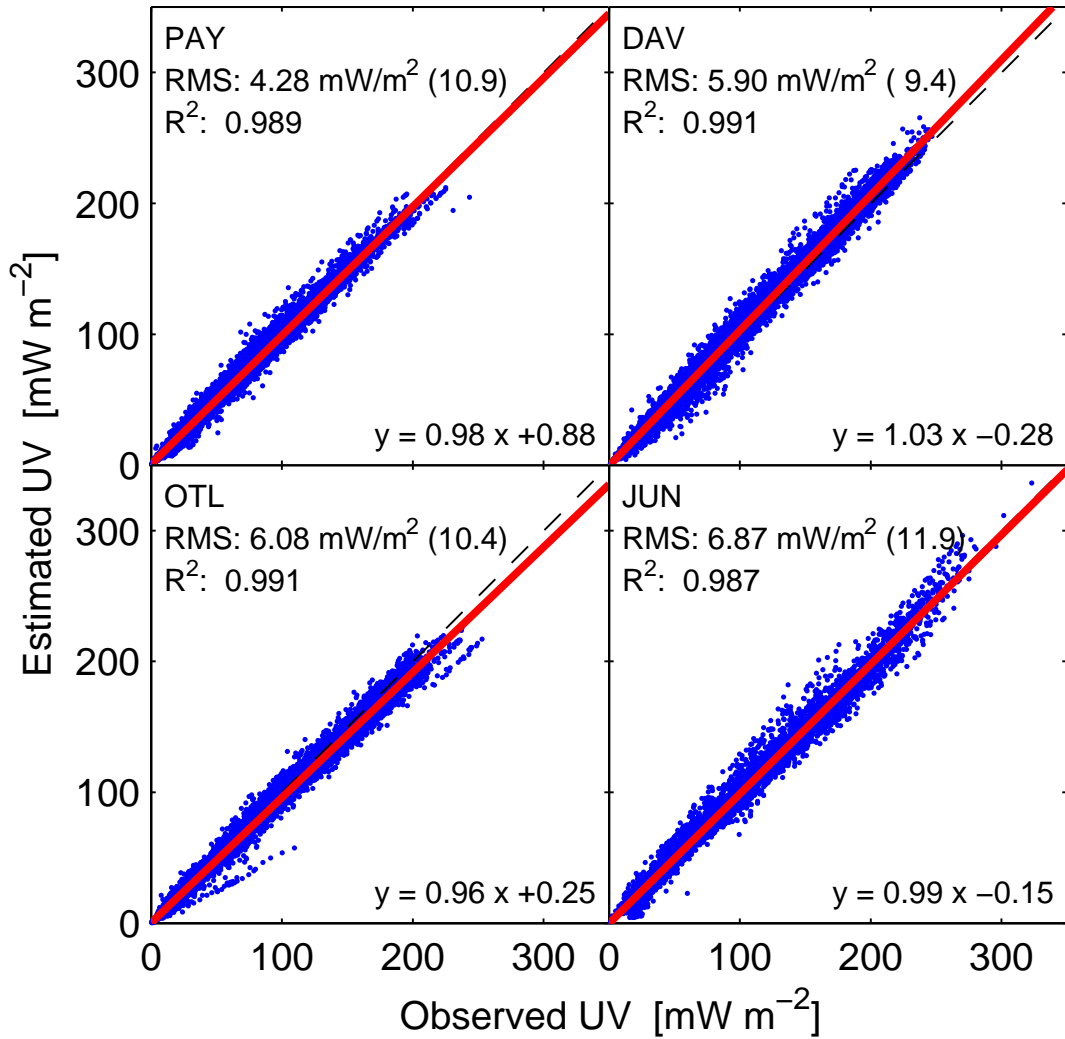
FIG. 4.6: Comparison of estimated vs. observed UV radiation at the four SACRaM-stations in Switzerland where UV is measured. PAY: Payerne, DAV: Davos, OTL: Locarno-Monti, and JUN: Jungfraujoch. The root mean square errors (RMS) are given in mW m^{-2} and in (%).

the non-systematic part from the total mean square error (MSE):

$$\text{systematic:} \quad \text{MSE}_\text{S} = \frac{1}{n} \sum_{i=1}^{n} \left(\hat{P}_i - O_i \right)^2$$

$$\text{unsystematic:} \quad \text{MSE}_\text{U} = \frac{1}{n} \sum_{i=1}^{n} \left(P_i - \hat{P}_i \right)^2 \tag{4.5}$$

where $\hat{P}_i = a + b \cdot O_i$ is the fitted model prediction
of a linear regression (Willmott, 1982).

At Payerne and Jungfraujoch the MSE is mostly caused by scatter with a systematic contribution of less than 2.6%. A larger systematic portion of total error of 22 and 33% was found at Davos and Locarno, respectively. This is in agreement with the tendency

of over- and underestimation indicated by larger deviations of the regression slopes from one in Figure 4.6 at these two stations.

The performance of the method was also investigated as a function of the solar zenith angle (SZA). For this purpose the correspondence between modeled and observed UV was analyzed for SZA-classes corresponding to the classification used to derive the relationships (Table 4.6). For small zenith angles ($< 42°$), the average RMS differences between estimated and observed UV range from 8.4 to 9.7% and increase, as expected, for larger SZAs. This is related to smaller absolute radiation levels and higher uncertainties of modeled and observed radiation that occur at large SZAs.

The estimated high time resolution data can be aggregated on longer time periods such as daily doses. The modeling performance for the daily doses is better than for 10'-data (Table 4.7). The linear regressions of estimated vs. observed daily doses lead at all four stations to slopes close to one (0.96-1.04) and to high R^2s exceeding 0.988. The absolute biases are small (< 80 J m^{-2}) and RMS differences between 5.4–8.0% were found. The weighted average RMS error over all stations amounts to 6.4%.

TABLE 4.6: Comparison of estimated vs. observed 10' UV radiation for all-sky conditions. The performance is shown separately for four different SZA-classes using root mean square errors (RMS in %), bias (mW m^{-2}) and the regression slope. On the last row, the weighted averages of the RMS are shown. The number of data per SZA-class and station range from 1678 to 5067.

	22-42°			42-54°		
	RMS	Bias	Slope	RMS	Bias	Slope
Payerne	9.7%	1.07	0.96	9.8%	-0.38	0.94
Davos	8.4%	4.27	1.03	8.5%	2.52	1.01
Locarno	9.2%	-4.83	0.94	8.8%	-2.64	0.94
Jungfraujoch	8.7%	-0.34	0.96	10.5%	-0.73	0.93
	9.0%			9.3%		

	54-64°			64-72°		
	RMS	Bias	Slope	RMS	Bias	Slope
Payerne	10.1%	-0.42	0.95	13.2%	-0.01	0.96
Davos	10.1%	1.15	1.00	10.7%	-0.11	0.97
Locarno	10.1%	-1.71	0.94	12.8%	-1.32	0.90
Jungfraujoch	10.2%	-1.15	0.93	15.5%	-1.40	0.97
	10.1%			12.8%		

TABLE 4.7: Comparison of estimated vs. observed daily doses using root mean square errors (RMS), bias and linear regression results (R^2, slope and intercept). The last row shows the weighted averages of the RMS and R^2 over all stations.

	RMS $[J\ m^{-2}]$		Bias $[J\ m^{-2}]$	R^2	Slope	Intercept $[J\ m^{-2}]$	n
Payerne	78.2	(6.0%)	0.8	0.990	0.99	15.8	353
Davos	122.3	(5.4%)	61.9	0.995	1.04	-29.1	355
Locarno	160.9	(8.0%)	-79.6	0.993	0.96	11.9	261
Jungfraujoch	156.6	(6.6%)	-23.1	0.988	1.00	-29.0	178
	122.8	(6.4%)		0.992			

4.4.c   Cloud effects: empiricism vs. model

We compare our parameterization with those developed in two other studies, one using an empirical method similar to ours (Bodeker and McKenzie, 1996; thereafter referred to as B96), and another primarily model-based approach (Lindfors et al., 2007; thereafter referred to as L07). A general overview of studies investigating cloud effects on UV is given by Calbó et al. (2005).

B96 derived relationships between CMF_{SW} and CMF_{UV} as function of the SZA at Lauder, New Zealand, using a high temporal resolution (10') and a one-year dataset. The UV cloud effect was estimated by power-functions of CMF_{SW}. In case studies extending over four days, the method tended to overestimate the daily doses by up to 16 and 21%, but was able to capture the diurnal variability in observed UV radiation. L07 chose another approach relying exclusively on calculations of a 1-dimensional radiative transfer model (RTM) for investigating CMF_{UV} vs. CMF_{SW}. This method generates a lookup table with modeled UV and SW radiation for clear-sky and cloudy conditions. The atmospheric radiation for cloudy conditions was simulated by introducing stratiform clouds with variable cloud optical depth into the RTM. Erythemal UV was estimated using this method at four different stations in northern Europe and RMS differences to observed daily doses between 5 and at most 22% were found, depending on the season and location.

We reproduce the methods of B96 and L07 for generating CMF_{UV} vs. CMF_{SW} relationships for each of the SZA-classes we used in our study (Figure 4.7). The CMF_{UV} inferred from the B96-relationships are generally smaller than those inferred from the method of L07 or ours. These differences are most pronounced within a CMF_{SW} range between 0.2 and 0.8 because the relationships of L07 and ours are not only steeper, but also more strongly bent. However, the B96 relations overestimate CMF_{UV} for CMF_{SW} larger than 0.8 and large SZAs compared to the other two methods (cf. lower right panel, Figure 4.7). For small SZAs, our relationships are very similar to those of L07, but some differences are found for larger SZAs (> 64°). These are more pronounced for CMF_{SW} between 0.4–0.5, where also the separation between the lower and upper regression is located in our method. This separation represents the change over from the steep to the flatter part of the relationship and is located at lower CMF_{SW} than the "flattening" of the L07-relations, occurring for CMF_{SW} above 0.7–0.8. On the other hand, the B96-relations present a maximum curvature at low CMF_{SW}, which is not optimal for reproducing the observed shape

of the CMF_{UV} vs. CMF_{SW} data in our study. Finally, the maximal absolute differences between our relationships and those of L07 are between 0.05 and 0.07 CMF_{UV} units for the SZA-classes 54–64° and 64–72°, respectively.
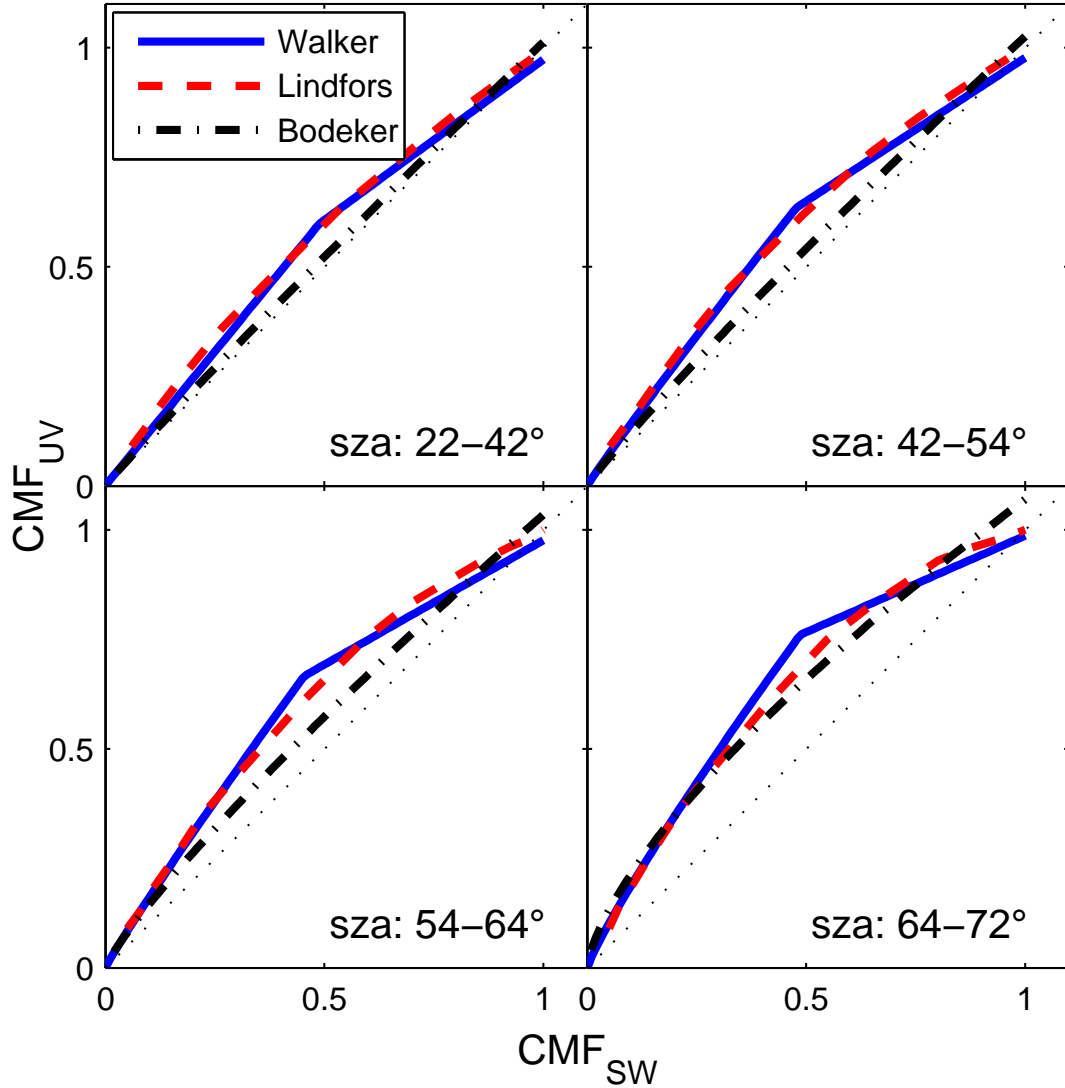

FIG. 4.7: Relationships between CMF_{SW} and CMF_{UV}, derived after the parameterizations described in this study (Walker) and two previous investigations: Lindfors and Bodeker (cf. Bodeker and McKenzie, 1996 and Lindfors et al., 2007). The curves are calculated for the four different SZA-classes used in this study at the median SZA (34°, 48°, 59°, and 68°) of all data of the respective class. (Note: for reproducing the parameterizations derived by Bodeker and McKenzie (1996), the coefficients from their empirical model are used)

4.5   Discussion and conclusions

This study presents a method to model erythemal UV radiation for all-sky conditions with a high temporal resolution of 10'. Our approach is based on semi-empirical relationships between the cloud effects in the SW and UV radiation. Modeled UV for clear-sky conditions is modified by a cloud modification factor (CMF) to account for varying cloud effects. We derived such relationships between CMFs in the UV and SW range for four stations in Switzerland where UV is operationally measured. These allow describing the cloud effects in the UV using observed attenuation of SW radiation with reference to clear-sky estimates.

The relationship was parameterized by two linear regressions of CMF_{UV} vs. CMF_{SW}, describing stronger and weaker cloud effects separately with two different slopes. The dependencies of this parameterization on environmental factors such as total ozone, solar zenith angle (SZA), and surface reflectance were assessed. Only the SZA was found to have a significant effect on the relationships. Furthermore, the inter-station differences were also found to be small. Therefore, the final relationships were inferred using a combined data set of all four stations, but divided in four different SZA-classes. These relationships achieved a high degree of generalization, since they led to good validation results at all four stations located in regions with different climate conditions representative for Switzerland. Thus, these relationships can not only be used to extend existing UV time-series into the past, but also to estimate UV wherever SW radiation is measured in Switzerland. The high time resolution, chosen to derive our method, enables capturing the short-term variability of UV radiation caused by rapidly changing cloud coverage. The necessary input data for estimating all-sky UV with our method are: (1) the total ozone and (2) surface reflectance as input variables to the radiative transfer model and (3) observed SW radiation to estimate the cloud effects.

The resulting time-series of estimated UV radiation with 10'-resolution were compared with independent data at the four locations in Switzerland where UV is operationally measured. The diurnal cycle and the short-term variability in UV radiation due to changing cloud coverage are well reproduced by our method. Over the whole validation period, the RMS errors between estimated and observed UV radiation range from 4.3 to 6.9 mW m^{-2}, corresponding to 9.4 to 11.9%. Linear regressions between the two quantities led to slopes between 0.96 and 1.03 with absolute intercepts of at most 0.88 mW m^{-2}. The performance of the model was found to be better for small SZAs, while relative differences increase towards larger SZAs. This SZA dependency of the modeling performance is also observed when estimating UV and SW radiation for clear-sky conditions (cf. Table 4.3). In general, the modeling yields larger uncertainties for large SZAs (longer atmospheric pathways) due to enhanced effects of the uncertainties in the atmospheric composition (e.g., ozone and aerosols). Furthermore, the smaller absolute radiation levels also lead to larger relative errors. Nevertheless, we used relative errors because they better express the model's capabilities also in difficult situations compared to absolute errors, which might be more appropriate in applications such as public health.

As expected, validation led to smaller RMS differences (5.4–8.0%) when aggregating the data on daily doses, while similar regression slopes were obtained. The smallest improvement of the performance for estimated daily doses compared to 10'-data was found at Locarno-Monti, where the systematic error in the estimated 10' data was largest.

The comparison between observed CMF_{UV} and CMF_{SW} showed most CMF_{UV} data above the 1-to-1 line (cf. Figure 4.2), indicating a stronger cloud effect on SW than on UV radiation. This behavior is in agreement with previous studies, and has been explained for instance by Bernhard et al. (2004), who compared modeled radiation for cloudy and clear-sky conditions. They found smaller cloud attenuation at shorter wavelengths, which was more pronounced for larger SZAs. The reason for this higher transmittance is the larger contribution of diffuse light to the total irradiance, which is more pronounced for shorter wavelengths and for large SZAs. Therefore, the spectral dependence of cloud attenuation can mostly be explained by the wavelength dependent radiance distribution (diffuse vs. direct) at the cloud top and the incidence-angle-dependent cloud transmittance (Bernhard et al., 2004).

This effect was further investigated in a modeling study by Lindfors and Arola (2008). Their analysis of the different radiation fluxes revealed two driving mechanisms for the different cloud attenuation of shorter and longer wavelengths: (1) the backscatter of upward reflected radiation from the cloud top that more strongly reinforces the downward radiation for shorter wavelengths for which Rayleigh scattering is more effective and (2) the higher cloud transmittance of diffuse radiation compared to global radiation (direct and diffuse) for large SZAs. The latter process explains the SZA-dependence of the difference in cloud effect for SW and UV radiation due to the larger diffuse contribution for shorter wavelengths, which increases for large SZAs. Another process leading to larger UV transmission is the variable absorption within the cloud of radiation with wavelengths longer than 700 nm, since the SW range includes the near infrared spectra (cf. Wiscombe et al., 1984).

Beside the generally stronger cloud effect in the SW, we also observed a change in the slope of CMF_{UV} vs. CMF_{SW} depending on the magnitude of the cloud attenuation. For overcast cloud conditions with strong attenuation, a small change in the cloud optical thickness for SW leads to larger changes in the UV range, in agreement with the theoretical arguments presented in the previous paragraph. This effect is reversed for broken and scattered cloud conditions with weaker cloud attenuation (CMF_{SW} above ∼0.5) where a change in the SW transmission results in a smaller change in the UV. We think this is related to the effect of the direct sun component being more important for the SW range: Situations of broken cloud coverage with changing sun screening result in a high variability of the direct component. When the sun is not shaded by a cloud, the fraction of the direct component in the global irradiance is much larger for the whole SW range than for the UV range. Thus, the enhanced variability has a weaker effect on UV than on SW, leading to the slope of the CMF_{UV} vs. CMF_{SW} relationship being lower than one for large CMF_{SW}. This difference in the relative strength of the direct component for SW and UV is also more pronounced for high SZAs. The combination of the behaviors discussed above for low and high CMF_{SW} leads to the bend we observed in the CMF_{UV} vs. CMF_{SW} relationships, and it also explains why it is more marked for high SZAs.

Beside the considerations mentioned above, residual analysis also confirmed the appropriateness of parameterizing this bent relationship with two different linear regressions. This is corroborated when displaying separately CMF_{UV} vs. CMF_{SW} for different cloud conditions (Figure 4.8). In this case, the separation between completely overcast and scattered cloud conditions is achieved using the independent APCADA algorithm (Duerr and Philipona, 2004). The upper panel of Figure 4.8 shows events that are totally overcast according to APCADA, and as expected, the vast majority is at CMF_{SW} below 0.5.

In addition the CMF_{UV} vs. CMF_{SW} relationship clearly exhibits a slope higher than one for these situations. A few events are located at CMF_{SW} larger than 0.5, which is due to the fact that the APCADA algorithm is based on longwave (thermal) radiation, and its selection of totally overcast cases may include few cases with strong cloud cover, but with few holes through which direct sun may occur. On the lower panel, cases with scattered cloud conditions are displayed. In this case the majority of events are at CMF_{SW} above 0.4, and the relationship clearly exhibit a slope lower than one. There is still a significant fraction of events that are at low CMF_{SW}, because a relatively wide range of cloud cover fractions (3–6 octas) was selected. These low CMF_{SW} events are those with the larger cloud cover fraction in this sample. This separation of cloud modification factors for overcast and scattered cloud situations around CMF_{SW} of 0.4–0.5 corresponds well with the position of $CMF_{SW,break}$ between 0.45–0.49, separating the relationship into an upper and lower regression (cf. Table 4.5).

Our comparison of the relationships derived from our method with those of B96 or L07 revealed that all three methods derive CMF_{UV} vs. CMF_{SW} relationships that start at the origin ($CMF_{UV} = CMF_{SW} = 0$) with a slope higher than one, then exhibit a curvature to finally pass close to the $CMF_{UV} = CMF_{SW} = 1$ point. The main difference resides in the location of the maximal curvature or bend. In the case of the B96 parameterization, a power law with the exponent being between 0.65 and 0.98, depending on the SZA, was chosen as a functional form. With such a choice, the maximum curvature (maximum absolute value of the second-order derivative) is always reached for $CMF_{SW} = 0$, which was not very appropriate for reproducing the observed shape of the CMF_{UV} vs. CMF_{SW} scatterplots in our study (e.g. Figure 4.2). In our method, the bending point (which we designed as breakpoint) was determined statistically. Its location was found to be robust at CMF_{SW} around 0.4-0.55, which was by definition well adapted to the data. Furthermore, the choice of two linear functions (or quasi-linear in the case of low CMF_{SW}) proved appropriate to reproduce the shape of the scatterplots. Finally, the model-based approach of L07 produced maximum curvature at higher CMF_{SW} around 0.7-0.8. However, their relationships were remarkably similar to ours, especially considering that the L07 method always uses 100% stratiform cloud coverage. This does not imply that a stratus, covering 100% of the sky, is an appropriate representation of any type of cloud and cloud cover for modeling radiation in the UV and SW range, but that the changes of CMF_{UV} relatively to changes in CMF_{SW} can be relatively well estimated using such a modeling approach. In the case of broken cloud coverage or cloud types very different from stratus, it may be due in large part to compensating errors.

Going beyond the similarities between the relationships of these two methods, we may gain insight into the effect of scattered cloud coverage by studying their differences. Even though these differences are small, they seem to be consistent and real. These differences are more pronounced for intermediate CMF_{SW} that most likely correspond to such scattered cloud coverage. Over a large range of CMF_{SW}, the L07 approach results in a small or negligible amount of direct radiation since direct radiation decreases rapidly with increasing cloud optical depth. It is only when very thin clouds (low optical depth corresponding to large CMF_{SW}) are simulated that the flattening of the relationship occurs, because the direct component quickly increases. On the other hand, the real broken cloud situations include large variation of the direct component already for much lower CMF_{SW}. This explains why the location of strongest curvature is at higher CMF_{SW} in the L07 method than in ours. More insight could probably be gained from such method
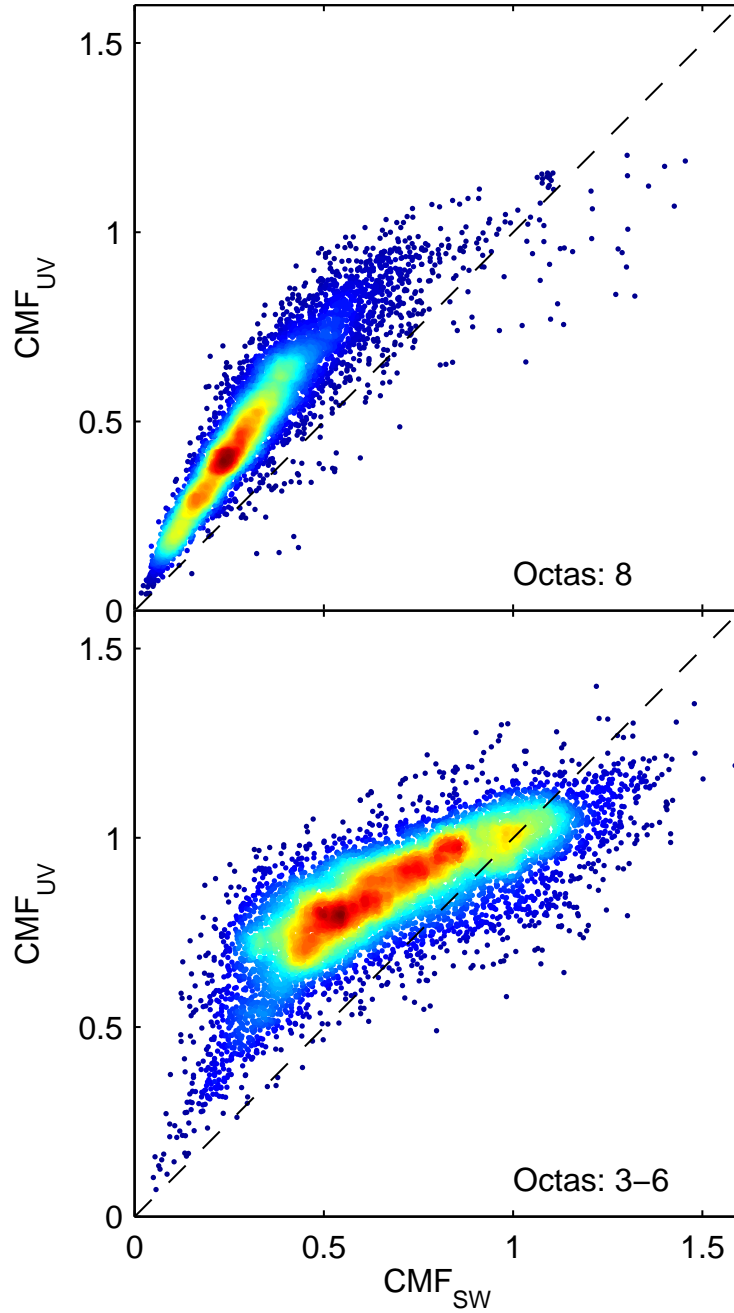
FIG. 4.8: The dimensionless cloud modification factors (CMF_{SW}, CMF_{UV}) of the combined data set for different cloud coverage and large solar zenith angles, corresponding to the class separation presented in Table 4.4 (SZA 64–72°). Upper panel: only data for completely overcast conditions (8 octas), lower panel: scattered and broken cloud situations (3-6 octas). The colors refer to the data density on the scatterplot (red: high density, blue: small data density).

comparisons in combination with 3-dimensional modeling of radiative transfer through clouds. However this represents a full domain of research in itself that goes beyond the scope of this study.

The assumption that a generalized method can be applied to any location in Switzerland (and possibly elsewhere) is strengthened by the fact that our empirical method, based on a data set incorporating various cloud situations in regions with different climatic conditions, results in relationships similar to those obtained by a pure model-based approach. The derived method can be currently applied at about 70 meteorological stations in Switzerland, where SW is continuously measured at a 10' time resolution. In the near future, a modernized and extended observation network will make the application possible at around 130 stations. This will allow producing UV radiation maps, which account for the spatial variability of the cloud cover and the complex alpine topography found in Switzerland. Such applications are essential for improving the understanding of the spatial variability and temporal evolution of UV radiation. Furthermore, the derived relationships allowed illustrating some theoretical considerations of previous studies with observed data in Switzerland.

Chapter 5

UV reconstruction and trend analysis

The successful validation of estimated all-sky UV against observations at four locations in Switzerland showed the ability of our method to assess the regional and temporal variability of erythemal UV radiation (cf. Chapter 4). The parameterization presented in Section 4.3.c is used for reconstructing all-sky UV radiation at the four SACRaM stations (Payerne, Davos, Jungfraujoch and Locarno-Monti) for the time period between 1981 and 2007. In this chapter, the temporal evolution of the reconstructed time-series is presented.

The reconstruction method (Equation (4.2)) uses the total ozone, the effective surface reflectance and observed total solar radiation (SW) as input parameters. While the development and validation in the previous chapter is based on radiation data with 10 minutes time resolution (10'), the following long-term reconstruction is performed on hourly SW time-series. This change in time resolution from 10' to hourly means was decided because the historical SW radiation at hourly resolution is of better quality as a result of corrections by Moesch and Zelenka (2004). Total ozone observations from Brewer spectrophotometers at Arosa are available since 1995. For earlier time-periods without Brewer observations, a combination of total ozone measurements with Dobson instruments at Arosa (cf. Staehelin et al., 1998b) and for days without such observations, the ozone reconstruction model by Krzyścin (2008) is used. Climatological corrections, based on balloon sounding data at Payerne, are added to account for tropospheric ozone between the SACRaM stations and Arosa. The effective surface albedo is estimated as described in Section 4.3.a, using the reconstructed regional snow distribution presented in Chapter 3. For the reconstruction of erythemal UV radiation we considered only data for periods with a solar zenith angle smaller than 72°.

5.1   Seasonal Mann-Kendall test and Sen's slope estimator

The residuals of least-square regressions on the time-series of erythemal UV radiation are not normally distributed and show various autocorrelations due to seasonal and daily cycles and because of successive periods of good and adverse weather. Therefore, we assess the temporal evolution of reconstructed UV radiation using seasonal Mann-Kendall tests (MK) in combination with Sen's slope estimates rather than by a least-square lin-

ear regression model. MK tests and Sen's slopes are non-parametric statistical methods based on the rank of the data. This allows performing trend estimates also for data with non-normally distributed noise, but some statistical efficiency is lost.

Seasonal Mann-Kendall Test

The Mann's test we use for the long-term trend analysis is a particular application of the Kendall's test for correlation (Kendall, 1938, 1975), commonly known as Kendall's tau. In our study, the Mann-Kendall statistic S for the data set x_i of length n is used to assess the significance of a temporal increase or decrease:

$$S = \sum_{k=1}^{n-1} \sum_{j=k+1}^{n} \text{sgn}\left(x_j - x_k\right) \quad \text{, where sgn}\left(\theta\right) = \begin{cases} 1 & \text{if } \theta > 0 \\ 0 & \text{if } \theta = 0 \\ -1 & \text{if } \theta < 0 \end{cases} \tag{5.1}$$

Thus, S indicates the dominance of concordant or discordant pairs in the data and can be interpreted as a measure for the strength of an existing temporal trend, based on the ranks of the individual observations. The test statistic S is normally distributed for $n > 10$ as shown by both Mann and Kendall, who derived the exact distribution of S also for smaller data sets. The calculation of the variance of S takes into account the presence of ties in the data and of ties in time. Thus, the standard normal variate Z of S is derived, using:

$$Z = \begin{cases} \frac{S-1}{\sqrt{\text{var}(S)}} & \text{if } S > 0 \\ 0 & \text{if } S = 0 \\ \frac{S+1}{\sqrt{\text{var}(S)}} & \text{if } S < 0 \end{cases} \tag{5.2}$$

The standardized Z indicates increasing and decreasing trends by its sign and can be tested for significance using $|Z| \leq Z_{\alpha/2}$, $F_N(Z_{\alpha/2}) = \alpha/2$. F_N is the standard normal cumulative distribution function and α represents the significance level to reject or accept the hypothesis that the observations are randomly ordered and no monotone trend over time exists. The Mann-Kendall test was extended by Hirsch et al. (1982) for taking the seasonal variability of the tested variable into account, including multiple observations per season. Furthermore, Hirsch and Slack (1984) introduced a consistent covariance estimator for treating correlated data developed by Dietz and Killeen (1981). For this trend analysis, the autocorrelation was taken into account by increasing the variance using the procedure described by Hamed and Rao (1998).

Sen's slope estimator

The Sen's slope estimator (Sen, 1968) is closely linked to the Mann-Kendall test and is used for assessing the magnitudes of statistical significant temporal changes previously identified by the MK test. The method calculates the variable's change per unit time interval of all data pairs $x_i\left(t_i\right)$ and $x_j\left(t_j\right)$:

$$A_{[ij]} = \frac{x_j - x_i}{t_j - t_i} \quad \text{, for } j > i \text{ and } t_i \neq t_j \tag{5.3}$$

The median value of all individual slopes of $A_{[ij]}$ defines the temporal trend, and its 90%-confidence interval is estimated following the method by Gilbert (1987).

Homogeneity of trends in different seasons

The trend analysis below is performed for each month separately. However, also the annual temporal evolution is assessed including the data of all seasons. Even significant trends over the whole year are only meaningful if the monthly trends are homogeneous such that they indicate for most seasons a consistent increase or decrease, respectively. This homogeneity is tested, following the method described by Gilbert (1987):

$$\chi^2_{\text{homog}} = \chi^2_{\text{total}} - \chi^2_{\text{trend}} = \sum_{i=1}^{K} Z_i^2 - K\overline{Z}^2 \qquad , K = 12 \qquad (5.4)$$

The hypothesis of homogeneous monthly trends over time is rejected, if χ^2_{homog} exceeds 4.57, representing the critical value for $\alpha = 0.95$ of the χ^2 distribution with 11 $(K-1)$ degrees of freedom.

The presented trend analysis focuses on the magnitudes of the linear trends and their statistical significance ($p \leq 0.05$). The trends are described by the Sen's slope estimates on the daily median values for solar zenith angles smaller than 72°, indicating for each month separately the yearly change, including the 90% confidence interval. The significance of a trend is assessed by the standardized Kendall's S (Equations (5.1) and (5.2)) derived from hourly data.

5.2 Results

The trend analysis for reconstructed erythemal UV radiation is presented for each month in Figure 5.1. The data of all four stations (Payerne, Davos, Locarno-Monti, and Jungfraujoch) show positive annual trends for the first half-year, reaching significant values between $+0.56$ and $+1.15\%$ yr^{-1}. The average absolute trends at all four stations increase from January to June from $+0.17$ to $+0.66$ mW m^{-2} yr^{-1} and become also most statistically significant in June (Table 5.1). In May and June, all estimated trends are significant with p-values below 0.03. The estimated annual changes in these two months ranges from 0.56-1.05% yr^{-1}, corresponding to 0.50-0.79 mW m^{-2} yr^{-1}. Over the period between 1981 and 2007 this annual change enhanced the UV-Index (UVI) in May and June by 0.54–0.85. For the months of the second half year, the trends are mostly positive but rather weak and usually non-significant ($p > 0.05$). The trend estimates for the whole year are positive and highly significant at all four stations ($p \leq 3 \cdot 10^{-5}$). However, these annual trends should be taken with caution due to quite inhomogeneous monthly trends ($\chi^2_{\text{homog}} > 5.1$ for all stations, cf. Equation (5.4)). As a consequence, only the monthly Kendall tests and Sen's slope estimates should be considered for further conclusions.
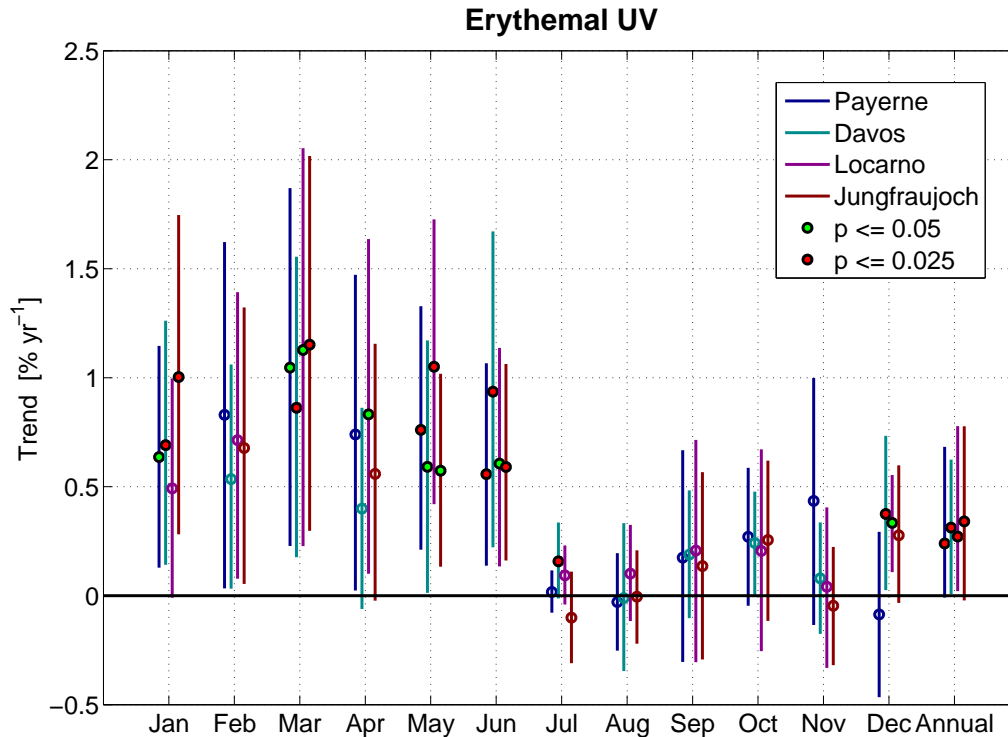
FIG. 5.1: Monthly linear trends (in % yr^{-1}) of erythemal UV radiation using daily median values between 1981 and 2007. The "annual" results refer to the trend analysis over the whole year instead of separating the data for each month. The vertical lines represent the two-sided 90% confidence interval. The color of filled markers refers to the confidence level of an existing trend based on the Mann-Kendall test for hourly data (red: $p \leq 0.025$, green: $0.025 < p \leq 0.05$).

The same trend analysis is applied on total ozone, observed SW radiation, and the surface reflectance. In Figure 5.2, the estimated trends in total ozone and SW radiation are presented. For the total ozone (upper panel), the Sen's slope estimations indicate a decrease in the first half-year. These negative trends are significant for May and June with slopes of -0.28 and -0.19% per year, respectively. This corresponds to a total decrease of 26 and 17 DU ($\sim$5-7%) over the whole period between 1981 and 2007. For the months of the second half-year no significant trends are found.

The analysis for SW radiation (lower panel, Figure 5.2) shows mostly positive trends for the months of the first half-year. In spite of several positive trends with Sen's slope confidence intervals excluding zero, only a few of them are identified statistically significant by the Mann-Kendall test ($p \leq 0.05$). The largest significant positive trends were found at Locarno-Monti for February and March (0.65–0.69% yr^{-1}) and at the Jungfraujoch during March (+0.67% yr^{-1}), corresponding to annual increases between 2.5–3.3 W m^{-2}. Also the trends for the second half-year are mostly positive at all four stations, but aside from one exception at Locarno-Monti in December they are all identified as non-significant by the MK test ($p > 0.05$). Again, the monthly trends are too inhomogeneous ($\chi^2_{homog} > 6.6$) for deriving representative annual trends for both, the total ozone and SW radiation.

The data of the surface reflectance is less suitable for this trend analysis. Most Sen's slope estimates are found to be zero, indicating no trend in the presence of snow. These

TABLE 5.1: Estimated monthly trends for the reconstructed daily median UV radiation at Payerne, Davos, Locarno-Monti, and Jungfraujoch. The trends describe the annual change in mW m^{-2} for each month separately. For each station and month, the Sen's slope including the 90% confidence interval is given. Furthermore, the p-value for the existence of a trend is added, derived from the standardized Kendall's S values based on hourly data. Additionally, the percental change of erythemal UV radiation is given (chng, % yr^{-1}). All p-values ≤ 0.05 are indicated in bold ($\alpha = 0.1$, two-sided).

	Payerne				Davos			
	slope	conf.-interval	p-val	chng	slope	conf.-interval	p-val	chng
1	0.098	[+0.019,+0.176]	**0.040**	0.636	0.188	[+0.033,+0.338]	**0.020**	0.690
2	0.199	[+0.009,+0.389]	0.063	0.829	0.212	[+0.003,+0.411]	0.063	0.535
3	0.412	[+0.088,+0.734]	**0.028**	1.046	0.519	[+0.102,+0.932]	**0.023**	0.862
4	0.416	[+0.004,+0.819]	0.085	0.739	0.320	[−0.051,+0.690]	0.090	0.400
5	0.552	[+0.140,+0.951]	**0.023**	0.761	0.501	[+0.010,+0.991]	**0.026**	0.591
6	0.518	[+0.045,+0.908]	**0.021**	0.558	0.787	[+0.169,+1.387]	**0.005**	0.936
7	0.016	[−0.077,+0.105]	0.275	0.017	0.156	[−0.020,+0.324]	**7e-06**	0.158
8	−0.022	[−0.194,+0.149]	0.341	−0.029	-0.009	[−0.303,+0.277]	0.278	−0.011
9	0.109	[−0.198,+0.407]	0.180	0.175	0.134	[−0.076,+0.341]	0.197	0.188
10	0.093	[−0.016,+0.201]	0.121	0.270	0.115	[−0.003,+0.227]	0.095	0.242
11	0.085	[−0.025,+0.196]	0.112	0.435	0.025	[−0.056,+0.105]	0.213	0.080
12	−0.011	[−0.059,+0.037]	0.360	−0.086	0.092	[+0.004,+0.178]	**0.014**	0.375

	Locarno-Monti				Jungfraujoch			
	slope	conf.-interval	p-val	chng	slope	conf.-interval	p-val	chng
1	0.099	[−0.002,+0.199]	0.087	0.492	0.311	[+0.081,+0.535]	**0.016**	1.003
2	0.207	[+0.010,+0.391]	0.088	0.713	0.310	[+0.015,+0.595]	0.058	0.678
3	0.498	[+0.089,+0.896]	**0.028**	1.127	0.792	[+0.194,+1.379]	**0.007**	1.151
4	0.483	[+0.016,+0.908]	**0.044**	0.832	0.509	[-0.035,+1.038]	0.119	0.559
5	0.764	[+0.273,+1.223]	**0.006**	1.050	0.632	[+0.143,+1.117]	**0.030**	0.574
6	0.569	[+0.071,+1.012]	**0.029**	0.606	0.776	[+0.155,+1.340]	**0.011**	0.590
7	0.088	[−0.042,+0.213]	0.131	0.093	−0.136	[−0.421,+0.146]	0.321	−0.101
8	0.080	[−0.097,+0.253]	0.379	0.101	−0.005	[−0.250,+0.242]	0.439	−0.005
9	0.137	[−0.198,+0.474]	0.181	0.207	0.129	[−0.279,+0.535]	0.261	0.136
10	0.083	[−0.105,+0.268]	0.203	0.206	0.163	[−0.069,+0.399]	0.085	0.255
11	0.010	[−0.079,+0.101]	0.393	0.041	−0.018	[−0.122,+0.087]	0.435	−0.046
12	0.061	[+0.021,+0.103]	**0.027**	0.334	0.078	[−0.012,+0.165]	0.083	0.277

zero-slopes are resulting from a large number of identical albedo values caused by situations with snow-free conditions or complete snow coverage in the close vicinity of the stations. The temporal evolution of the regional snow cover in Switzerland, which is also linked to the effective surface reflectivity around each station analyzed in this section, is investigated in more detail in Chapter 3.
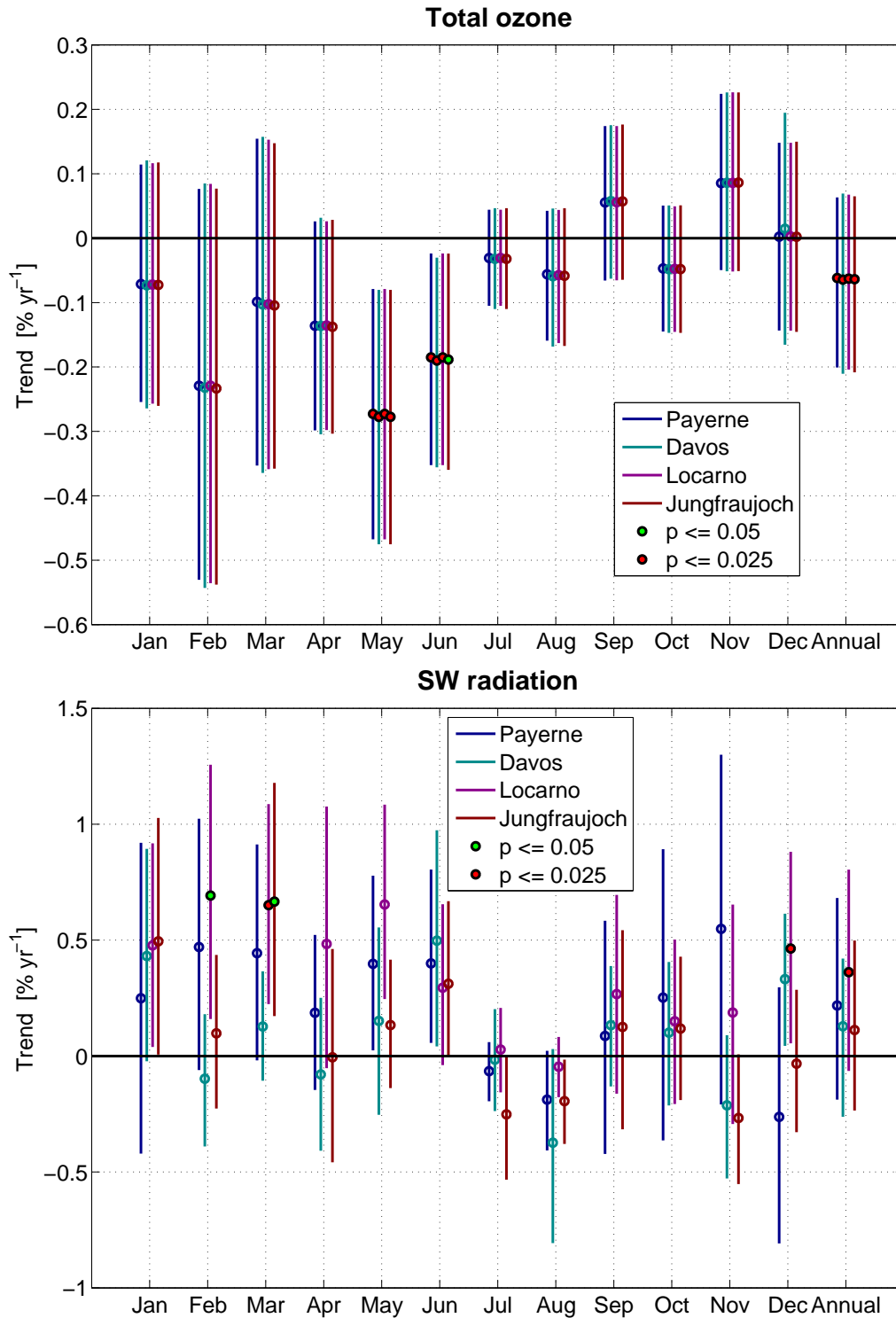
FIG. 5.2: Estimated trends for observed daily median total ozone (upper panel) and SW radiation (lower panel). The trends for total ozone are very similar for all four stations since the most ozone data come from measurements at Arosa. However, the ozone trends at all four stations are shown in order to be consistent with the trend visualizations of erythemal UV and SW radiation. Further details are given in the caption of Figure 5.1.

5.3 Discussion

The strongest annual percentual increase of the daily median erythemal UV radiation was found in March (0.86–1.15% yr^{-1}). For this month, UV radiation increased over the whole time period (1981–2007) by 0.44–0.86 UV-Indexes (UVI). In absolute terms, the changes are larger in May and June, where the incoming UV radiation increased over the whole period by 0.54–0.85 UVI. The decline in ozone, which is most significant in May and June, and the tendency of increased SW radiation especially for January to March and May provoke this increase in UV radiation during months of the first half year. The decrease in the regional snow cover in Switzerland (cf. Chapter 3), on the other hand, which is most pronounced at low altitudes, counteracts the UV increase especially at the lowland station Payerne and to some extent also at Locarno-Monti.

These found increases of almost 1 UVI over the past three decades are considerable since UV-Indexes of around 7–8 are reached for instance at Payerne for clear-sky conditions during May and June. However, the shown trends represent the changes in the median daily all-sky UV radiation and therefore are not equivalent to a general rise of clear-sky UV radiation by this magnitude. The clear-sky UV radiation in the months May and June is strongly influenced by the evolution of the total ozone, which decreased by 1.9–2.8% dec^{-1}. Such a decline provokes an increase in clear-sky erythemal UV radiation by 2.1–3.1% dec^{-1} (cf. Equation (5.5), below). These considerations give also an idea about the changes of the maximal daily UV radiation, since this value often corresponds to clear-sky conditions.

There are previous studies, which also estimated trends in UV radiation. Lindfors and Vuilleumier (2005) reconstructed daily erythemal UV doses at Davos back to 1926, estimating cloud effects with sunshine duration. They found positive trends of around 6.6 and 6.1% per decade for winter and spring seasons (1979-1999). These values correspond well with the decadal increase we found in our study at Davos (5.3 and 6.2% for winter and spring). A trend analysis of reconstructed erythemal daily doses at Hohenpeissenberg ($\sim$1000 m MSL) between 1968 and 2001 revealed an increase in the months April to June of 3.2–5.4% per decade (Trepte and Winkler, 2004). Compared to the average positive trends of 4.8-7.6% for these months at the elevated stations in our study, Davos and Jungfraujoch, the trends at Hohenpeissenberg are smaller. Assuming that a considerable amount of the long-term UV trends are due to the ozone depletion after 1975 (Solomon et al., 1986), these smaller linear trends can partly be explained by the inclusion of the period before 1975 by Trepte and Winkler (2004). A study by Rieder et al. (2008) investigated the temporal evolution of daily erythemal UV doses at Vienna and Hoher Sonnblick (Austria). They compared yearly averaged values for different seasons over two periods between 1986 and 2005 to a reference period (1976-1985). The increase of the yearly averages from the reference period to the successive decade are very large at Vienna (+29%) and somewhat smaller at Hoher Sonnblick (+14%) during winter months (DJF). These values are much larger than the monthly trends found in our study, where no decadal trend exceeds +10% during winter. For spring months (MAM), the increases at Vienna and Hoher Sonnblick (+9% and +7%) are more comparable to the average spring trends found at the stations in Switzerland (6.2–10.0%). These comparisons show

that the magnitudes of the trends found in this study are comparable to results of previ-
ous investigations. However, the range of trend values found by other studies is relatively
large, which may be explained by the different climate conditions, reconstruction tech-
niques, statistical analysis methods, and time periods used by those studies.

The temporal changes for total ozone are negative for the months of the first half year
and statistically significant for May and June. These negative trends in the first half
year are in agreement with the analysis of Staehelin et al. (1998a), who also found large
changes in winter and spring, while the trends from August to October were not statisti-
cally significant. The total ozone content is connected to the advection of polar (Arctic)
air. Some decrease in total ozone in winter is caused by a decreasing influence of this
polar air reaching the middle of the European continent (Staehelin et al., 1998a). The
significant negative decadal trends of -2.8 and -1.9% in May and June are somewhat
smaller than the trends of balloon sounding data (1970–2002) presented by Jeannet et al.
(2007). They found a decadal decrease of approximately -3 to -4% in the vertical ozone
distribution between the 100 and 10 hPa level (annual mean). Recent trend analysis of
total ozone at Arosa (1980–2007) showed linear decadal trends of -2.5 and -1.6% for May
and June, respectively, when anthropogenic influences were analysed isolated from natural
fluctuations (i.e. stratospheric aerosols, NAO- and EAWR-Index[1], and solar cycle). These
results are comparable to the decadal decrease of 2–3% found in this study. Similar trends
emerged also from an analysis of total ozone measurements at Arosa over the time period
between 1970 and 1996 (Staehelin et al., 1998a). They found negative decadal trends of
-2.3% for annual mean ozone and around -2% dec^{-1} for May and June, which correspond
well with the results of our trend analyis. However, Staehelin et al. (1998a) found larger
negative changes ($\sim$4%) for January–March, compared to the negative decadal trends
smaller than 2.3% found in our study. One reason for smaller trends resulting from our
study is the time period considered, ending in 2007. Compared to the analyses of Jeannet
et al. (2007) and Staehelin et al. (1998a) we include more years after the end of the 1990s,
where a beginning ozone recovery is anticipated. This can lead to an underestimation of
the decadal changes since the MK test and Sen's slopes assume monotonic linear trends
over the whole analyzed period. This underestimation of total ozone changes also affects
the UV trends, which are found to be smaller in our study compared to the results of
Lindfors and Vuilleumier (2005). Such changes in total ozone imply corresponding oppo-
site changes in erythemal UV radiation. For describing the impact of a small change in
total ozone on UV radiation, a linearization of the radiative amplification factor (RAF)
described by Madronich (1993) can be used:

$$\frac{\Delta D}{D_0} = -\text{RAF} \cdot \frac{\Delta \text{TOZ}}{\text{TOZ}_0} \tag{5.5}$$

where ΔD indicates the variation in the erythemal UV dose (D_0) due to changes in the to-
tal ozone (TOZ). The RAF value for erythemal UV doses is around 1.1 (Madronich et al.,
1998), which means that a total ozone decrease of 1% leads to an increase of 1.1% in the
erythemal UV dose for clear-sky conditions. For March, where the strongest increase in
UV radiation was found, the decrease in ozone is relatively weak (-0.1% per year) and
not significant. Thus, this little change in ozone cannot entirely explain the annual UV
increase between 0.86-1.15%, considering a RAF of 1.1. The SW radiation, on the other

---

[1]East Atlantic/West Russia pattern, see Acronyms and Abbreviations (p. 98) for more details

hand, shows larger trends for March (i.e. between $+0.13$ and $+0.67\%$ yr^{-1}) compared to the rather small changes in total ozone. The temporal evolution of SW radiation is positive for January to March and June and significant trends are found for February and March. The well documented increase in SW radiation since the mid 1980s (cf. "solar dimming and solar brightening") is primary caused by changes in the anthropogenic aerosol emissions (cf. Norris and Wild, 2007; Ruckstuhl et al., 2008), while changes in the cloud cover cannot account for the trends in surface SW flux. However, Norris and Wild (2007) ascribed an observed decrease in SW cloud effects to the indirect aerosol effect influencing the albedo of the clouds. Also a previous satellite study detected a reduction in the cloud albedo of about 2% from the late 1980s to the late 1990s (Krüger and Graßl, 2002). This effect should be stronger in winter and spring, where overcast conditions are more frequent and therefore resulting changes in SW radiation are larger.

Wild et al. (2008) investigated trends of monthly mean downward SW radiation at 332 stations of the Global Energy Balance Archive (GEBA), based on monthly mean data. They found decadal increases of 1.4–1.7% over the period from 1986 to 2000, when excluding the Pinatubo-affected period. They considered an increase in downward surface solar radiation slightly above $+0.2$ W m^{-2} yr^{-1} ($\sim 1.3\%$ dec^{-1}) as best estimate over the period 1986–2000. Another trend analysis of monthly averaged global solar radiation in Germany (1978/9–2000) revealed, especially for stations in the south-western region, larger trends between 3.1–4.5% dec^{-1} (Power, 2003). In most studies, the temporal evolution of SW radiation is assessed for daily or even monthly means. In our analysis, the temporal evolution of the daily median radiation data is investigated, only including time periods when the sun is considerably above the horizon (SZA $< 72°$). This difference in the calculation of the radiative parameters tested for temporal evolution makes a quantitative comparison of the estimated trends difficult. Most decadal increases in SW radiation over the whole year range between 1.1 and 2.2% (non-significant) in our study and are comparable to the trends found by Wild et al. (2008). The slightly larger trend at Locarno-Monti ($+3.6\%$ dec^{-1}, significant) is still in good agreement with the results of Power (2003) for stations in South Germany. Further information about the seasonal contributions to these trends are given by Norris and Wild (2007) in their study about radiative effects of clouds and solar dimming and brightening over Europe. They subtracted cloud effects from observed all-sky SW radiation and investigated the temporal evolution of this residual component for different seasons. The strongest seasonal trend was found for springtime (February–April), with a decadal increase of this cloud-corrected component between 2.6 and 3.2% over the time period 1987–2002. Again, the different radiative parameter analyzed for temporal evolution makes a quantitative comparison difficult. However, the largest significant SW radiation trends in our analysis were also found for February and March, while the weakest temporal changes occurred in summer. The effects of enhanced SW radiation on erythemal UV change with the solar zenith angle and depend strongly on the cloud type and total cloud coverage (cf. Chapter 4). The impact of a change in cloud transmission in the SW range (CMF$_{SW}$) on UV radiation (CMF$_{UV}$) is presented on Figure 4.3. A change in cloud optical depth for strong cloud attenuation leads to an amplified effect (slope > 1) in the UV range, while the same change for scattered cloud coverage with CMF$_{SW} > 0.5$ has a weaker impact on UV than on SW transmission. No direct conclusions about the link between monthly SW and UV trends can be drawn since the cloud conditions and solar zenith angles are not resolved when analyzing daily median values.

The changes, which were found in the reconstructed UV time-series are a direct conse-
quence of trends in the used proxy-data (observed SW radiation, total ozone, and surface
reflectance). Therefore, no further attempt is made for physical interpretation of the re-
lation between the changes of the proxies and the trends of reconstructed UV radiation,
since they are not independently deduced. The direct impact of any changes in total ozone
and albedo on UV radiation is defined by the radiative transfer model and for observed
SW radiation by the relationships between CMF_{SW} and CMF_{UV} (Section 4.3.c).

Observed changes in the atmospheric aerosol concentrations are included by using SW ra-
diation as a proxy for the reconstruction of UV. Changes in the atmospheric turbidity due
to different aerosol loads are captured to some extent by the observed SW radiation and
transferred to the UV range by the CMF-relationships. However, changes in the aerosol
composition and size distribution are not explicitly considered in our reconstruction.

Chapter 6

Conclusions and outlook

6.1 Conclusions

UV radiation is an environmental factor not only influencing the atmospheric chemistry but also various ecosystems with important impacts on our daily life and human health. Clouds strongly modify the radiation levels at the ground and introduce a short-term variability to the diurnal evolution of UV radiation. The motivation for the presented study is therefore to advance the understanding of the influence of clouds on UV radiation. The effects of complex 3-dimensional cloud situations are very difficult to simulate with radiative transfer modeling. Hence, the presented studies focus on the description of cloud effects by a semi-empirical method, based on total solar radiation (SW).

The main goals of this thesis were the investigation of the appropriateness of such a method in the complex topography of Switzerland and the analysis of its characteristics in more details. Furthermore, the method's portability was assessed and conclusions were drawn about its application at locations where UV is not measured. The analysis was performed at four stations in Switzerland, contributing to the SACRaM-network where UV is measured operationally (Payerne, Davos, Jungfraujoch, and Locarno-Monti). A second study deals with the temporal evolution of the regional snow cover. This information is important because the diversified climatology of Switzerland involves a strong seasonal cycle in the presence of snow, which is the main factor for determining the surface reflectivity. A third part investigates the data quality of UV measurements at the four SACRaM stations. Different quality levels were identified, their consequences on the observed UV radiation assessed and a post-processing algorithm proposed to make the available time-series more homogeneous.

The results of these studies are discussed separately below, followed by an outlook at the end of this chapter.

Cloud effects on erythemal UV and SW radiation

The main result of this thesis is the study of cloud effects in the UV by the atmospheric transmission of SW radiation. These cloud effects were investigated by assessing the relationship between cloud modification factors (CMFs) in the SW and UV. The link between CMF_{SW} and CMF_{UV} was parameterized separately for scattered clouds and for strong cloud attenuation, which is usually linked to overcast conditions.

- Observed cloud effects on UV and SW radiation show the same characteristics at all SACRaM stations in Switzerland.

- The relationship between CMF_{SW} and CMF_{UV} mainly depends on the solar zenith angle (SZA), while other local conditions, such as total ozone, surface reflectance, and the topography are only of minor importance.

- Observed cloud effects on UV radiation are smaller compared to SW radiation. In other words, for a given cloud situation, CMF_{UV} is closer to unity (no cloud effect) than CMF_{SW}. This observation confirms theoretical considerations and previous modeling results also at these four stations.

- The relationship between UV and SW cloud effects changes for different cloud situations: a given change in the cloud optical depth for strong cloud attenuation results in larger CMF changes for UV than for SW radiation. The opposite is true for scattered cloud conditions, when direct sunlight often passes through the broken cloud cover.

- The position where the relationship was separated into an upper and a lower regression by an iterative procedure on observed CMF data ($CMF_{SW,break}$) corresponds well with the separation of the CMF data into overcast and scattered situations by an elaborated cloud detection tool. This supports the chosen approach to treat small and large CMFs separately.

- The observed cloud effects agree well with the results of a fully model-based approach. However, the locations where the relationships have their strongest bends clearly differ between the two methods for larger SZAs. These differences could be related to the fact that the modeling approach uses exclusively stratiform clouds, while the presented method in this study is based on a wide range of real cloud situations, including scattered and cumulus clouds.

The derived relationship between CMF_{SW} and CMF_{UV} reaches a high level of generalization since the most important influence comes from SZA, which can be derived for any location. This portability of the method without further adaptations is additionally supported by the agreement with the modeling approach, which neither accounts for the local topography nor for the actual cloud characteristics. Therefore, cloud effects on UV radiation can be assessed at more than 130 stations of the new SwissMetNet and information back to the early 1980s become available.

All-sky UV model

From the previously discussed study of cloud effects emerged an all-sky model for deriving erythemal UV, wherever SW radiation is observed and information on total ozone and surface reflectance is available.

- Estimated UV radiation showed RMS errors to observations smaller than 7 mW m^{-2} ($< 11.9\%$) at the four SACRaM stations and a time resolution of 10 minutes.

- The performance of the model improved (RMS: 8.4–9.7%) for situations with small SZAs ($< 42°$).

- The aggregation on daily doses led at all four stations to a good agreement with observations (RMS: 5.4–8.0%).

These validation results confirm that the derived method successfully describes the short-term variability of UV radiation due to clouds. Furthermore, UV can satisfyingly be estimated at all four SACRaM stations covering climate conditions ranging from the Swiss lowlands to the high-alpine environment. The validation showed especially good results for small SZAs corresponding to periods with higher UV doses, which are more relevant for public health.

UV trend analysis

The derived relationship was used for reconstructing UV radiation at the four SACRaM stations for the time period between 1981 and 2007. The reconstructed UV time-series and the used proxy-data were analyzed for monthly trends using non-parametric Mann-Kendall tests and Sen's slope estimations.

- Positive decadal trends for the median daily UV values between 5.6–11.5% were found during months of the first half year (January-June). The trend analysis revealed largest percental UV changes for March with a decadal increase ranging from 8.6 to 11.5%. In May and June, the UV-index increased by 0.54–0.85 units over the last 27 years.

- The analysis of observed total ozone showed generally negative trends for the months of the first half year, which are significant for May and June. Afterward, the trends for the months July to December are smaller and statistically non-significant. For the months May and June, negative decadal trends of 2.8 and 1.9% were found.

- Most trends for SW radiation are found to be non-significant by Mann-Kendall test. However, the trends of the first half year tend to be positive and a significant increase is found for February and March at Jungfraujoch and Locarno-Monti (6.5-6.9% dec^{-1}).

- The derived trends for the annual data are often significant, especially for UV and total ozone, but the monthly trends are inhomogeneous and therefore the significance of the annual trends is reduced.

The temporal changes of UV radiation at the four stations in Switzerland are comparable with results of previous studies and at other locations. The impact of an increased UV-Index of 0.54–0.85 for May/June can be illustrated by the reduction of the sunburn-time by 3 to 6 minutes ($\sim$-15%), when increasing the UV-Index by 1 unit at Payerne for clear-sky conditions in May. However, the found changes of the UV-Index refer to the increase of the daily median UV radiation for **all-sky** conditions, while the change of the maximal clear-sky UV-Index is smaller because it is mainly caused by the temporal evolution of ozone.

The temporal evolution of observed SW radiation and total ozone was identified as being non-significant for most stations and months. Thus, the significant increase of UV radiation found at most stations in January–June results from the combination of mainly non-significant increases of SW radiation and reductions of ozone. The significant decrease in regional snow cover (discussed below), on the other hand, counteracts the UV reinforcing effects from SW and ozone changes.

Aerosols & atmospheric composition

The most important environmental factors influencing clear-sky UV radiation beside the sun elevation are total ozone, surface reflectance, and the atmospheric turbidity (i.e. aerosols). Stratospheric and tropospheric ozone variations are well monitored in Switzerland by long-term total ozone observations at Arosa and regular balloon soundings at Payerne. The spatial variability of snow was investigated in more details in this thesis because of its known effects on the down-welling irradiance. The vertical structure of the atmosphere, including the aerosol composition and amount, on the other hand, was derived from average profiles for mid-latitudes and from a standard aerosol model. The validation of the radiative transfer model for clear-sky conditions demonstrated that these profiles are appropriate for describing the conditions found in Switzerland. However, this good agreement could also be reached to some extent by compensating errors. The day-to-day variability of the atmospheric turbidity is partly included by building the relationship between cloud modification factors for the UV and SW range. Therefore, changes in the atmospheric turbidity are captured by observed SW radiation and are transferred to some extent into the UV range by the derived relationships. However, changes in the aerosol composition and size distribution can not be considered using this method. We found some indications that a part of the seasonal radiation cycle especially in the UV was not reproduced by the model and was, at least at one station, covered to some extent by the optimization of the effective albedo boundaries for snow-free and snow-covered conditions. However, the direct radiative forcing of aerosols is much weaker in the presence of clouds, because incoming radiation is back-scattered by the cloud instead of by the aerosols (cf. Norris and Wild, 2007). Since our study is not limited to clear-sky conditions, cloud related effects may dominate in many situations over aerosol attenuation for all-sky conditions.

For further studies investigating the links between UV radiation and environmental factors, such as ozone, aerosols, or snow cover one should also include spectral radiation data. The Brewer spectrophotometers at Arosa not only proved to be highly stable over time but also offer maximum flexibility regarding wavelength range and weighting.

Regional snow cover in Switzerland

The reflectivity of the ground directly affects the down-welling irradiance by multiple reflections at the surface and back-scattering in the atmosphere above. The surface reflectivity is strongly determined by the presence and absence of snow. This is especially true for UV radiation, since most soil types show very low albedo (< 0.1), unless they are covered with snow.

- The temporal evolution of the regional snow distribution was studied using a method based on observed snow depth in combination with a digital elevation model.

- Snow cover in Switzerland was reconstructed back to 1980 and was validated against snow observations and satellite snow masks. In the cross-validation during winter periods (November–April), a POD of 0.96 and a FAR of 0.15 were found, while the post-agreement to satellite observations reached 69–97%.

- The trend analysis of reconstructed time-series showed a decrease of the snow cover between -10 and -15% in the lowlands north of the Alps. The negative trends in the more elevated alpine regions are smaller (1–8%) and statistically non-significant ($p > 0.1$).

The presented study confirms, that the regional snow cover can successfully be derived over the last 28 years in Switzerland, providing valuable information for describing the seasonal variability in surface reflectivity on a larger spatial scale. Despite the satisfying validation results of this snow study, a further development of the method could be considered in order to improve its performance especially at low altitudes. This would include further investigations of the regression technique using multiple slopes and the assessment of the chosen set of stations regarding their altitude distribution. Nevertheless, it will be difficult to achieve excellent modeling results in the lowlands, since not only the occurrence of snow is infrequent, compared to alpine regions but also the amount of snow is lower. Therefore both, the occurrence and the persistence of snow at these low altitudes depend strongly on local effects, which are difficult to assess with this method.

UV-data quality assessment

The data quality of erythemal UV measurements in Switzerland evolved over the past decade since first observations by the CHARM network started. Different quality levels were identified, which are closely related to the angular response and filter characteristics of the instruments. Ignoring these effects in the instrument's calibration process leads to systematic differences between observation and the model, which are especially strong for large SZAs and thus during winter seasons. Such a behavior strongly interfere with the investigation of cloud effects, which are also depending on the SZA.

- A post-processing algorithm is proposed, based on actual calibration data and methods similar to the standard calibration procedures described by Webb et al. (2007).

- This post-processing reduces systematic underestimation of the instruments compared to the model for large SZAs and corrects this pattern.

- The used algorithm improves the standard deviations of the model-to-observation ratio by 35–44%.

This thesis showed that the relationship between cloud effects in the UV and SW has the same characteristics in the lowlands and high-alpine environment and depends mainly on the solar zenith angle. Local influences, such as the topography or cloud characteristics that are not described by the clear-sky modeling are captured by the observed SW radiation. The SW transmission is strongly influenced by a wide range of cloud types and properties, whose radiative effects can hardly ever be modeled by RTMs in a general way. The varying radiation distribution (diffuse/direct) for overcast and scattered cloud cover causes a distinct change in the derived relationship, yielding two different slopes. These slopes can be interpreted as amplification factors of UV cloud effects due to changes in SW transmission.

The different characteristics of overcast and scattered cloud situations will help drawing conclusions regarding the evolution of UV when anticipating future climate changes with modified cloud types and properties. The surface energy budget, air pollution or circulation patterns are subject to changes in a future climate and can favor the formation of certain cloud types (e.g. convective or stratiform) and influence the clouds' reflectivity characteristics. The impacts of such changes can be investigated by continuously observing UV and SW cloud modification factors and by the derived relationships. Therefore, possible scenarios on future frequencies of overcast and scattered cloud situations can also be used to forecast their impacts on UV radiation. More specific conclusions can be drawn when investigating the radiative effects of actually observed cloud situations and situating them in the CMF-relationship. This may also include a more detailed cloud characterization by combining balloon sounding and remote sensing data available at Payerne. Such studies can be carried on further in order to compare the relationships with results from 3-dimensional modeling for selected cloud situations. The impact of future changes in winter precipitation on the surface reflectivity and UV radiation can additionally be investigated by the derived method for assessing the regional snow distribution.

The good validation results of estimated all-sky UV give further information about the advantages of the derived method: the differences between estimated and observed UV are only slightly larger than the instruments' uncertainties. This is the result of a good description of the link between atmospheric transmission in the SW and UV range and also due to the assessment of cloud effects using pyranometer measurements with superior accuracy compared to UV biometers.

The description of the radiative transfer also in a cloudy atmosphere allows reconstructing UV radiation back to early 1980s. The results of the performed trend analysis give first hints on the impacts of changes in SW radiation, total ozone and surface reflectivity on UV in the past. The many significant positive trends in UV radiation for January–June result from the combined effects of mostly non-significant temporal changes in SW, ozone, and

partly from snow cover, which are used for the reconstruction. However, further studies are necessary to assess the sensitivity of the found UV trends on the individual changes of the different environmental factors. This also allows the prediction of the UV response to future changes of SW radiation, ozone, and snow.

The derived relationship describes the link between cloud effects in total solar radiation and mainly the UVB, since the spectral maximum of erythemally weighted UV is around 305–310 nm. This also allows drawing conclusions for atmospheric chemistry. The important photodissociation of NO_2, for instance, has a large part of the absorption cross-section in the UVA range. The clear-sky modeling is well understood for UVA, which is situated between UVB and the visible part of the solar spectrum and thus the CMF_{UVA} should be intermediate between the one for UVB and SW range.

From an operational point of view, the derived method enables not only the development of UV now-casting tools and spatially more representative data sets but also the design of more sophisticated QA/QC procedures, which are able to detect instrument instabilities earlier and enhance the data quality in the future.

6.2 Outlook

In a future step, a more detailed spatial and temporal characterization of the aerosol optical depth could be introduced to evaluate the sensitivity of the derived method on aerosol variability. These results could also be used for the reconstruction and thus for refining the trends found in this study. Furthermore, the data quality issues discussed in the previous section underline some practical recommendations for the future operation of biometers. The complete calibration chain, as proposed by Webb et al. (2007) should be considered at all stations measuring erythemal UV radiation. This also requires the detection of the direct radiation beam in order to modify the necessary cosine correction correspondingly. Furthermore, the different quality levels of observed UV time-series need to be considered when using results of previous studies including observations without corrections for non-ideal cosine responses of the instruments.

For the development and comparison of different methods in this study, it was important to have access to UV radiation measurements at two stations in the Swiss lowlands and two in alpine and high-alpine regions. Therefore, the number and location of stations in Switzerland measuring erythemal UV radiation should be maintained. Furthermore, it needs to be considered to make the spectral UV measurements at Arosa available for future scientific studies in atmospheric radiation research.

The derived method proved to be capable of describing the short-term cloud effects on erythemal UV radiation at locations in Switzerland situated in regions with different climate conditions. Therefore, the presented parameterization can be developed further for providing a now-casting tool for erythemal UV radiation at more than 130 stations of the future SwissMetNet.

Appendix A

Snow line algorithm

This appendix describes how the algorithm treats the snow depth data and handles situations, where the usual regression technique fails.

- The snow line is calculated using the robust linear regression in case the slope is positive, which is in agreement with increasing snow depth with altitude (cf. Equation (3.1)). This is generally true in more than 90% of the analyzed situations, only in the NW-region, the portion of days with positive slopes is slightly smaller (86%). For the regression, snow observations of 0.00 m are removed except for the highest zero-value below the lowest non-zero observation.

- For cases with negative slopes, the lowest elevation with measured snow depth larger than 0.05 m is taken as snow line altitude. Negative slopes are rare and occur in less than 0.6% of the analyzed days in the northern part of Switzerland (NE, NW). The largest amount of negative slopes is found in the S-region (3.5%).

- If none of the stations is measuring more than 0.05 m of snow, climatological summer values for the snow line altitude are applied (NE: 2600 m, NW: 2800 m, SW: 3300 m, S: 3000 m, and SE: 3200 m MSL). These climatological snow line altitudes are estimations by a forecaster of the national weather service, MeteoSwiss, and are used in less than 5.3% of the analyzed situations. Only in the north-western part (NW) this fraction is higher (8.2%) where only four stations are located at higher altitudes than 1500 m MSL.

- In cases with less than three snow observations (> 0.00 m), a robust regression cannot be applied. In such cases, a simple linear interpolation is performed between the lowest altitude with snow and the highest station without observed snow. These situations occur in less than 3.3% of the analyzed days, except in the NW-region where in 5.2% of the cases such an interpolation is used.

Appendix B

Total solar radiation measurements in ANETZ and SwissMetNet

Total solar irradiance (SW) is measured concurrently by the operational and the high-resolution research network of MeteoSwiss at four stations in Switzerland. The operational network (ANETZ) measured SW radiation with 10-minute (10') time resolution over the last three decades and is currently modernized into a new network called "SwissMetNet" (SMN). This transition from ANETZ to SMN also includes a change in instrumentation, leading to inhomogeneities in the time-series, which are analyzed in this appendix. The SW measurements provided by the CHARM network are used as reference and are of higher quality and time resolution. In order to make CHARM and ANETZ/SMN data comparable, the high-resolution CHARM measurements are aggregated on a 10' time resolution.

Dominantly SW observations from the previous ANETZ network are used for deriving the relationships between cloud modification factors (CMF) in the UV and SW radiation (cf. Section 4.3.c). However, at the end of this "learning" period or during the validation phase (cf. Table 4.1), the transition to the new SwissMetNet took place at all four stations analyzed in this study. In order to make the SW data during the validation period comparable to the previous data, the differences between SW observations during ANETZ operation and after activation of SwissMetNet are assessed. For this analysis, the ratios between the operational data (ANETZ and SMN, respectively) and the high-resolution data of CHARM are investigated (Figure B.1).

The SW data provided by ANETZ are generally lower than the aggregated CHARM data at all four stations (left from the red line, Figure B.1). The agreement between the operational measurements and the data provided by the reference CHARM instruments clearly increased during the validation phase, which is due to the activation of SwissMetNet. Correction factors were derived for adjusting the SMN data to the previous ANETZ-levels (Table B.1). The reason for modifying the newer SMN data and not the older ANETZ data is the aim to apply the derived CMF relationships for UV reconstruction back to the early 1980s. These correction factors (F) are calculated from the comparison of the average ratios of ANETZ vs. CHARM and of SwissMetNet vs. CHARM during the analyzed periods:
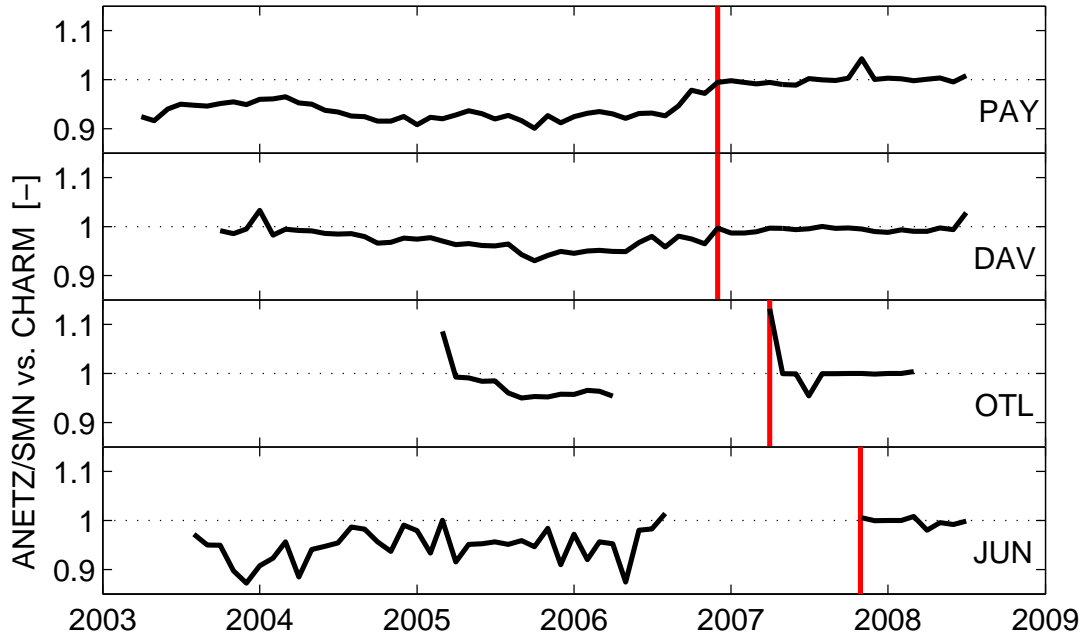
FIG. B.1: The monthly ratio between ANETZ and SMN data, respectively, and the CHARM measurements used as reference. The vertical red lines indicate the activation of the new SwissMetNet instrumentation at each of the four stations. Only the data within periods used for deriving the relationships and for validation (Table 4.1) are included.

$$F = \frac{\overline{\mathrm{SW_{ANETZ}/SW_{CHARM}}}}{\overline{\mathrm{SW_{SwissMetNet}/SW_{CHARM}}}}$$

The correction factors (F) are applied on SW observations for time periods after Swiss-MetNet activation.

TABLE B.1: Correction factors (F) to adjust SW observations by SwissMetNet instrumentation to previous ANETZ-levels. A: ANETZ, C: CHARM, S: SwissMetNet. The factors are calculated from average monthly ratios during the ANETZ and SwissMetNet operations within the periods analyzed in this study.

	A/C	S/C	F
Payerne	0.936	1.00	0.935
Davos	0.970	0.995	0.975
Jungfraujoch	0.948	0.998	0.950
Locarno-Monti	0.977	1.01	0.970

List of Figures

List of Tables

References

Al-Aruri, S. D., 1990: The empirical relationship between global radiation and global ultraviolet (0.290-0.385 μm) solar radiation components. *Sol. Energy*, **45 (2)**, 61–64, doi:10.1016/0038-092X(90)90028-B.

Ambach, W. and H. Eisner, 1986: Albedo verschiedener Schneeoberflaechen fuer erythemwirksame solare Strahlung (Albedo of various snow surfaces for erythemal solar radiation). *Wetter und Leben*, **38**, 1–4.

Anderson, G. P., S. A. Clough, F. X. Kneizys, J. H. Chetwynd, and E. P. Shettle, 1986: AFGL Atmospheric Constituent Profiles (0–120 km). *AFGL-TR-86-0110, AFGL (OPI), Hanscom AFB, MA 01736.*

Auer, M., R. Meister, A. Stoffel, and R. Weingartner, 2004: Analyse und Darstellung der mittleren monatlichen Schneehoehen in der Schweiz (Analysis and presentation of average monthly snowpack in Switzerland). *Wasser Energie Luft*, **96 (7/8)**, 173–178.

Balk, B. and K. Elder, 2000: Combining binary decision tree and geostatistical methods to estimate snow distribution in a mountain watershed. *Water Resour. Res.*, **36 (1)**, 13–26.

Barnston, A. and R. Livezey, 1987: Classification, Seasonality and Persistence of Low-Frequency Atmospheric Circulation Patterns. *Mon. Wea. Rev.*, **115**.

Bernhard, G., C. Booth, and J. Ehramjian, 2004: Version 2 data of the National Science Foundations Ultraviolet Radiation Monitoring Network: South Pole. *J. Geophys. Res.*, **109 (D21207)**, doi:10.1029/2004JD004937.

Blumthaler, M. and W. Ambach, 1988: Solar UVB-albedo of various surfaces. *Photochem. Photobiol.*, **48 (1)**, 85–88.

Blumthaler, M. and W. Ambach, 1990: Indication of increasing solar ultraviolet-B radiation flux in alpine regions. *Science*, **248 (4952)**, 206–208, doi:10.1126/science.2326634.

Blumthaler, M., W. Ambach, and M. Salzgeber, 1994: Effects of cloudiness on global and diffuse UV irradiance in a high-mountain area. *Theor. Appl. Climatol.*, **50 (1-2)**, 23–30, doi:10.1007/BF00864899.

Bodeker, G. E. and R. L. McKenzie, 1996: An Algorithm for Inferring Surface UV Irradiance Including Cloud Effects. *J. Appl. Meteorol.*, **35 (10)**, 1860–1877.

Bordewijk, J. A., H. Slaper, H. A. J. M. Reinen, and E. Schlamann, 1995: Total solar radiation and the influence of clouds and aerosols on the biologically effective UV. *Geophys. Res. Lett.*, **22 (16)**, 2151–2154.

Brönnimann, S., W. Eugster, and H. Wanner, 2001: Photo-oxidant chemistry in the polluted boundary layer under changing UV-B radiation. *Atmos. Environ.*, **35**, 3789–3797, doi:10.1016/S1352-2310(01)00162-5.

Calbó, J., D. Pagès, and J.-A. González, 2005: Empirical studies of cloud effects on UV radiation: A review. *Rev. Geophys.*, **43 (RG2002)**, doi:10.1029/2004RG000155.

Crutzen, P. J. and F. Arnold, 1986: Nitric acid cloud formation in the cold Antarctic stratosphere: a major cause for the springtime 'ozone hole'. *Nature*, **324**, 651–655, doi:10.1038/324651a0.

Dahlback, A. and K. Stamnes, 1991: A new spherical model for computing the radiation field available for photolysis and heating at twilight. *Planet. Space Sci.*, **39**, 671–683.

de Graaf, M., P. Stammes, and E. A. A. Aben, 2007: Analysis of reflectance spectra of UV-absorbing aerosol scenes measured by SCIAMACHY. *J. Geophys. Res.*, **112 (D02206)**, doi:10.1029/2006JD007249.

de Gruijl, F. R., J. Longstreth, M. Norval, A. P. Cullen, H. Slaper, M. L. Kripke, Y. Takizawa, and J. C. van der Leun, 2003: Health effects from stratospheric ozone depletion and interactions with climate change. *Photochem. Photobiol. Sci.*, **2**, 16–28, doi:10.1039/b211156j.

den Outer, P. N., H. Slaper, J. Matthijsen, H. A. J. M. Reinen, and R. Tax, 2000: Variability of ground-level ultraviolet: model and measurement. *Radiat. Prot. Dosimetry*, **91**, 105–110.

den Outer, P. N., H. Slaper, and R. B. Tax, 2005: UV radiation in the Netherlands: Assessing long-term variability and trends in relation to ozone and clouds. *J. Geophys. Res.*, **110 (D02203)**, doi:10.1029/2004JD004824.

Dietz, E. J. and T. J. Killeen, 1981: A nonparametric multivariate test for monotone trend with pharmaceutical applications. *J. Am. Stat. Assoc.*, **76**, 169–174.

Diffey, B., 2004: Climate change, ozone depletion and the impact on ultraviolet exposure of human skin. *Phys. Med. Biol.*, **49**, R1–R11, doi:10.1088/0031-9155/49/1/R01.

Duerr, B. and R. Philipona, 2004: Automatic cloud amount detection by surface longwave downward radiation measurements. *J. Geophys. Res.*, **109 (D05201)**, doi:10.1029/2003JD004182.

Eck, T. F., P. K. Bhartia, P. H. Hwang, and L. L. Stowe, 1987: Reflectivity of Earth's surface and clouds in ultraviolet from satellite observations. *J. Geophys. Res.*, **92 (D4)**, 4287–4296.

Erxleben, J., K. Elder, and R. Davis, 2002: Comparison of spatial interpolation methods for estimating snow distribution in the Colorado Rocky Mountains. *Hydrol. Process.*, **16**, 3627–3649, doi:10.1002/hyp.1239.

Farman, J. C., B. G. Gardiner, and J. D. Shanklin, 1985: Large losses of total ozone in Antarctica reveal seasonal ClO_x/NO_x interaction. *Nature*, **315**, 207–210, doi:10.1038/315207a0.

Feister, U. and K.-H. Grasnick, 1992: Solar UV radiation measurements at Potsdam (52°22'N, 13°5'E). *Sol. Energy*, **49 (6)**, 541–548, doi:10.1016/0038-092X(92)90162-4.

Fioletov, V. E., J. B. Kerr, C. T. McElroy, D. I. Wardle, V. Savastiouk, and T. S. Grajnar, 2005: The Brewer reference triad. *Geophys. Res. Lett.*, **32 (L20805)**, doi:10.1029/2005GL024244.

Foppa, N., A. Hauser, D. Oesch, S. Wunderle, and R. Meister, 2007a: Validation of operational AVHRR subpixel snow retrievals over the European Alps based on ASTER data. *Int. J. Remote Sens.*, **28 (21)**, 4841–4865, doi:10.1080/01431160701253287.

Foppa, N., A. Stoffel, and R. Meister, 2007b: Synergy of in situ and space borne observation for snow depth mapping in the Swiss Alps. *Int. J. Appl. Earth Obs.*, **9 (3)**, 294–310, doi:10.1016/j.jag.2006.10.001.

Foppa, N., S. Wunderle, A. Hauser, D. Oesch, and F. Kuchen, 2004: Operational subpixel snow mapping over the Alps with NOAA AVHRR data. *Ann. Glaciol.*, **38 (1)**, 245–252, doi:10.3189/172756404781814735.

Foukal, P., C. Fröhlich, H. Spruit, and T. M. L. Wigley, 2006: Variations in solar luminosity and their effect on the Earth's climate. *Nature*, **443**, 161–166, doi:10.1038/nature05072.

Foyo-Moreno, I., J. Vida, and L. Alados-Arboledas, 1999: A simple all weather model to estimate ultraviolet solar radiation (290-385 nm). *J. Appl. Meteorol.*, **38 (7)**, 1020–1026.

Frederick, J. E., A. E. Koob, A. D. Alberts, and E. C. Weatherhead, 1993: Empirical studies of tropospheric transmission in the ultraviolet: broadband measurements. *J. Appl. Meteorol.*, **32 (12)**, 1883–1892.

Gilbert, R. O., 1987: *Statistical methods for environmental pollution monitoring.* Van Nostrand Company, Hoboken, N. J., 320 pp.

Gröbner, J., G. Hülsen, L. Vuilleumier, M. Blumthaler, J. M. Vilaplana, D. Walker, and J. E. Gil, 2006: Report of the PMOD/WRC-COST calibration and intercomparison of erythemal radiometers Davos, Switzerland 28 July–23 August 2006. Tech. rep., PMOD/WRC Davos.

Häder, D.-P., 1997: *Solar ultraviolet radiation, modelling, measuring and effects, edited by C. S. Zerefos and A. F. Bais.* Springer-Verlag, 332 pp., Impact on marine ecosystems (p. 209–231).

Hamed, K. A. and A. R. Rao, 1998: A modified Mann-Kendall trend test for autocorrelated data. *J. Hydrol.*, **204**, 182–196.

Hantel, M., M. Ehrendorfer, and A. Haslinger, 2000: Climate sensitivity of snow cover duration in Austria. *Int. J. Climatol.*, **20 (6)**, 615–640.

Heimo, A., B. Calpini, T. Konzelmann, and S. Suter, 2006: SwissMetNet: The New Automatic Meteorological Network of Switzerland. *CIMO/TECO Conference, Geneva, 4-6 December 2006, extended abstract.*

Hirsch, R. M. and J. R. Slack, 1984: A nonparametric trend test for seasonal data with serial dependence. *Water Resour. Res.*, **20**, 727–732.

Hirsch, R. M., J. R. Slack, and R. A. Smith, 1982: Techniques of trend analysis for monthly water quality data. *Water Resour. Res.*, **18**, 107–121.

Jeannet, P., R. Stübi, G. Levrat, P. Viatte, and J. Staehelin, 2007: Ozone balloon soundings at Payerne (Switzerland): Reevaluation of the time series 1967-2002 and trend analysis. *J. Geophys. Res.*, **112 (D11302)**, doi:10.1029/2005JD006862.

Josefsson, W. and T. Landelius, 2000: Effect of clouds on UV irradiance: As estimated from cloud amount, cloud type, precipitation, global radiation and sunshine duration. *J. Geophys. Res.*, **105 (D4)**, 4927–4935.

Kato, S., T. Ackerman, J. Mather, and E. Clothiaux, 1999: The k-distribution method and correlated-k approximation for a shortwave radiative transfer model. *J. Quant. Spectrosc. Radiat. Transfer*, **62**, 109–121.

Kendall, M. G., 1938: A new measure of rank correlation. *Biometrika*, **30**, 81–93.

Kendall, M. G., 1955: *Rank Correlation Methods*. Charles Griffin, London.

Kendall, M. G., 1975: *Rank Correlation Methods*. Charles Griffin, London, 202 pp.

Kipp&Zonen, 2004: *CM 21 - Precision Pyranometer, Instruction Manual.* Kipp&Zonen, v.1004.

Koepke, P., et al., 1998: Comparison of models used for UV Index calculations. *Photochem. Photobiol.*, **67 (6)**, 657–662, doi:10.1111/j.1751-1097.1998.tb09470.x.

Koepke, P., et al., 2006: Modelling solar UV radiation in the past: comparison of algorithms and input data. *Proc. SPIE*, **636215**, doi:10.1117/12.687682.

Krüger, O. and H. Graßl, 2002: The indirect aerosol effect over Europe. *Geophys. Res. Lett.*, **29 (19)**, doi:10.1029/2001GL014081.

Krzyścin, J. W., 2008: Statistical reconstruction of daily total ozone over Europe 1950 to 2004. *J. Geophys. Res.*, **113 (D07112)**, doi:10.1029/2007JD008881.

Krzyścin, J. W., J. Jarosławski, and P. S. Sobolewski, 2003: Effects of clouds on the surface erythemal UV-B irradiance at northern midlatitudes: estimation from the observations taken at Belsk, Poland (1999–2001). *J. Atmos. Sol-Terr. Phys.*, **65**, 457–467.

Kylling, A., T. Persen, B. Mayer, and T. Svenœ, 2000: Determination of an effective spectral surface albedo from ground-based global and direct UV irradiance measurements. *J. Geophys. Res.*, **105 (D4)**, 4949–4959.

Lindfors, A. and A. Arola, 2008: On the wavelength-dependent attenuation of UV radiation by clouds. *Geophys. Res. Lett.*, **35 (L05806)**, doi:10.1029/2007GL032571.

Lindfors, A., A. Arola, J. Kaurola, P. Taalas, and T. S. e, 2003: Longterm erythemal UV doses at Sodankylä estimated using total ozone, sunshine duration, and snow depth. *J. Geophys. Res.*, **108 (D16)**, doi:10.1029/2002JD003325.

Lindfors, A., J. Kaurola, A. Arola, T. Koskela, K. Lakkala, W. Josefsson, J. Olseth, and B. Johnsen, 2007: A method for reconstruction of past UV radiation based on radiative transfer modeling: Applied to four stations in northern Europe. *J. Geophys. Res.*, **112 (D23201)**, doi:10.1029/2007JD008454.

Lindfors, A. and L. Vuilleumier, 2005: Erythemal UV at Davos (Switzerland) 1926–2003, estimated using total ozone, sunshine duration, and snow depth. *J. Geophys. Res.*, **110 (D02104)**, doi:10.1029/2004JD005231.

Liu, S., S. A. McKeen, and S. Madronich, 1991: Effect of anthropogenic aerosols on biologically active ultraviolet radiation. *Geophys. Res. Lett.*, **18 (12)**, 2265–2268.

López-Moreno, J. I. and D. Nogués-Bravo, 2005: A generalized additive model for the spatial distribution of snowpack in the Spanish Pyrenees. *Hydrol. Process.*, **19 (16)**, 3167–3176, doi:10.1002/hyp.5840.

López-Moreno, J. I. and D. Nogués-Bravo, 2006: Interpolating local snow depth data: an evaluation of methods. *Hydrol. Process.*, **20 (10)**, 2217–2232, doi:10.1002/hyp.6199.

Madronich, S., 1993: *UV-B radiation and ozone depletion: effects on humans, animals, plants, microorganisms, and materials, edited by Manfred Tevini.* Lewis Publishers, 248 pp., Chapter 2: UV Radiation in the Natural and Perturbed Atmosphere (p. 17–69).

Madronich, S., R. McKenzie, L. Bjorn, and M. Caldwell, 1998: Changes in biologically active ultraviolet radiation reaching the Earths surface. *J. Photoch. Photobio. B.*, **46**, 5–19.

Mann, H. B., 1945: Nonparametric tests against trend. *Econometrica*, **13 (3)**, 245–259.

Martinez-Lozano, J. A., A. J. Casanovas, and M. P. Utrillas, 1994: Comparison of global ultraviolet (290-385 nm) and global irradiation measured during the warm season in Valencia, Spain. *Int. J. Climatol.*, **14 (1)**, 93–102, doi:10.1002/joc.3370140108.

Marty, C., 2000: Surface radiation, cloud forcing and greenhouse effect in the Alps. Dissertation no. 13609, ETH Zurich.

Marty, C., 2008: Regime shift of snow days in Switzerland. *Geophys. Res. Lett.*, **35 (L12501)**, doi:10.1029/2008GL033998.

Marty, C., R. Philipona, C. Fröhlich, and A. Ohmura, 2002: Altitude dependence of surface radiation fluxes and cloud forcing in the alps: results from the alpine surface radiation budget network. *Theor. Appl. Climatol.*, **72 (3–4)**, 137–155, doi:10.1007/s007040200019.

Mayer, B. and A. Kylling, 2005: Technical note: The libRadtran software package for radiative transfer calculations – description and examples of use. *Atmos. Chem. Phys.*, **5**, 1855–1877.

Mayer, B., G. Seckmeyer, and A. Kylling, 1997: Systematic long-term comparison of spectral UV measurements and UVSPEC modeling results. *J. Geophys. Res.*, **102 (D7)**, 8755–8767.

McKinlay, A. and B. Diffey, 1987: A reference action spectrum for ultraviolet induced erythema in human skin, in human exposure to ultraviolet radiation: risks and regulations, edited by W. Passchier and B. Bosnajakovich. *Elsevier Sci., New York*, 83–87.

Moesch, M. and A. Zelenka, 2004: Globalstrahlungsmessung 1981–2000 im ANETZ. Tech. Rep. 207, Federal Office of Meteorology and Climatology MeteoSwiss.

Molina, M. J. and F. S. Rowland, 1974: Stratospheric sink for chlorofluoromethanes: chlorine atomcatalysed destruction of ozone. *Nature*, **249**, 810–812, doi:10.1038/249810a0.

Molotch, N. P., M. T. Colee, R. C. Bales, and J. Dozier, 2005: Estimating the spatial distribution of snow water equivalent in an alpine basin using binary regression tree models: the impact of digital elevation data and independent variable selection. *Hydrol. Process.*, **19 (7)**, 1459–1479, doi:10.1002/hyp.5586.

Newchurch, M. J., E.-S. Yang, D. M. Cunnold, G. C. Reinsel, J. M. Zawodny, and J. M. R. III, 2003: Evidence for slowdown in stratospheric ozone loss: First stage of ozone recovery. *J. Geophys. Res.*, **108 (D16)**, doi:10.1029/2003JD003471.

Norris, J. R. and M. Wild, 2007: Trends in aerosol radiative effects over Europe inferred from observed cloud cover, solar "dimming" and solar "brightening". *J. Geophys. Res.*, **112 (D08214)**, doi:10.1029/2006JD007794.

Perna, J. J., M. L. Mannix, J. F. Rooney, A. L. Notkins, and S. E. Straus, 1987: Reactivation of latent herpes simplex virus infection by ultraviolet light: a human model. *J. Am. Acad. Dermatol.*, **17 (3)**, 473–478.

Philipona, R., A. Heimo, C. Fröhlich, C. Marty, A. Ohmura, and C. Wehrli, 1996: The Swiss atmospheric radiation monitoring program: CHARM. A. DEEPAK Publishing, IRS '96: Current Problems in Atmospheric Radiation, ISBN 0-937194-39-5.

Power, H. C., 2003: Trends in solar radiation over Germany and an assessment of the role of aerosols and sunshine duration. *Theor. Appl. Climatol.*, **76**, 47–63, doi:10.1007/s00704-003-0005-8.

Rieder, H. E., F. Holawe, S. Simic, M. Blumthaler, J. W. Krzyścin, J. E. Wagner, A. W. Schmalwieser, and P. Weihs, 2008: Reconstruction of erythemal UV-doses for two stations in Austria: a comparison between alpine and urban regions. *Atmos. Chem. Phys.*, **8**, 6309–6323.

Ruckstuhl, C., et al., 2008: Aerosol and cloud effects on solar brightening and the recent rapid warming. *Geophys. Res. Lett.*, **35 (L12708)**, doi:10.1029/2008GL034228.

Scherrer, S. C. and C. Appenzeller, 2006: Swiss Alpine snow pack variability: major patterns and links to local climate and large-scale flow. *Clim Res*, **32**, 187–199.

Scherrer, S. C., C. Appenzeller, and M. Laternser, 2004: Trends in Swiss Alpine snow days: The role of local- and large-scale climate variability. *Geophys. Res. Lett.*, **31 (L13215)**, doi:10.1029/2004GL020255.

Schmucki, D., S. Voigt, R. Philipona, C. Froehlich, J. Lenoble, A. Ohmura, and C. Wehrli, 2001: Effective albedo derived from UV measurements in the Swiss Alps. *J. Geophys. Res.*, **106 (D6)**, 5369–5383.

Schwander, H., P. Koepke, A. Kaifel, and G. Seckmeyer, 2002: Modification of spectral UV irradiance by clouds. *J. Geophys. Res.*, **107 (D16)**, doi:10.1029/2001JD001297.

Sen, P. K., 1968: Estimates of the regression coefficient based on the Kendall's tau. *J. Am. Stat. Assoc.*, **63**, 1379–1389.

Shettle, E. P., 1989: Models of aerosols, clouds and precipitation for atmospheric propagation studies. *in AGARD Conference Proceedings No. 454, Atmospheric propagation in the uv, visible, ir and mm-region and related system aspects.*

Sneyers, R., 1992: On the use of statistical analysis for the objective determination of climate change. *Meteor. Z.*, **1**, 247–256.

Soehnge, H., A. Ouhtit, and H. N. Ananthaswamy, 1997: Mechanisms of induction of skin cancer by UV radiation. *Front. Biosci.*, **2**, 538–551.

Solomon, S., R. R. Garcia, F. S. Rowland, and D. J. Wuebbles, 1986: On the depletion of Antarctic ozone. *Nature*, **321**, 755–758, doi:10.1038/321755a0.

Staehelin, J., R. Kegel, and N. R. P. Harris, 1998a: Trend analysis of the homogenized total ozone series of Arosa (Switzerland), 1926-1996. *J. Geophys. Res.*, **103 (D7)**, 8389–8399, doi:10.1029/97JD03650.

Staehelin, J., et al., 1998b: Total ozone series at Arosa (Switzerland): Homogenization and data comparison. *J. Geophys. Res.*, **103 (D5)**, 5827–5841, doi:10.1029/97JD02402.

Steinbrecht, W., H. Claude, and P. Winkler, 2004: Enhanced upper stratospheric ozone: Sign of recovery or solar cycle effect? *J. Geophys. Res.*, **109 (D02308)**, doi:10.1029/2003JD004284.

Steinbrecht, W., et al., 2006: Long-term evolution of upper stratospheric ozone at selected stations of the Network for the Detection of Stratospheric Change (NDSC). *J. Geophys. Res.*, **111 (D10308)**, doi:10.1029/2005JD006454.

Stolarski, R. S., A. J. Krueger, M. R. Schoeberl, R. D. McPeters, P. A. Newman, and J. C. Alpert, 1986: Nimbus 7 satellite measurements of the springtime Antarctic ozone decrease. *Nature*, **322**, 808–811, doi:10.1038/322808a0.

Tevini, M., 1993: *UV-B Radiation and Ozone Depletion: effects on humans, animals, plants, microorganisms, and materials, edited by Manfred Tevini.* Lewis Publishers, 248 pp., Chapter 5: Effects of enhanced UV-B radiation on terrestrial plants (p. 125-153).

Theil, H., 1950: A rank-invariant method of linear and polynomial regression analysis. *Indagationes Math.*, **12**, 85–91.

Trepte, S. and P. Winkler, 2004: Reconstruction of erythemal UV irradiance and dose at Hohenpeissenberg (1968-2001) considering trends of total ozone, cloudiness and turbidity. *Theor. Appl. Climatol.*, **77**, 159–171, doi:10.1007/s00704-004-0034-y.

Valerie, K., A. Delers, C. Bruck, C. Thiriart, H. Rosenberg, C. Debouck, and M. Rosenberg, 1988: Activation of human immunodeficiency virus type 1 by DNA damage in human cells. *Nature*, **333**, 78–81, doi:10.1038/333078a0.

van der Leun, J. and F. R. de Gruijl, 1993: *UV-B radiation and ozone depletion: effects on humans, animals, plants, microorganisms, and materials, edited by Manfred Tevini.* Lewis Publishers, 248 pp., Chapter 4: Influences of ozone depletion on human and animal health (p. 95–123).

van der Leun, J. C., X. Tang, and M. Tevini, (Eds.) , 1998: *Environmental Effects of Ozone Depletion: 1998 Assessment.* Secretariat for the Vienna Convention for the Protection of the Ozone Layer and the Montreal Protocol on Substances that Deplete the Ozone Layer, United Nations Environment Programme, UNEP, Nairobi, Kenya, ISBN 92-807-1724-3.

Vestreng, V., G. Myhre, H. Fagerli, S. Reis, and L. Tarrasón, 2007: Twenty-five years of continuous sulphur dioxide emission reduction in Europe. *Atmos. Chem. Phys.*, **7**, 3663–3681.

Walker, D. M., L. Vuilleumier, C. Marty, S. Brönnimann, and U. Lohmann, 2009: Regional snow distribution and evolution in Switzerland between 1980 and 2008, (submitted). *J. Appl. Meteorol. Clim.*

Webb, A., J. Gröbner, and M. Blumthaler, 2007: A practical guide to operating broadband instruments measuring erythemally-weighted irradiance. EUR 22595, ISBN 92-898-0032-1.

Weihs, P., et al., 2001: Modeling the effect of an inhomogeneous surface albedo on incident UV radiation in mountainous terrain: determination of an effective surface albedo. *Geophys. Res. Lett.*, **28 (16)**, 3111–3114.

Wild, M., J. Grieser, and C. Schär, 2008: Combined surface solar brightening and increasing greenhouse effect support recent intensification of the global land-based hydrological cycle. *Geophys. Res. Lett.*, **35**, doi:10.1029/2008GL034842.

Wilks, D. S., 1995: *Statistical Methods in the Atmospheric Sciences - An Introduction*, Vol. 59. Academic Press, Inc., 467 pp.

Willmott, C. J., 1982: Some comments on the evaluation of model performance. *Bull. Am. Meteorol. Soc.*, **63 (11)**, 1309–1313.

Wiscombe, W., R. Welch, and W. Hall, 1984: The Effects of Very Large Drops on Cloud Absorption. Part I: Parcel Models. *J. Atmos. Sci.*, **41**, 1336–1355.

Yang, E.-S., D. M. Cunnold, M. J. Newchurch, R. J. Salawitch, M. P. McCormick, J. M. R. III, J. M. Zawodny, and S. J. Oltmans, 2008: First stage of Antarctic ozone recovery. *J. Geophys. Res.*, **113 (D20308)**, doi:10.1029/2007JD009675.

Acronyms and abbreviations

ANETZ   MeteoSwiss automatic network consisting of 72 stations with high data availability for standard meteorological applications. Currently transforming into SwissMetNet (SMN, see below).

APCADA   Automatic partial cloud amount detection algorithm - based on observed longwave downward radiation, temperature, and relative humidity at screen level height (Duerr and Philipona, 2004).

ASRB   Alpine Surface Radiation Budget network. This project aims at investigating the surface radiation budget at different altitudes and its relation to the greenhouse effect and to temperature and humidity in a changing climate (Source: MeteoSwiss).

B   Bias

biometer Synonym for UV broadband radiometer (cf. SL 501)

Black body For a given temperature, wavelength and surface exists an upper limit for the energy a body can emit. A black body emits the maximal possible intensity at all wavelengths.

BSRN   BSRN is a project of the Radiation Panel from the Global Energy and Water Cycle Experiment GEWEX under the umbrella of the World Climate Research Programme (WCRP) and as such is aimed at detecting important changes in the Earth's radiation field at the Earth's surface which may be related to climate changes. (Source: World Radiation Monitoring Center)

CHARM   Swiss Atmospheric Radiation Monitoring Program consists of four stations in the Swiss lowlands and the Alps: Payerne, Davos, Jungfraujoch and Locarno-Monti. This research network measures operationally erythemal UV radiation with broadband radiometers (biometers).

CIE   The International Commission on Illumination - also known as the CIE from its French title, the Commission Internationale de l'Eclairage - is devoted to worldwide cooperation and the exchange of information on all matters relating to the science and art of light and lighting, colour and vision, and image technology. (http://www.cie.co.at)

CM21	High quality pyranometer for measuring the irradiance on a plane surface. This instrument is compliant with the ISO 9060 secondary standard instrument performance criteria and is used in the solar radiation monitoring network BSRN (Baseline Surface Radiation Network) of WMO. This instrument is used in MeteoSwiss' operational network for measuring the total shortwave irradiance (SW) and is the follow-up model of the previous CM5.
CMF	Cloud Modification Factor built by the ratio of the radiation for all-sky conditions to the radiation for the same situations but without clouds (clear-sky estimates).
CMF_{SW}	CMF in the SW range
CMF_{UV}	CMF in the UV range
COST	"European Cooperation in the Field of Scientific and Technical Research" is one of the longest-running European instruments supporting cooperation among scientists and researchers across Europe. (www.cost.esf.org)
COST 713	COST initiative to establish tested and standardized UV-B radiation forecasts for public information in Europe.
COST 726	"Long term changes and climatology of UV radiation over Europe" – for advancing the understanding of UV radiation distribution under various meteorological conditions in Europe in order to determine UV radiation climatology and assess UV changes over Europe. (www.cost726.org)
CUVRA	Characteristics of the UV radiation field in the Alps.
DAV	Davos
dec^{-1}	per decade
DEM	Digital Elevation Model
DJF	winter season: December–February
EAWR-Index	The East Atlantic/West Russia (EATL/WRUS) pattern is one of three prominent teleconnection patterns that affects Eurasia throughout year. This pattern has been referred to as the Eurasia-2 pattern by Barnston and Livezey (1987). (Source: NOAA)
ETH	Swiss Federal Institute of Technology
EDUCE	European Database for UV Climatology and Evolution - a research project for investigating the UV radiation climate in Europe.
FAR	False Alarm Rate

GAW	The Global Atmosphere Watch program is one of WMO's most important contributions to the study of environmental issues in the post-UNCED period (United Nations Conference on Environment and Development, 1992). The mission of GAW is making reliable, comprehensive observations of the chemical composition and selected physical characteristics of the atmosphere on global and regional scales. Furthermore, the program provides the scientific community with the means to predict future atmospheric states. (Source: World Meteorological Organization)
Global radiation	Total radiation on a horizontal surface resulting from the direct solar radiation and from the diffuse radiation incident from the hemisphere above.
HR	Hit Rate
K	Kelvin
Irradiance	see "Global radiation"
JUN	Jungfraujoch
libRadtran	library for radiative transfer calculations (www.libradtran.org).
MAM	spring season: March–May
MeteoSwiss	Swiss Federal Office of Meteorology and Climatology
MSL	above Mean Sea Level
μm	micrometer
NE	North-eastern part of Switzerland (lowland region)
Near-IR	Infrared radiation with wavelengths between 780–2500 nm
nm	nanometer
NW	North-western part of Switzerland (lowland region)
OTL	Locarno-Monti
PAG	Post-agreement
PAY	Payerne
PFR	The Precision Filter Radiometer (PFR) is a research grade instrument to measure direct solar irradiance in 4 narrow spectral bands centered at wavelengths recommended by World Meteorological Organization for the determination of atmospheric aerosol optical depth. (Source: PMOD/WRC)
PMOD/WRC	Physikalisch-Meteorologisches Observatorium Davos / World Radiation Center (www.pmodwrc.ch)
POD	Probability of detection

p (-value)	The *p value* is the specific probability that the observed value of the test statistic, together with all others at least as unfavorable to the null hypothesis, will occur according to the null distribution. Thus the null hypothesis is rejected if the *p value* is less than or equal to the test level, and is not rejected otherwise (Wilks, 1995).
QA/QC	Quality Assurance and Quality Control
RACE-UV	Representative Alpine Climatology for Erythemal UV. This project is a contribution to the COST action 726. The particular aim of this project is testing the methodology for building a UV climatology in Switzerland. This includes investigating the dependency of the established UV estimation relationships on the location environment and conditions met in Switzerland.
RMS	Root-Mean-Square
RTM	Radiative Transfer Model
S	Southern part of Switzerland (alpine region, mainly canton Ticino)
SACRaM	Swiss Alpine Climate Radiation Monitoring network - a new atmospheric radiation research network of MeteoSwiss emerging from the previous CHARM and stations from the ASRB-network.
SE	South-eastern part of Switzerland (alpine region, mainly canton Graubünden)
SL	Snow line altitude
SL 501	SolarLight UVB Biometer Model 501 radiometer. This instrument measures the UV radiation with a filter close to the erythemal action spectrum and is based on the Robertson Berger technology.
SLF	WSL Institute for Snow and Avalanche Research
SMN	The new automatic meteorological network of MeteoSwiss (SwissMetNet)
SW	Total solar radiation (ShortWave radiation, ca. $< 3\mu m$)
SW	South-western region of Switzerland (alpine region, mainly canton Valais)
SZA	Solar Zenith Angle (90° - solar elevation)
TOA	Top Of Atmosphere
TSI	Total Solar Irradiance
UTC	coordinated universal time
UV	Ultraviolet radiation (100-400 nm)
UVA	UV-A radiation (315–400 nm)

UVB   UV-B radiation (280–315 nm), note: often UVB is extended to 320 nm in scientific literature.

UVC   UV-C radiation (200–280 nm)

UVI   UV-Index

Vacuum UV   Ultraviolet radiation (< 200 nm)

Vitamin D_3 Vitamin necessary for the formation and maintenance of our bone system and for several other health effects. The vitamin may also be supplied via the diet, but the formation in the skin by solar UV-B radiation usually forms an important part of the supply (van der Leun and de Gruijl, 1993).

WMO   World Meteorological Organization

WSL   Swiss Federal Institute for Forest, Snow and Landscape Research (an institute of the ETH domain)

yr^{-1} per year

α The test level (α) determines the "sufficiently improbable" region of the null distribution, also called "rejection level" (Wilks, 1995).

10'   10 minutes

Acknowledgements

guter letzt der wichtigste Dank an meine Eltern und Familie, welche den Weg zu dieser Dissertation erst möglich gemacht haben. Ich danke euch für eure enorme Unterstützung, auf die ich immer zählen durfte und euren Zuspruch in den schwierigeren Phasen.

Curriculum Vitae

Daniel Walker, rue de la Boverie 16, CH-1530 Payerne
born on 10 August 1976 in Zurich; citizen of Winterthur (ZH) and Gurtnellen (UR)

PROFESSIONAL TRAINING

08/2005 – 05/2009	Doctorate at ETH Zurich and MeteoSwiss Payerne
04/2005 – 07/2005	Project collaborator at Swiss Re Zurich
07/2004 – 11/2005	Research assistant at the Institute for Atmospheric and Climate Science (IACETH), ETH Zurich
04/2002 – 12/2004	Geological consulting, A. Rissi, Dipl. Natw. ETH, Zurich (part time)
08/1992 – 08/1996	Apprenticeship as a draftsman in an architectural office, Tauscher & Waibel, Arch. HTL, Winterthur

EDUCATION

08/2005 – 05/2009	PhD student at the Institute for Atmospheric and Climate Science (IACETH), ETH Zurich
09/2005 – 10/2007	Advanced studies in applied statistics at the Seminar for Statistics, Dep. of Mathematics, ETH Zurich
09/2000 – 05/2005	Master's degree in Earth Sciences, ETH Zurich
08/1998 – 06/2000	High school, type C, "Kantonale Maturitätsschule für Erwachsene (KME)", Zurich
08/1997 – 07/1998	Technical high school, Winterthur
08/1992 – 07/1996	Apprenticeship draftsman: Vocational school with technical school, GIB, Winterthur
04/1983 – 07/1992	Public schools

CONFERENCE CONTRIBUTIONS

- European Geoscience Union (EGU) General Assembly, Vienna, Austria, April, 2006

- European Geoscience Union (EGU) General Assembly, Vienna, Austria, April, 2007

- 5th Swiss Geoscience Meeting, Geneva, November, 2007

- Quadrennial Ozone Symposium (QOS), Tromsø Norway, July, 2008

- 6th Swiss Geoscience Meeting, Lugano, November, 2008

- IAMAS-IAPSO-IACS Joint Assembly *MOCA-09*, Montreal, Canada, July 19–29, 2009

PUBLICATIONS

- Walker, D. M., L. Vuilleumier, C. Marty, S. Brönnimann, and U. Lohmann, 2009: Regional snow distribution and evolution in Switzerland between 1980 and 2008, (submitted). *J. Appl. Meteorol. Clim.*

- Walker, D. M., L. Vuilleumier, S. Brönnimann, and U. Lohmann, 2009: Cloud effects on erythemal ultraviolet (UV) and total solar radiation in Switzerland, *in preparation*

- Gröbner, J., G. Hülsen, L. Vuilleumier, M. Blumthaler, J. M. Vilaplana, D. Walker, and J. E. Gil, 2006: Report of the PMOD/WRC-COST calibration and intercomparison of erythemal radiometers Davos, Switzerland 28 July–23 August 2006. Tech. rep., PMOD/WRC Davos.

- Vuilleumier, L., and D. Walker, 2008: Swiss National Report for the 7th WMO/UNEP Ozone Research Managers Meeting, Geneva, 18–21 May 2008, Chapter 2.

- Vuilleumier, L., D. Walker, and J. Verdebout, 2009: Long term changes and climatology of UV radiation over Europe, *Final Scientific Report for COST Action 726*, Section 3.3 Albedo.

- Vuilleumier, L., R. Philipona and D. Walker, 2009: Global Atmosphere Watch Radiation Measurements, *International Foundation HFSJG - Activity Report 2008.*

Veröffentlichungen der MeteoSchweiz

85   Ambühl, J: 2010, Neural interpretation of ECMWF ensemble predictions, 48pp, CHF 68.-

84   Ambühl, J: 2010, Customer oriented warning systems, 91pp, CHF 78.-

83   Ceppi, P: 2010, Spatial characteristics of gridded Swiss temperature trends: local and large-scale influences, 82pp, CHF 76.-

82   Blanc, P: 2009, Ensemble-based uncertainty prediction for deterministic 2 m temperature forecasts, 90pp, CHF 78.-

81   Erdin R: 2009, Combining rain gauge and radar measurements of a heavy precipitation event over Switzerland: Comparison of geostatistical methods and investigation of important influencing factors, 109pp, CHF 81.-

80   Buzzi M: 2008, Challenges in Operational Numerical Weather Prediction at High Resolution in Complex Terrain, 186pp, CHF 103.-

79   Nowak D: 2008, Radiation and clouds: observations and model calculations for Payerne BSRN site, 101pp, CHF 80.-

78   Arpagaus M, Rotach M, Ambrosetti P, Ament F, Appenzeller C, Bauer H-S, Bouttier F, Buzzi A, Corazza M, Davolio S, Denhard M, Dorninger M, Fontannaz L, Frick J, Fundel F, Germann U, Gorgas T, Grossi G, Hegg C, Hering A, Jaun S, Keil C, Liniger M, Marsigli C, McTaggart-Cowan R, Montani A, Mylne K, Ranzi R, Richard E, Rossa A, Santos-Muñoz D, Schär C, Seity Y, Staudinger M, Stoll M, Vogt S, Volkert H, Walser A, Wang Y, Werhahn J, Wulfmeyer V, Wunram C and Zappa M: 2009, MAP D-PHASE: Demonstrating forecast capabilities for flood events in the Alpine region. Report of the WWRP Forecast Demonstration Project D-PHASE submitted to the WWRP Scientific Steering Committee, 65pp, CHF 73.-

77   Rossa AM: 2007, MAP-NWS – an Optional EUMETNET Programme in Support of an Optimal Research Programme, 67pp, CHF 73.-

76   Baggenstos D: 2007, Probabilistic verification of operational monthly temperature forecasts, 52pp, CHF 69.-

75   Fikke S, Ronsten G, Heimo A, Kunz S, Ostrozlik M, Persson PE, Sabata J, Wareing B, Wichura B, Chum J, Laakso T, Säntti K and Makkonen L: 2007, COST 727: Atmospheric Icing on Structures Measurements and data collection on icing: State of the Art, 110pp, CHF 83.-

74   Schmutz C, Müller P und Barodte B: 2006, Potenzialabklärung für Public Private Partnership (PPP) bei MeteoSchweiz und armasuisse Immobilien, 82pp, CHF 76.-

73   Scherrer SC: 2006, Interannual climate variability in the European and Alpine region, 132pp, CHF 86.-

72   Mathis H: 2005, Impact of Realistic Greenhouse Gas Forcing on Seasonal Forecast Performance, 80pp, CHF 75.-

71   Leuenberger D: 2005, High-Resolution Radar Rainfall Assimilation: Exploratory Studies with Latent Heat Nudging, 103pp, CHF 81.-

70   Müller G und Viatte P: 2005, The Swiss Contribution to the Global Atmosphere Watch Programme – Achievements of the First Decade and Future Prospects, 112pp, CHF 83.-

69   Müller WA: 2004, Analysis and Prediction of the European Winter Climate, 115pp, CHF 34.

68   Bader S: 2004, Das Schweizer Klima im Trend: Temperatur- und Niederschlagsentwicklung seit 1864, 48pp, CHF 18.-

67   Begert M, Seiz G, Schlegel T, Musa M, Baudraz G und Moesch M: 2003, Homogenisierung von Klimamessreihen der Schweiz und Bestimmung der Normwerte 1961-1990, Schlussbericht des Projektes NORM90, 170pp, CHF 40.-

Frühere Veröffentlichungen und Arbeitsberichte finden sich unter
www.meteoschweiz.ch » Forschung » Publikationen

Arbeitsberichte der MeteoSchweiz

229 Philipona R, Levrat G, Romanens G, Jeannet P, Ruffieux D and Calpini B, 2009: Transition from VIZ / Sippicanto ROTRONIC - A new humidity sensor for the SWISS SRS 400 Radiosonde, 37pp, CHF 66.-

228 MeteoSchweiz: 2009, Klimabericht Kanton Graubünden, 40pp, nur als .pdf erhältlich

227 MeteoSchweiz, 2009, Basisanalysen ausgewählter klimatologischer Parameter am Standort KKWLeibstadt, 135pp, CHF 88.-

226 MeteoSchweiz, 2009, Basisanalysen ausgewählter klimatologischer Parameter am Standort KKW Mühleberg, 136pp, CHF 88.-

225 MeteoSchweiz, 2009, Basisanalysen ausgewählter klimatologischer Parameter am Standort KKW Gösgen, 136 pp, CHF 88.-

224 MeteoSchweiz, 2009, Basisanalysen ausgewählter klimatologischer Parameter am Standort KKW Beznau, 135pp, CHF 88.-

223 Dürr B: 2008, Automatisiertes Verfahren zur Bestimmung von Föhn in den Alpentälern, 22pp, CHF 62.-

222 Schmutz C, Arpagaus M, Clementi L, Frei C, Fukutome S, Germann U, Liniger M und Schacher F: 2008, Meteorologische Ereignisanalyse des Hochwassers 8. bis 9. August 2007, 29pp, CHF 64.-

221 Frei C, Germann U, Fukutome S und Liniger M: 2008, Möglichkeiten und Grenzen der Niederschlagsanalysen zum Hochwasser 2005, 19pp, CHF 62.-

220 Ambühl J: 2008, Optimization of Warning Systems based on Economic Criteria, 79pp, CHF 75.-

219 Ceppi P, Della-Marta PM and Appenzeller C: 2008, Extreme Value Analysis of Wind Observations over Switzerland, 43pp, CHF 67.-

218 MeteoSchweiz (Hrsg): 2008, Klimaszenarien für die Schweiz – Ein Statusbericht, 50pp, CHF 69.-

217 Begert M: 2008, Die Repräsentativität der Stationen im Swiss National Basic Climatological Network (Swiss NBCN), 40pp, CHF 66.-

216 Della-Marta PM, Mathis H, Frei C, Liniger MA and Appenzeller C: 2007, Extreme wind storms over Europe: Statistical Analyses of ERA-40, 80pp, CHF 75.-

215 Begert M, Seiz G, Foppa N, Schlegel T, Appenzeller C und Müller G: 2007, Die Überführung der klimatologischen Referenzstationen der Schweiz in das Swiss National Climatological Network (Swiss NBCN), 47pp, CHF 68.-

214 Schmucki D und Weigel A: 2006, Saisonale Vorhersage in Tradition und Moderne: Vergleich der "Sommerprognose" des Zürcher Bööggs mit einem dynamischen Klimamodell, 46pp, CHF 68.-

213 Frei C: 2006, Eine Länder übergreifende Niederschlagsanalyse zum August Hochwasser 2005. Ergänzung zu Arbeitsbericht 211, 10pp, CHF 59.-

212 Z'graggen, L: 2006, Die Maximaltemperaturen im Hitzesommer 2003 und Vergleich zu früheren Extremtemperaturen, 74pp, CHF 75.-

211 MeteoSchweiz: 2006, Starkniederschlagsereignis August 2005, 63pp, CHF 72.-

210 Buss S, Jäger E and Schmutz C: 2005: Evaluation of turbulence forecasts with the aLMo, 58pp, CHF 70.–

209 Schmutz C, Schmuki D, Duding O, Rohling S: 2004, Aeronautical Climatological Information Sion LSGS, 77pp, CHF 25.–

Frühere Veröffentlichungen und Arbeitsberichte finden sich unter
www.meteoschweiz.ch » Forschung » Publikationen